Localization In Photonic Crystals

Faris Siedahmed Mohammed Osman

A thesis submitted to the Faculty of Science, University of the Witwatersrand,

in fulfilment of the requirements for the degree of doctor of philosophy (Physics)

School of Physics

University of the Witwatersrand,

Johannesburg.

24 March 2017

Abstract

This thesis is an accumulation of the work and that was carried out and published as two articles and two book chapters. Throughout the thesis, we develop and present theoretical as well as numerical model to extend the existing techniques to study the optical properties of photonic crystals, plasmonic photonic crystals and photonic quasicrystals.

We start with a background review, where we cover the theoretical aspects of light–matter interaction. That is followed by a review of the physics of photonic crystals. In that chapter, we discuss the different properties of photonic crystals, plasmonic photonic crystals as well as the topic of localization. We then delve into the numerical aspects of the subject. We provide a review on the frequency domain method and the finite–differences–time–domain methods which they are both used in the work to perform different types of simulations.

The frequency domain method is, then, extended to enable the numerical analysis of the optical properties in plasmonic photonic crystals. We use first order perturbation theory to study the effect of surface plasmon polaritons on the photonic band structure of plasmonic photonic crystals. We developed a simple numerical tool that extends the standard frequency domain methods to compute the photonic band structure of plasmonic photonic crystals.

We then employ the two stage cut and project scheme to generate a dodecagonal two–dimensional quasiperiodic structure. The finite-differences-time–domain method is applied to simulate the propagation of electromagnetic modes in the system. We compute the transmission coefficients as well as the inverse participation ratio for a quasicrystal consisting of dielectric cylindrical rods. The analysis has shown that crystal has critical states. Furthermore, we apply the frequency domain method to quantify the localized modes in the vicinity of defects in a two–dimensional photonic crystal. We compute the intensity of those modes in the surroundings of the defects sites to identify their nature. Finally, we use the finite–differences–time–domain method to provide a second example of a quasicrystalline structure, where the states are localized.

Declaration

I, the undersigned, declare that this dissertation is my own, unaided work. It is being submitted for the Degree of Doctorate of Philosophy in Science at the University of the Witwatersrand, Johannesburg. It has not been submitted before for any degree or examination at any other University.

The work was done under the guidance of Professor Alex Quandt, at the University of the Witwatersrand, Johannesburg, South Africa.

Faris Siedahmed Mohammed, 23 March 2017

In my capacity as supervisor of the candidate's thesis, I certify that the above statements are true to the best of my knowledge.

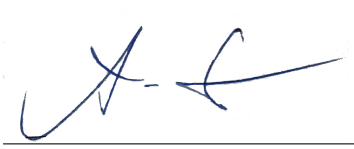

Alex Quandt, 23 March 2017

Contents

1. Introduction

The control over the properties of materials has always been a topic of interest to mankind, which often culminated in tools and devices of great benefits. The transistor, for instance, emerged from the ability to control the electrons in specific systems at the microscopic scale. The development of such devices resulted in highly sophisticated technologies that became an essential part of our lives.

On the other hand, the control over the optical properties has not been as successful as its electronic counterpart for various reasons. Following the first breakthrough in the field of photonic crystals in 1987 by Eli Yablonovitch [1], the fabrication of new structures that exhibit desired properties such as photonic band gaps was not a trivial task, hence the numerical simulations came in as a major player in the development of the field of photonic crystals.

The numerical methods in general played a critical role in advancing the natural as well as the applied sciences. In particular methods such as the finite–differences–time–domain and frequency–domain helped in understanding the optical characteristics of systems such as photonic crystals and optical waveguides. Moreover, the giant leap in computer hardware made it possible to efficiently run massive simulations in shorter periods of time with high accuracy. The work carried out in this thesis focuses on the development of different numerical methods as well as extending existing techniques to study the optical properties of photonic crystals. Some of the developments are included in appendix A.

Through the different chapters of the thesis, we provide a cumulative summary of different numerical schemes that have been developed and tested to study the different properties of photonic crystals. The work carried out in this thesis has been published in different journals [2, 3, 4, 5], see appendices B, C, D and E.

In chapter 2 we review some of the core concepts used throughout this work such as light–matter interactions and the frequency dielectric function. We further provide a simple derivation of Drude–Lorentz model using the Ehrenfest theorem. As part of this chapter, we shed light on plasmons and their different types which are linked to the study carried out in a future chapter.

In chapter 3 we review the physics of photonic crystals in addition to plasmonic photonic crystals,

and photonic quasicrystals. The chapter serves as an introduction to the three main topics studied in the thesis; photonic crystals, plasmonic photonic crystals and optical localization in photonic systems. That is followed by a chapter dedicated to the discussion of the numerical methods used in the simulations.

In chapter 5 we shift the attention to the topic of plasmonic photonic crystals where we develop a simple perturbation theory to calculate the impact of surface plasmon polaritons on the photonic band structure.

The topic of optical localization is addressed in chapter 6, where we develop a scheme to compute the optical properties of photonic quasicrystals. Finally, in chapter 7 we present different schemes to identify localized states in optical systems. We provide two different examples where we study the states formed in the vicinity of defects in a regular photonic crystal, as well as the optical modes in a photonic quasicrystal.

2. Light–Matter Interactions

The electronic properties of any material depend on the nature of the chemical bonds at its atomic level. Electrons that are strongly bound to the ions lead to insulating or semiconducting systems. Electrons that move freely throughout the structure result in metallic systems. Regardless of the nature of the system, photons may interact with these electrons leading to a new set of phenomena. This chapter will serve as an introduction to the resulting light–matter interactions.

In the following sections we will cover the theoretical background to understand the interaction between light and matter within the framework of Drude–Lorentz model [6]. In the first part of this chapter we will discuss the Ehrenfest theorem due to its importance and the fundamental role it plays in developing the Drude–Lorentz model. The second part will shed some light on the different types within interaction between light and electron gas called plasmons. The content of this chapter was published in [4, 5].

2.1 Frequency Dependent Dielectric Functions

The predictions made by the Drude–Lorentz model are formally based on a classical oscillator model. In order to justify such an approach, the basic equations of motion that characterize the microscopic properties may be understood in the theoretical framework of the Ehrenfest theorem [7].

2.1.1 Ehrenfest Theorem

Consider a nucleus uniformly charged with an elementary positive charge e located at the centre of a sphere with radius R. In a classical picture the charge density ϱ, which is localized, is simply the result of the division of the total charge by the volume of the sphere

$$\varrho = -\frac{3e}{4\pi R^3} \,. \tag{2.1}$$

Now assume there is a charged test particle that moves within that charged sphere. Such motion can be induced by an external electromagnetic field. The problem in hand also represents the

motion of an electronic cloud around a fixed charge. According to Gauss law, the force exerted on the charged particle is radially symmetric:

$$F(r) = \frac{e^2}{4\pi\varepsilon_\circ}\frac{r}{R^3} \equiv -kr \ , \tag{2.2}$$

where $\varepsilon_\circ$ is the vacuum permittivity. This force is a harmonic restoring force with spring constant

$$k = \frac{e^2}{4\pi\varepsilon_\circ}\frac{1}{R^3} \tag{2.3}$$

and angular frequency

$$\omega_\circ^2 = \frac{k}{m_e} \ , \tag{2.4}$$

where m_e is the mass of an electron. According to the Ehrenfest theorem, $\vec{r}$ is the quantum mechanical expected value of the position operator $\langle\vec{r}|$, such that $\vec{r} \equiv \langle\vec{r}\rangle$ and $\langle F(\vec{r})\rangle \equiv F(\vec{r})$. This leads to the classical equation of motion as described in the following.

Applying an oscillating electric field $\vec{E}(t) = \vec{E}_\circ \exp(i\omega t)$ will lead to the following equation of motion:

$$m_e\frac{d^2r}{dt^2} + m_e\gamma\frac{dr}{dt} + m_e\omega_\circ^2 r = -eE(t) \tag{2.5}$$

where γ is a damping rate which describes energy loss. It can be thought of as the damping originating from the classical radiation of a moving electric charge. However, a better picture is that of a solid material with the oscillators coupled to a heat bath that drains out the energy.

Moreover, the damped oscillation of the electronic cloud around the nucleus forms a local dipole moment. The value of the local electric field interacting with the local dipole is usually treated as the contribution of the applied electric fields added to that of the dipole–dipole interactions.

To find the solution of Eq. 2.5, the ansatz $\vec{r}(t) = \vec{r_\circ}\exp(i\omega t)$ can be used to compute the amplitude $\vec{r_\circ}$ as well as the macroscopic polarization $\vec{P}$, which represents the dipole moment per unit volume. Assume that N is the number of atoms per unit volume in the system, then

$$\vec{P} = -Ne\vec{r} = \frac{Ne^2}{m_e}\frac{1}{(\omega_\circ^2 - \omega^2 - i\gamma\omega)}\vec{E} \tag{2.6}$$

2.1.2 Drude–Lorentz Model

The model described above deals with the interaction between electrons in a bulk material and an externally applied electromagnetic field. From basic electrodynamics one can calculate the

dielectric displacement $\vec{D}$:

$$\vec{D} = \varepsilon_\circ \vec{E} + \vec{P} \equiv \varepsilon_\circ \varepsilon_r(\omega)\vec{E} \equiv \varepsilon_\circ(1 + \chi(\omega))\vec{E}\ , \tag{2.7}$$

where $\chi(\omega)$ is the electric susceptibility of the system. Using the expression obtained in Eq. 2.7, the complex relative dielectric function of the Drude–Lorentz model is

$$\varepsilon_r(\omega) = 1 + \frac{Ne^2}{m_e\varepsilon_\circ}\frac{1}{(\omega_\circ^2 - \omega^2 - i\gamma\omega)} \tag{2.8}$$

Note that the core assumption used to derive this formula states that the electrons are tightly bound to the nucleus, which is valid for insulators and semiconductors. For metals, however, the electrons are required to be free which requires the radius of the charged sphere to be very large, and consequently the spring constant in Eq. 2.3 and the value of the plasma frequency in Eq. 2.4 approaches zero. Thus, for a metallic system the dielectric function reads:

$$\varepsilon_r(\omega) = 1 - \frac{Ne^2}{m_e\varepsilon_\circ}\frac{1}{(\omega^2 + i\gamma\omega)} = 1 - \frac{\omega_p^2}{(\omega^2 + i\gamma\omega)}\ , \tag{2.9}$$

where $\omega_p = \sqrt{\frac{Ne^2}{m_e\varepsilon_\circ}}$ is the plasma frequency.

The model described by Eqs. 2.8 and 2.9 can be further refined and even parametrized using quantum mechanical data [8], which makes it useful to model the optical properties of insulators and metals at least over certain frequency ranges. Nowadays *ab initio* methods can be used to evaluate $\varepsilon_r(\omega)$ on the entire frequency range from $\omega = 0$ to $\omega = \infty$ [4, 9, 10].

2.2 Plasmons and Plasmonics

The Drude–Lorentz model provides a framework for studying the interaction between electrons and electromagnetic waves, whereby the electrons could be a single electron or a group of isolated electrons bound to a central charged ion. However, in metallic systems electrons roam freely without any noticeable force binding them to the positively charged nucleus, which makes their properties remarkably different. For instance, the periodic oscillation of the whole electron gas in a solid around the skeleton of the ions gives rise to a number of interesting physical phenomena such as the collective optical excitations of a solid known as plasmons. Furthermore, the existence

of evanescent surface waves known as surface plasmon polaritons (SPPs) lead to a new type of subwavelength optics, opening the possibility to bridge optics and electronics [11, 12].

In this section we discuss bulk and surface plasmons as well as the absorption and scattering processes for metallic nanoparticles, which are also caused by plasmonic resonance effects. As an example we will show calculated data for silver nanoparticles based on a suitably parametrized Drude–Lorentz model.

A proper analysis or simulation of these phenomena would require the knowledge of fundamental electron gas properties and/or fundamental dielectric properties. This information can be supplied by experimental data as explained in Ref [4, 5].

2.2.1 Bulk Plasmons

Within a metal a cloud of electrons surrounds a fixed skeleton of ions such that the repulsive forces on each ion are minimized. Applying an external electric field distorts the picture and cause local fluctuations in the electron gas, which ultimately lead to collective oscillations called plasmons.

Despite the rapid fluctuation of the electron gas, the overall charge density of the system remains zero. However, at locations where the electrons are oscillating, a local electronic current $\vec{j}$ arise. The continuity equation relates the current $\vec{j}$ to the electronic density ϱ_e and the electric field $\vec{E}$ by:

$$\vec{\nabla} \cdot \vec{j} = -\frac{\partial \varrho_e}{\partial t} = -\varepsilon_\circ \frac{\partial(\vec{\nabla} \cdot \vec{E})}{\partial t} \tag{2.10}$$

Assume that N is the number of charge carriers per unit volume involved in the local electronic current $\vec{j}$, then the current reads

$$\vec{j} = -Ne\vec{v}\,, \tag{2.11}$$

where $\vec{v}$ is the velocity of the electrons in the current.

In the presence of such a current $\vec{j}$, the wave equation has the form [8]:

$$\frac{\partial \vec{j}}{\partial t} + \varepsilon_\circ \frac{\partial^2 \vec{E}}{\partial t^2} = -\frac{1}{\mu_\circ} \vec{\nabla} \times (\vec{\nabla} \times \vec{E}) \tag{2.12}$$

We can further determine $\frac{\partial \vec{j}}{\partial t}$ by going back to Eq. 2.5, which yields

$$\frac{\partial \vec{j}}{\partial t} = -Ne\frac{\partial \vec{v}}{\partial t} = \frac{Ne^2\vec{E}}{m_e} \tag{2.13}$$

Finally the general plasmon equation is obtained;

$$\omega_p^2\vec{E} + \frac{\partial^2\vec{E}}{\partial t^2} = -c^2\vec{\nabla}\times(\vec{\nabla}\times\vec{E}) \,, \tag{2.14}$$

where ω_p is the plasma frequency of Eq. 2.9.

To further analyse the fields associated with the plasmon oscillations, one can split $\vec{E}$ into a longitudinal and transverse component since plasmons are collective excitations, and hence one is dealing with matter waves, i.e. $\vec{E} = \vec{E}_l + \vec{E}_t$.

The longitudinal component $\vec{E}_l$ originates from the charge displacement, which causes the total charge distribution to deviate from its equilibrium value. That results in a new electric field source. Therefore $\vec{\nabla}\times\vec{E}_l = 0$ and $\vec{\nabla}\cdot\vec{E}_l \neq 0$. The plasmon equation becomes:

$$\omega_p^2\vec{E}_l + \frac{\partial^2\vec{E}_l}{\partial t^2} = 0 \tag{2.15}$$

which is the wave equation of a harmonic oscillator. Hence one can quantize the longitudinal oscillations accordingly [8].

A plane wave ansatz $\vec{E}_l = \vec{E}_\circ \exp\left(i\vec{k}\cdot\vec{r} - i\omega t\right)$ for the oscillating electric field of the longitudinal plasmons shows that these modes are actually dispersionless (i.e. ω_p is independent of $\vec{k}$). This is indeed an artefact of the simplifications that were initially made to derive this equation. For instance, a more realistic scenario would include effective masses $m^*(\vec{k})$ and general permittivities $\varepsilon_r(\vec{k},\omega)$ in the expression for ω_p, instead of using m_e and $\varepsilon_\circ$ [10].

Furthermore, the appearance of longitudinal bulk plasmon oscillations depends on some criteria that is derived from the previous equations. For example, the average charge density in the system is zero, which implies that:

$$\vec{\nabla}\cdot\vec{D} = \vec{\nabla}\cdot(\varepsilon_r\varepsilon_\circ\vec{E}) = 0 \tag{2.16}$$

Hence, for longitudinal plasmons with $\vec{\nabla}\cdot\vec{E}_l$ can only happen if $\varepsilon_r = 0$. This criteria also remains valid for the most general types of plasmons based on relative permittivities $\varepsilon_r(\vec{k},\omega)$. Moreover, values that approach zero in ε_r lead to peaks in the loss function $-\operatorname{Im}\left(\frac{1}{\varepsilon_r(\vec{k},\omega)}\right)$.

Note that a longitudinal plasmon oscillation cannot be directly excited by light, which is a transverse electromagnetic wave. However particle beams like the electron beam in an electron microscope can knock off plasmon oscillations, and the resulting plasmon resonances can be used for diagnostic purposes, a technique called electron energy loss spectroscopy (EELS). The probability $P(\vec{q},\omega)$ per unit time that a scattered electron transfers momentum $\vec{q}$ and energy $\hbar\omega$ to the electron gas is given by [13]:

$$P(\vec{q},\omega) = 2\pi \left(\frac{4\pi e^2}{q^2}\right)^2 S(\vec{q},\omega) = -\frac{8\pi e^2}{q^2}\,\mathrm{Im}\left(\frac{1}{\varepsilon(\vec{q},\omega)}\right) \tag{2.17}$$

Here $S(\vec{q},\omega)$ is the structure factor for the scattering of the incoming electron by the electron gas of the bulk solid. Consequently a peak in the loss function corresponds to a large probability of momentum and electron transfer by the incoming electrons, which is exactly what happens during a collective excitation of the electron gas.

For the transverse bulk plasmons, which originates from a charge motion in a fixed background field, $\vec{E}_t$ has $\vec{\nabla}\times\vec{E}_t \neq 0$ and $\vec{\nabla}\cdot\vec{E}_t = 0$. In this case Eq. 2.14 takes the form:

$$\omega_p^2\vec{E}_t + \frac{\partial^2\vec{E}_t}{\partial t^2} = -c^2\vec{\nabla}\times(\vec{\nabla}\times\vec{E}_t) \tag{2.18}$$

Using a plane wave ansatz similar to the one used for longitudinal modes $\vec{E}_t = \vec{E}_\circ \exp\Big(i\vec{k}\cdot\vec{r} - i\omega t\Big)$, one obtains the following dispersion relation:

$$c^2k^2 = \omega^2 - \omega_p^2 \tag{2.19}$$

It is implied that there will be no plasmon oscillations for $\omega < \omega_p$. The transverse nature of these plasmon oscillations $\vec{\nabla}\times\vec{E}_t = 0 = \vec{\nabla}\times((\varepsilon_r\varepsilon_\circ)^{-1}\vec{D})$ also mean that plasmonic modes correspond to poles $\varepsilon_r = \infty$ in the dielectric function $\varepsilon_r(\vec{k},\omega)$. Finally as transverse waves, they can directly be excited by light.

2.2.2 Surface Plasmon Polaritons

The interface between a regular dielectric material (such as semiconductors or insulators) and a metal could witness the formation of evanescent surface charge density waves. These waves are strongly coupled photon–plasmon excitations known as polaritons [14].

To theoretically analyse the system, it is assumed that the dielectric function varies along different directions. In other words, the dielectric function depends on the direction on which it is considered. Mathematically, such dielectric is represented as a tensor $\varepsilon_{r,d}(\omega)$ where $r, d \equiv x, y, z$ axis, and similarly for a metal $\varepsilon_{r,m}(\omega)$. However, to simplify the problem it is often assumed that the dielectric function is uniform and independent of the direction in which the field is propagated. For the case of polaritons the strong interaction between the electromagnetic field and the polarizable matter is characterized by a dielectric constant $\varepsilon_r(\omega)$. Then, the wave equation is obtained from Maxwell's equations:

$$\varepsilon_r(\omega)\frac{\partial^2 \vec{E}}{\partial t^2} = -c^2 \vec{\nabla} \times (\vec{\nabla} \times \vec{E}) \tag{2.20}$$

Following the same approach described in the previous section, and applying a plane wave solution one can reach at a general polariton dispersion relation

$$c^2 k^2 = \varepsilon_r(\omega)\omega^2 \ . \tag{2.21}$$

Surface waves combined with polaritons result into evanescent surface waves called surface–plasmon polaritons (SPPs). The SPP is supposed to propagate into the positive x-direction, where it will decay over time. It will also decay along the z-direction into both materials.

The light-matter interaction can be described on each side of the interface by a general polariton dispersion relation:

$$k_{x,i}^2 + k_{z,i}^2 = \varepsilon_{r,i}\left(\frac{\omega^2}{c^2}\right) \qquad i = d, m \tag{2.22}$$

where d represents the material side, and m is the metallic side. Due to the evanescent nature of the SPPs, the components of $\vec{k}$ are assumed to be complex in both media. At the interface the tangential components of $\vec{E}$, $\vec{H}$ and the normal components of $\vec{D}$ and $\vec{B}$ have to be continuous at each point along the surface [15]. This strongly restricts the components of $\vec{k}$ [8] according to

$$k_{x,d} = k_{x,m} = k_{\text{spp}}, \qquad \frac{k_{z,d}}{\varepsilon_{r,d}} + \frac{k_{z,m}}{\varepsilon_{r,m}} = 0 \tag{2.23}$$

These restrictions can further be used to eliminate the z-components in Eq. 2.22, and then obtain the dispersion relation for the propagation of SPPs in the x-direction:

$$k_{\text{spp}} = k_{\text{spp},1} + ik_{\text{spp},2} = \frac{\omega}{c}\sqrt{\left(\frac{\varepsilon_{r,d}\varepsilon_{r,m}}{\varepsilon_{r,d} + \varepsilon_{r,m}}\right)} = k_\circ\sqrt{\varepsilon_{\text{eff}}(\omega)} \tag{2.24}$$

where $k_\circ$ is the scalar wave vector of an electromagnetic wave in vacuum.

The general analysis of Eq. 2.24 is not trivial due to the presence of the square root of a complex number. However, to simplify the analysis we assume that the imaginary part of the dielectric function on the material side $\varepsilon_{2,d}$ is zero. On the metal side we assume that the real part $\varepsilon_{1,m}$ is negative, and that the imaginary part $\varepsilon_{2,m}$ is very small. The square root in Eq. 2.24 can then be expanded as follow:

$$k_{\mathrm{spp}} = k_{\mathrm{spp},1} + ik_{\mathrm{spp},2} = k_\circ \sqrt{\left(\frac{\varepsilon_{1,d}\varepsilon_{1,m}}{\varepsilon_{1,d}+\varepsilon_{1,m}}\right)} + i\frac{k_\circ}{2}\left(\frac{\varepsilon_{1,d}\varepsilon_{1,m}}{\varepsilon_{1,d}+\varepsilon_{1,m}}\right)^{3/2}\frac{\varepsilon_{2,m}}{\varepsilon_{1,m}^2} + \ldots \tag{2.25}$$

A real $k_{\mathrm{spp},1}$ will result in a propagating surface wave which can be avoided by putting $\varepsilon_{1,m} < -\varepsilon_{1,d}$. However, the latter assumption leads to $k_{\mathrm{spp},1} > k_\circ$, which means that for a given frequency ω, SPPs have a smaller wavelength than the corresponding electromagnetic wave in vacuum, and therefore the SPP needs an extra momentum to be kicked off. For more details see [4] and the references therein.

It is worth noting that SPPs cannot be directly excited by light due to their evanescent character. In fact light has to be coupled into an SPP using a prism or a surface grating since extra momentum is necessary to kick off an SPP and boost the modes frequency to match the light frequency [16]. Once the SPPs have been excited, they give rise to an interesting type of surface optics called plasmonics, which bridges the fields of optics and electronics [17, 18, 16]. In chapter 5 we will study the impact of surface plasmons polaritons on two–dimensional photonic crystals.

2.2.3 Localized Plasmons

The interaction between light and metallic nanoparticles results in a third type of plasmonic phenomena known as localized surface plasmon resonances (LSPRs), or more generally known as localized plasmons (LPs). The interaction of light with metallic nanoparticles with irregular shapes is complex, and modelling the resulting resonances can be quite challenging [19]. Numerical solutions of this problem generally require the use of Finite Difference Time Domain (FDTD) methods explained in Sect. 4.1.2.

Experimentally the formation of localized plasmonic surface waves enhances the field intensity around these metallic nanoparticles. These field enhancements can be quite substantial, and the

frequency ranges for the corresponding plasmonic resonances are strongly dependent on the size, the shape of the particle as well as the dielectric properties of the surrounding medium [16].

In this section we will only focus on spherical nanoparticles in order to simplify the mathematical description of localized plasmons in such systems. Such a spherical metallic particle has a radius R and a relative dielectric function $\varepsilon_{r,m}$. Furthermore it is embedded into a surrounding dielectric material with relative dielectric function $\varepsilon_{r,d}$. The system is excited by a constant electric field $\vec{E}$, which induces a dipole moment $\vec{p} = \alpha\vec{E}$ into the nanosphere. The system is equivalent to a point dipole $\vec{p}$ at the center of the spherical nanoparticle with the following polarizability [6]:

$$\alpha = \frac{4\pi R^3}{3}\frac{\varepsilon_{r,m} - \varepsilon_{r,d}}{\varepsilon_{r,m} + \varepsilon_{r,d}} \tag{2.26}$$

In order to quantify plasmonic field enhancements by such a particle, one can extend the simple dipole picture to the standard scattering scenario of incoming light with frequency ω and wave vector $\vec{k}$ being scattered by a point dipole. The scattering process can be summarized as *extinction* = *scattering* + *absorption* + *luminescence*, which in terms of cross sections reads

$$\sigma_{\text{ext}} = \sigma_{\text{scatt}} + \sigma_{\text{abs}} + \sigma_{\text{lum}} \tag{2.27}$$

Obtaining analytical expressions for the cross sections is not a trivial exercise [19, 16]. However, leaving luminescence effects aside one can obtain formulas for the scattering and absorption cross sections [16]:

$$\sigma_{\text{scatt}} = \frac{8\pi}{3}k^4R^6\left(\frac{\varepsilon_{r,m} - \varepsilon_{r,d}}{\varepsilon_{r,m} + 2\varepsilon_{r,d}}\right)^2 \tag{2.28}$$

$$\sigma_{\text{abs}} = 4\pi kR^3\,\text{Im}\left(\frac{\varepsilon_{r,m} - \varepsilon_{r,d}}{\varepsilon_{r,m} + 2\varepsilon_{r,d}}\right) \tag{2.29}$$

For the proper range of validity of these expressions with respect to the optical theorem see [19]. The approach is a good approximation to observe a general trend; for particles with a large radius R, Eqs. 2.28 and 2.29 indicate that scattering process will dominate over absorption. On the other hand, particles with small radius R tends to enhance the absorption over scattering. This is demonstrated in the FDTD simulation presented in Fig. 2.1b, where a dielectric function was represented using the sum of Lorentzian resonances with parameters $\omega_1 = 0.065815$, $\gamma_1 = 0.31343$, $\sigma_1 = 7.9247$, $\omega_2 = 0.36142$, $\gamma_2 = 0.036456$, $\sigma_2 = 0.50133$, $\omega_3 = 0.66017$, $\gamma_3 =$

0.0052426, $\sigma_3 = 0.013329$, $\omega_4 = 0.73259$, $\gamma_4 = 0.07388$, $\sigma_4 = 0.82655$, ω_5 1.6365, $\gamma_5 = 0.19511$ and $\sigma_5 = 1.1133$. Further details and mathematical models for different geometries can be found in [19].

Example: Determine Cross Sections Using FDTD

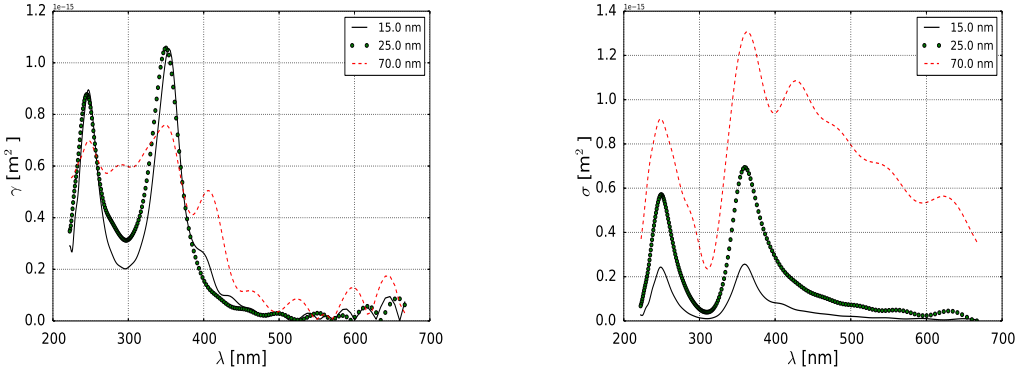

(a) (b)

Figure 2.1: In (a) we show the absorption cross–section and the scattering cross–section in (b) for a simple two-dimensional plane surface with silver sphere positioned in its centre. The simulation is performed using the FDTD method. Three different radii of the sphere, 15, 25 and 70 nm are considered during the simulation.

The computation of the cross section is one of the important aspects of FDTD methods. The cross section is related to the power transmitted through a unit surface area, and it is defined as the ratio between the power P and the field intensity. In terms of units, the cross secion has the units of area; cross section $= \frac{\text{power}}{\text{intensity}}$ (units: $\frac{J/S}{J/S.m^2} = m^2$).

The power P that goes through a surface S is given by the real part of the integral of the Poynting vector over the surface S

$$P(\omega) = \mathrm{Re} \oiint_S \vec{E}(\omega, \vec{r}) \times \vec{H}(\omega, \vec{r}) \cdot \mathrm{d}\vec{A}\,, \tag{2.30}$$

where the fields $\vec{E}$ and $\vec{H}$ are specified at a given spatial point $\vec{r}$ and frequency ω.

One problem is the fact that the FDTD technique simulates the propagation of the fields in space and time. In order to calculate the power spectrum $P(\omega)$, the fields have to be transformed into

to the frequency domain. To perform the calculations one has to use a short–pulse source, which covers the range of the frequencies at which the cross sections are required to be calculated. Then the fields that propagate out of the surface S are stored for each time step. Then one can perform a Fourier transformation according to

$$\vec{\tilde{E}}(\omega) = \frac{1}{\sqrt{2}} \sum_n e^{i\omega n \Delta t} \vec{E}(n\Delta t)\Delta t \ , \tag{2.31}$$

which is known as discrete–time Fourier transformation. It is the preferred technique used by MIT Electromagnetic Equation Propagation (MEEP), but other methods to extrapolate Fourier transforms can be used as well. For details and further references see [20].

2.3 Summary

In this chapter we reviewed the aspects of light–matter interactions. We covered the frequency–dependent dielectric function and provided a derivation of the Drude–Lorentz model within the framework of Ehrenfest theorem. Furthermore, the interaction between electromagnetic waves and electrons was discussed in metallic systems where the electrons move freely around positively charged ions, which results in the bulk plasmon excitations.

At the interface between a metal and a dielectric material a new class of plasmons known as surface plasmon polaritons exist, which opens the door for a new set of applications that bridges the field of optics and electronics.

Moreover, the topic of localized surface plasmon resonances was covered in this chapter, where we finally presented a simple numerical simulation to compute the scattering as well as the absorption cross sections for a spherical silver nanoparticle. In the following chapter we lay the foundation of the numerical techniques used throughout this work.

3. Photonic Crystals

The ability to control fundamental forces and the flow of their elementary particles has always been a desire for mankind as it give rise to important technological application. For example, semiconductors control the flow and the propagation of electrons in materials [21]. They allow electrons with certain energies to flow through a device and block other electrons, as discussed in the previous section. The ability to control electrons has lead to an industrial revolution and resulted in manufacturing very sophisticated semiconductor technologies.

On the other hand, understanding the optical properties of materials that have the ability to control the propagation of photons has received much less attention. The fascination with the electronic properties of solids and the search for materials that exhibit novel properties has been in the front for long time. However, in 1987 Eli Yablonovitch and Sajeev John published two ground breaking papers that highlight the link between semiconductors and photonic crystals (PCs) [22, 23]. The term photonic crystals was coined by Yablonovitch himself.

For the past three decades the field of photonic crystals (PCs) is growing almost exponentially. The fabrication techniques have improved dramatically, which opens the doors for a lot of interesting practical applications. Photonic band gaps play a central role in a wide range of applications such wavelength selective filters, mirrors, optical resonators, point defect laser, optical waveguides, optical multiplexer and optical fibres. Moreover, PCs are used for optical time delay devices, dispersion compensation, distributed feedback laser and negative refractive index lenses [24, 25, 26, 27, 28].

3.1 Photonic Band Gap

The periodic arrangement of dielectric elements in bulk materials in 1D, 2D and 3D forms photonic crystals (PCs) in a manner similar to that of atoms and molecules in solids. This periodicity of dielectric elements in PCs makes them similar to their electronic counterparts in many ways. One of the most interesting properties of photonic crystals is the opening of a photonic band gap due to the specific geometry and the dielectric properties of the dielectric components.

The quantum theory of solids assumes that the atoms and the molecules in a crystal can be replaced by a potential that repeats itself periodically across the lattice. The propagation of the electrons in such media is ruled by different factors that include the geometry of the lattice structure and the type of the potentials involved. Conductors, for example, have electrons that move freely like electrons in a free electron gas, while semiconductors limit the motion of conducting electrons to those that acquire certain energies within a specific range. Usually the semiconducting materials have a prohibited range of energies where, electronic states do not exist, which is known as the electronic band gap [29].

In analogy to solids, dielectric elements like spheres or rods correspond to the atomic constituents of solids. Due to translational symmetry, the solution of Maxwell's equations yields photonic bands similar to those of the electronic systems. In other words, PCs form photonic states where photons are allowed to propagate through the entire PC and photonic band gaps where photons with the frequencies that fall in the range of the band gap may not propagate in all directions, if allowed to propagate at all [30].

The photonic band gap is at the core of every search for dielectric structures that can potentially be used in different photonic applications. For instance, 1D photonic crystals that consist of layers that are made of two different dielectric materials, will always have a band gap as long as the two layers have different dielectric functions with a suitable contrast. Such crystals can act as a Bragg mirror for frequencies within the gap [31]. It also has the ability to localize modes when defects are present. A multilayer film made of GaAs alternating with air layers has a wide band gap which makes it a suitable structure for filtering devices [30].

In two–dimensions things are slightly different. A key difference is the fact that 1D structures are periodic along one axis (say z-axis for example). The 2D crystals, on the other hand, are periodic in a plane (say x-y plane in this case) which adds additional constraints on the wave vector $\vec{k}$. To demonstrate those constraints, a 1D multilayer film would have a restriction on the $\vec{k}_z$. In the 2D PCs the wave vectors parallel to the plane $\vec{k}_{\|}$ are restricted to the Brillouin zone which is the periodicity direction, however, the $\vec{k}_z$ vector has no restrictions and modes along that axis propagate freely.

Moreover, the mirror symmetry in such systems allows the separation of the electromagnetic

modes into two components; transverse–electric (TE) and transverse–magnetic (TM) modes. The former has the magnetic field $\vec{H}$ perpendicular to the plane, while the later has the electric field $\vec{E}$ perpendicular to the plane. That gives higher dimensional crystals the advantage of forming band gaps for a specific polarization as shown in Fig. 3.1a, where only TM modes have a band gap.

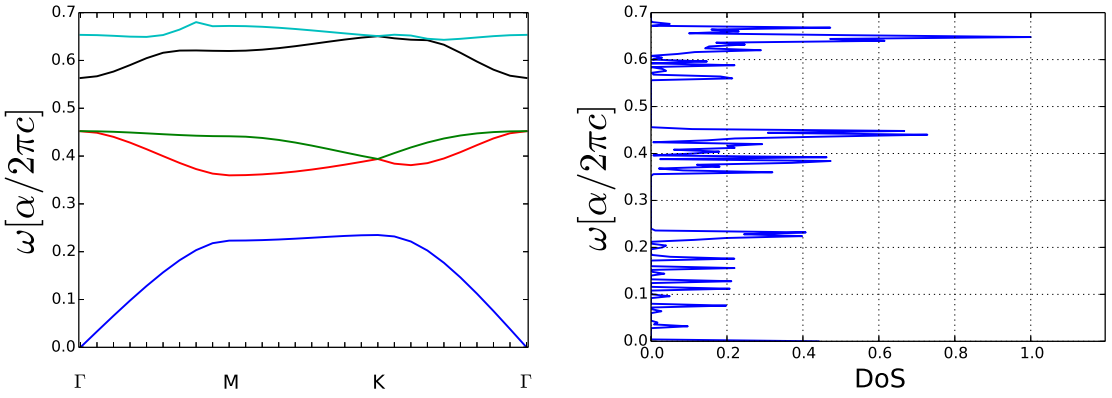

(a) (b)

Figure 3.1: (a) TM modes in units of $(2\pi c)/\alpha$ for a honeycomb photonic crystal. In (b) we show the corresponding scaled density of states (DoS).

Fig. 3.1a depicts the transverse magnetic mode (TM) band structure for a two dimensional honeycomb lattice. The lattice points are populated with cylindrical objects of radius 0.2α, where α is the lattice constant. It is quite convenient to represent all bands in Fig. 3.1a in units of α, which stems from the fact that Maxwell's equations for systems with frequency–independent dielectric functions are scale–invariant [30]. The cylindrical objects on the lattice consist of a dielectric material of dielectric constant 13. The background medium is air (i.e. dielectric constant equal to 1). The bands are obtained using the frequency domain method implemented in MPB [32].

Band gaps are observed between $\omega \sim 0.24\ [(2\pi c)/\alpha]$ and $0.35\ [(2\pi c)/\alpha]$, and $\omega \sim 0.46\ [(2\pi c)/\alpha]$ and $0.55\ [(2\pi c)/\alpha]$, which can also be seen in the density of states related to the band structure in Fig 3.1b.

The scale–invariant character of Maxwell's equations makes PCs distinct from other solids in the sense that PCs maintain the same optical properties for different scales. To elaborate, a crystal

with a band gap at frequency ω will maintain the band gap and all band structure characteristics when the size of the lattice unit vector changes. That is mainly the reason why frequencies are usually given in terms of the lattice unit vector α as we saw in the previous examples. This, however, breaks down when the crystal building blocks do not have a constant dielectric function, in other words, the dielectric functions depends on the frequency. Such a case is addressed in a separate chapter.

3.1.1 Photonic Band Gap and the Colours of the Chameleon

Photonic crystals also appear in nature. Here we give a very illustrative example, which is the changing colours of the chameleon. The ability of the chameleon to change colours has always been a topic of great interest. A recent study proposed a model, where a three–dimensional photonic crystal was used to explain the different colours seen at different angles [33]. The authors suggested that the chameleon gets and changes its colours by controlling the dimensions of skin cells, which form a photonic crystal. Similar to a complete band gap, photonic band gaps along certain directions can also act as mirrors, which filter out electromagnetic modes with specific frequencies along that particular direction.

Figure 3.2: A chameleon displaying a fascinating range of colours. The image was taken from Pixabay and it is licensed under Creative Commons CC0.

To model the problem, the chameleon's skin is considered to be a dielectric structure, which

consist of spheres lined up side by side, which forms a 3D opal crystal. The radius of each of the spherical objects in the crystal is fixed, but the lattice constant of the opal itself varies. This is a simulation of a chameleon which relaxes or stretches its skin. A relaxed skin would correspond to a smaller lattice constant, while stretching the skin is effectively the equivalent of increasing the lattice constant.

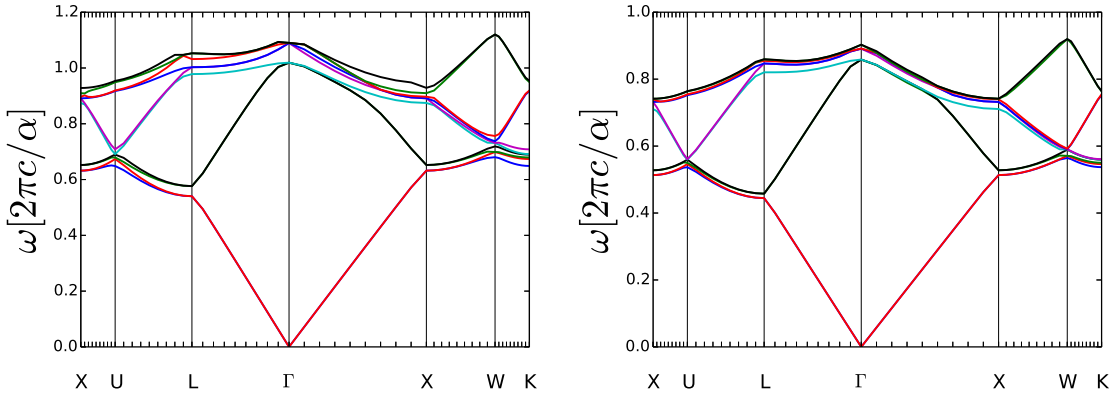

Figure 3.3: The band structure for 3D opal lattice with spherical objects. The spheres have a dielectric constant of 3.35 and radii of 0.76 μm. The background dielectric constant is 1.77. In (a) the band structure is computed for a lattice constant $\alpha = 1.88$ μm while (b) is for $\alpha = 2.55$ μm.

In Fig. 3.3, we show the photonic band structure for an opal lattice with spheres of dielectric constant 3.35 and background material of dielectric 1.77. The spheres have a radius of 0.76 μm. In Fig. 3.3a the lattice constant is 1.88 μm, which corresponds to a chameleon with a relaxed skin. In Fig. 3.3b we present the band structure for lattice constant $\alpha = 2.55$ μm, which represent a chameleon with a stretched skin [33].

Although both structures in Fig. 3.3 do not demonstrate a complete band gap, they have directional band gaps. For example in Fig. 3.3a one of the directional band gaps appear along the U – L axis at approximately 0.58 – 0.62 $2\pi c/\alpha$. In terms of metric units, these frequencies are equivalent to 581.2 – 621.1 THz for a lattice constant 1.88 μm. That means along the U – L axis the colours reflected are cyan – blue. Changing the lattice size results in a shift in the bands to lower frequencies as well as the closure of the band gap as seen in Fig. 3.3b. This method

gives a rough estimate of the colours of the chameleon. A better approach will be the calculation of the reflectance and CIE values [34] in colour spaces to identify the colours perceived by the human eye, which gives more realistic predictions. However, the topic is beyond the scope of this thesis.

3.2 Plasmonic Photonic Crystals

The interaction between the free electrons and the optical electromagnetic waves at the interface between a metal and a dielectric material results in evanescent electromagnetic waves known as surface plasmon polaritons. Due to their evanescent character the wavelength of SPP can be shorter than the wavelength of their optical counterparts in the dielectric medium [35, 12, 36, 11].

Similar to light, the surface plasmons can also be manipulated by a photonic crystal placed on a metallic surface, a system better known as plasmonic photonic crystal. The decaying surface plasmon polaritons at the interface between the heterogeneous dielectric metamaterial and the metal influence the dielectric properties of photonic crystals by introducing non-linearities [37], which can localize certain photonic modes. Furthermore, the plasmonic photonic crystals can enhance the optical properties of a regular photonic crystal [36].

SPP waves play an important role in the field of photonics due to their potential applications and interesting physics. In previous studies Raman scattering is enhanced using the localized surface plasmon resonance [38]. Also surface plasmons can enhance the absorption of light which can be used to improve the efficiency of solar cells [39]. For plasmonic photonic crystals a band gap is found to open at a specific frequency range in periodic structures due to Bragg resonance at the boundaries of the Brillouin zone, leading to the development of waveguides [40, 41], high efficiency Bragg reflectors and resonators [42, 43]. Moreover, a one-way waveguide can be achieved under static magnetic fields [44].

In chapter 5, a particular case of plasmonic photonic crystals is examined. The problem is treated using perturbation theory whereby a brief description of a suitable perturbative scheme is developed. Then the results of the photonic band structure of a 2D dielectric honeycomb crystal placed on an aluminium surface are presented.

3.3 Localization in Photonic Crystals

In a seminal work published in 1958 by P. Anderson [45], the author argued that for a highly disordered crystal the electronic states can be confined in a particular region due to wave scattering. Such a localized wave will decay exponentially over space. Consequently, a metallic system can turn into an insulator, because its conduction electrons become localized. This is not really covered by Blochs theorem, which would still postulate extended states under the same conditions. Although localization was initially proposed as a phenomena associated with electronic systems, it turned out to be a generic wave phenomena, which can be observed in other wave systems including optical materials [46].

To understand the origin of the localization phenomena one has to understand the physics of waves. In a medium with scatterers such as atoms in the case of solids or dielectric elements in the case of photonic crystals, waves can not propagate freely without encountering a scatterer. The distance travelled by the wave before being scattered is known as the mean free path. The size and the density of the scatterers in addition to the wavelength of the wave in the media are essential in determining the type of the scattering; weak scattering occurs when the density is low and the scatterer–scatterer separation is large compared to the wavelength, and strong scattering occurs when the separation between the scatterers is small compared to the wavelength [46].

Scattering can be characterized by two different types. Elastic scattering refers to the scattering of waves that preserve their frequency but not their direction after being scattered. Inelastic scattering deals with scattering processes that alter both, the frequency and the direction of propagation of a scattered wave.

Scattering where the frequency is maintained but the direction is reversed is called coherent backscattering, and its phase is preserved in that particular direction, which usually leads to an enhancement in the backscattering by constructive interference. Such enhancement in turn impacts the diffusive wave transport negatively. To further clarify the concept, a medium with a long mean free path has weak scattering, and hence a weak backscattering. Short mean free path corresponds to an enhanced backscattering, which can cease the waves from propagating leading to mode localization.

To quantify localization, one has to consider the size of the sample since the backscattering is dependant on the distance between the scatterers as well as the wavelength. Thus, for a sample with a high density of scatterers and a large size, the wave propagation in such media is likely to slow down, and measurable quantities such the transmission coefficients will decay exponentially. For smaller samples the wave diffusion will decrease but a complete freeze out of the wave motion will not be reached. The correlation between size and localization introduces a new fundamental length known as the localization length (ξ) which plays an important role in the transport theory in solids [47].

For example, in a 1D multilayer film the transmission coefficients τ can be modelled using the transfer matrix method. The transmission coefficients are the product of all transmission coefficients for the segments forming the film [46],

$$\tau = \prod_{i=1}^{N} \tau_i \tag{3.1}$$

where N is the index of the last segment. Moreover, one can infer from the relationship in Eq. 3.1 that each scattering event is independent and hence $\ln|\tau_i|$ is additive. In terms of the localization length the transmission function is expressed as:

$$|\tau|^2 = e^{-2L/\xi} \tag{3.2}$$

where L is the thickness of the film. The localization length ξ is then written as:

$$\xi = \frac{-2L}{\sum_{i=1}^{N} \ln|\tau|^2}. \tag{3.3}$$

Statistically speaking, the term $\ln|\tau|^2$ has a Gaussian distribution, since it is independent of any particular scattering and it essentially varies as a random variable. That impacts the computed value of $\ln|\tau|^2$, and high accuracy is achieved for film with $L \longrightarrow \infty$.

Introducing localization brings forward the dimensionality of the structure as a major player in quantifying all measurable quantities. This is in contradicting to diffusive transport, where the transmission is completely independent of the size of the sample.

In photonic crystals disorder can cause the optical modes to be trapped at sites containing the defects. In 2D crystals such defects are found to play a critical role in tuning their properties; in the case of linear defects the modes can be trapped along the defects direction creating guided bands. Point defects have the ability to trap photons with frequencies close the band gap frequencies without accounting for the direction of the incident wave. The later case is examined and analysed in chapter 7.

On the other hand, aperiodic structures such as photonic quasicrystals (PQCs) are found to have richer properties, due to the abundant number of geometries and the breaking of lattice symmetries. With that, however, comes another computational difficulty. Later in chapter 6 we will discuss the development of numerical techniques to compute and quantify the optical localization of 2D PQCs.

In the next chapter we review the numerical foundations of computational electromagnetism with focus on the two major techniques; the finite–differences–time–domain method (FDTD) and the frequency–domain method (FD). The mathematical details of each method are described in some details with simple examples illustrating the technical background.

4. Numerics

The physics of real systems often requires the solution of very complex equations. For most of these systems analytical solutions do not exist, and the need for accurate numerical solutions arises. Numerical methods have played a major role in the development of all applied sciences, and not only for Physics. Alongside the development of powerful computers it was also the development of new algorithms that allowed for us to tackle very complex tasks efficiently, and with very high accuracy [48].

For systems that are described by partial differential equations, such as electronic (Schrödinger equation) and photonic (wave equation derived from Maxwell's equations) systems, different numerical techniques have been developed in order to make accurate predictions about their physical properties. In the following sections we summarize some of the most popular numerical techniques used to simulate photonic systems on various length and time scales. Further details on the topic can be found in [5] and the references therein.

4.1 Basic Techniques

We start with mesoscopic/macroscopic optical systems. The numerical simulation of such systems is based on wave equations, which can directly be derived from Maxwell's equations. Knowing the properties of the basic materials forming a given system in terms of their relative permittivities and permeabilities, one can make very precise predictions even for relatively complex optical systems, because the underlying equations are mostly linear. The most popular numerical techniques in this area are the finite–differences–time–domain method [49], spectral methods [50], block iterative methods [32] and block-pseudospectral methods [51], just to name a few. Each of these methods has its advantages and disadvantages. We will limit our discussion to only two methods, which are the frequency domain method described in Sec. 4.1.1, and the finite-differences time-domain (FDTD) method described in Sec. 4.1.2.

Permeabilities and permittivities have their origin in light-matter interactions at the atomic level (i.e. nanoscale). In order to make accurate predictions about plasmonic systems on the nanoscale,

simple models like the Drude–Lorentz model described in Sec. 2.1 cannot be used any more. One has to solve the many–body Schrödinger equation for a bulk system excited by electromagnetic radiation. Although these basic equations can be formulated quite easily, it is also well known in quantum mechanics that they will not have analytical solutions for even the simplest type of nano–systems or molecules. Numerical solutions are a formidable challenge as well, due to the non–linear nature of the effective one–particle equations derived from the many–body Schrödinger equation [52, 53].

4.1.1 Frequency Domain Methods for Periodic Systems

Periodic systems such as photonic crystals, waveguides and resonant cavities give rise to electromagnetic modes that have analytical properties similar to electronic states in periodic solids [30]. They are described by a general wave equation, which can be directly derived from Maxwell's equations.

A fundamental technique in understanding the optical properties of these particular modes is a decomposition into harmonic time–dependant eigenmodes. Frequency domain (FD) methods as a special case of these decomposition methods will expand electromagnetic fields into Fourier eigenmodes, which is often sufficient to understand the characteristics of optical materials in the absence of non–linear effects [32]. FD methods usually start from basic photonic systems with translational symmetry, for which the solution of Maxwell's equations and the derived wave equations will give rise to electromagnetic Bloch states and related photonic band structures [30].

In the following we will discuss the numerical details for computing the photonic band structures using FD schemes. We will show that under the particular assumptions of the FD schemes, the solution of the wave equation will become equivalent to a matrix eigenvalue problem, which is one of the standard problems of numerics, and for which there are very powerful numerical methods available [32]. Some of the technical problems of the FD scheme will be pointed out as well.

Photonic Band Structures

To find the eigenmodes using the frequency domain method, a general equation describing the propagation of electromagnetic waves in matter has to be mapped onto an eigenvalue problem. For a linear dielectric function $\varepsilon(\vec{r})$ we may derive general wave equations for the electric and magnetic components of the propagating waves, which of course follow from Maxwell's equations [30]. For the magnetic field $\vec{H}$ the corresponding wave equation will be

$$\nabla \times \frac{1}{\varepsilon} \times \nabla \times \vec{H} = \frac{1}{c^2} \frac{\partial^2}{\partial t^2} \vec{H} \; , \tag{4.1}$$

The solution $\vec{H}$ is constrained by the transversality condition

$$\nabla \cdot \vec{H} = 0 \; . \tag{4.2}$$

For the solution of Eq. 4.1 and Eq. 4.2 we only consider time–dependant periodic solutions $\vec{H}(t)$. Taking into account the translational symmetry of a periodic photonic system described by $\varepsilon(\vec{r})$, the magnetic modes represents the eigenstates of Eq. 4.1. That is similar to the Bloch states of electrons in a solid [29], as explained in the following.

For magnetic modes the corresponding electromagnetic Bloch states are

$$\vec{H}(\vec{k}, \vec{r}) = e^{i\left(\vec{k} \cdot \vec{r} - \omega t\right)} \vec{H}_{\vec{k}}(\vec{r}) \; , \tag{4.3}$$

where $\vec{k}$ is a Bloch wavevector (which is a pseudomomentum [29]), and $\vec{H}_{\vec{k}}$ is an amplitude factor that gains its periodicity from the periodicity of the underlying photonic system. Substituting the Ansatz of Eq. 4.3 into Eq. 4.1 results in

$$\left(\nabla + i\vec{k}\right) \times \left(\frac{1}{\varepsilon}\left(\nabla + i\vec{k}\right) \times \vec{H}_{\vec{k}}\right) = \left(\frac{\omega}{c}\right)^2 \vec{H}_{\vec{k}} \; . \tag{4.4}$$

The operator on the left hand side of Eq. 4.4 is a positive semi–definite Hermitian operator, and Eq. 4.4 is a typical Hermitian eigenvalue problem with eigenvalues $\left(\frac{\omega}{c}\right)^2$. By introducing a complete set of basis states $\left\{\vec{\Psi}_i(\vec{r})\right\}_i$ and using $\vec{H}_{\vec{k}} = \sum_i h_i \vec{\Psi}_i(\vec{k})$, we can map this eigenvalue problem on a standard (Hermitian) matrix eigenvalue problem:

$$A \, \vec{h}\vec{\Psi} = \left(\frac{\omega}{c}\right)^2 B \, \vec{h}\vec{\Psi} \tag{4.5}$$

where A is the Hermitian operator on the left hand side of Eq. 4.4 and $\vec{h}$ represents the coefficient vectors $(h_1, h_2, \ldots h_m)$. The matrix operator A is a result of the discretization of the momentum space used in the simulation. The matrix element A_{lm} is given by $\vec{\Psi}_l^\dagger A \vec{\Psi}_m$ and B_{lm} is $\vec{\Psi}_l^\dagger \vec{\Psi}_m$. These products involve integration over the configuration space, in analogy to matrix elements in quantum mechanics [30].

Note that due to the $\vec{k}$ dependence of the Bloch states $\vec{H}_{\vec{k}}(\vec{r})$, the frequencies ω derived from the eigenvalue problem are also $\vec{k}$ dependent, i.e. $\omega = \omega(\vec{k})$. One usually solves the eigenvalue problem for a series of selected $\vec{k}$ vectors, and then interpolates in between these points to obtain the photonic band structure. See Fig. 3.1a as an example.

Numerical Details

The fields $\vec{H}_{\vec{k}}$ in Eq. 4.4 can be written as a linear expansion of basis vectors $\vec{\Psi}_i$ [32]

$$\vec{H}_{\vec{k}} = \sum_{i=1}^{\infty} h_i \vec{\Psi}_i \,, \tag{4.6}$$

where h_i represents the expansion coefficients, which form a column vector $\vec{h}$ in the matrix formulation of the eigenvalue problem of Eq. 4.5. From a computational point of view, it is impossible to calculate every single coefficient in the infinite sum that represents the field $\vec{H}_{\vec{k}}$. Therefore this sum must be truncated at a sufficiently small number N, which should still yield a very good approximation to the exact $\vec{H}_{\vec{k}}$.

Terminating the sum in Eq. 4.6 at a number N of basis functions also reduces the size of the column vectors and of the matrix operators to finite sizes of $N \times 1$ for the column vector and $N \times N$ for the matrix sizes. But this mapping on a matrix eigenvalue problem does not necessarily provide a solvable problem in practice; in particular when a traditional linear algebra approach is used to solve the matrix eigenvalue problem. The matrices involved could just be too large, which requires enormous amounts of computer memory, and the algorithms involved will basically never finish.

Fortunately, in most cases only a few lower eigenvalues or photonic bands are necessary to understand the interesting physics behind periodic optical systems like photonic crystals [30]. Then one does not have to solve for the entire spectrum of the eigenvalue problem, and the

interesting bands are computed using a suitable iterative method. This approach also has a very positive impact on the computer memory needed by a typical FD scheme.

The iterative solution of the eigenvalue problem starts off with an initial guess of the eigenvector $\vec{H}$ (neglecting all labels for the moment being). Then one iteratively improves this guess, based on the fact that for all Hermitian operators the smallest eigenvalue λ satisfies

$$\lambda = \min_{\vec{H}} \frac{\vec{H}^{\dagger} A \vec{H}}{\vec{H}^{\dagger} B \vec{H}} \; . \tag{4.7}$$

This type of problems is better known as the Rayleigh-quotient, which can perfectly be solved using a preconditioned conjugate–gradient method [54]. The best description of this technique would be band–by–band minimization. It has been applied quite extensively in the study of electronic solids [55]. An interesting aspect of this method is the fact that we do not have to store the full matrices A and B in order to solve the minimization problem of Eq. 4.7. In fact the conjugate gradient method only requires the storage of the products $A\vec{\Psi}$ and $B\vec{\Psi}$, which saves a lot of computer memory.

The minimization of Eq. 4.7 leads to the determination of an eigenvalue λ and the related frequency ω, and we also obtain an eigenvector $\vec{H}$. This is the lowest band at a given $\vec{k}$ point. To obtain the next band values for the following frequency, we repeat the minimization in Eq. 4.7, but for a new trial eigenvector $\vec{H}'$, which is constrained to be transverse and orthogonal to the lowest eigenvector $\vec{H}$. Hence the band structure may be obtained on the basis of a band-by-band minimization technique using the preconditioned conjugate–gradient method.

At this point it is worth noting that due to the periodicity of the photonic system, a plane wave basis $\vec{\Psi}_i$ seems to be a natural choice. To elaborate, for a periodic system Bloch theorem states that the eigenstate $\vec{H}$ can be expressed as a product of a plane wave and a function with the periodicity of the lattice:

$$\vec{\Psi}(\vec{r} + \vec{R}) = e^{(i\vec{G}\cdot\vec{r})} \vec{\Psi}(\vec{R}) \tag{4.8}$$

where $\vec{G}$ is a wave vector, $\vec{R}$ and $\vec{r}$ are vectors that represent two points in the real (configuration) space They are usually expressed in terms of a fundamental set of vectors known as the unit vectors $\hat{r}_j$ and an integer n_j,

$$\vec{r} = \sum_{j=1}^{3} n_j \hat{r}_j \; . \tag{4.9}$$

At the boundaries of a lattice, periodic boundary conditions are often imposed on the wave function, which leads to the conclusion that the exponent $\exp\left(i\vec{G}\cdot\vec{r}\right) = 1$. For this condition to be satisfied, $\vec{G}\cdot\vec{r}$ has to equal $2\pi n$ where $n = 0, 1, 2, \ldots$ [29].

The vectors $\vec{G}$ are related to the fundamental lattice vectors $\hat{G}_i$ in reciprocal space by

$$\vec{G} = \sum_{i=1}^{3} m_i \hat{G}_i \ , \tag{4.10}$$

where m_i are integers. One can easily switch between the grid in real and reciprocal space using Fast Fourier Transform (FFT) routines [30], which is also useful for evaluating the vector operators in Eq. 4.4. By switching from real to reciprocal space, the curl operator $\vec{\nabla}$ becomes $\vec{k} + \vec{G}$. Switching back from reciprocal to real space, one can easily carry out the successive multiplication by ε^{-1}. Given the speed of the standard FFT routines, the operations on the left hand side of Eq. 4.4 can actually be carried out very efficiently.

The simplification of Eq. 4.4 by putting the modes on a grid in real space comes with its own problems, which are related to the inverse dielectric function ε^{-1}. The later has to be evaluated on a real space grid as well, and irregular geometries at the interface between two dielectric media might not be covered by a moderate discretization grid in real space, leading to all sorts of numerical artefacts.

In order to avoid such problems, the dielectric function close to the interface has to be averaged. The most successful procedure is based on effective–medium theory [56]. If $\hat{n}$ is taken as the vector normal to the surface and P is the projection operator onto $\hat{n}$, then the effective inverse dielectric constant $\tilde{\varepsilon}^{-1}$ for one unit of a cubic discretization grid is given by:

$$\tilde{\varepsilon}^{-1} = \overline{\varepsilon^{-1}} P + (\bar{\varepsilon})^{-1}(1 - P) \tag{4.11}$$

where the first term on the right hand side of Eq. 4.11 is the average of the inverse dielectric function projected onto the surface normal. That term is the dominant term when the incident field is parallel to the surface normal. The second term is the inverse of the averaged dielectric function, and this contribution dominates when the field is perpendicular to the normal of the surface. Other than for the dielectric media, this averaging plays no role, and we can just take the usual inverse of the dielectric constant at a particular grid point. For further details see [32].

4.1.2 Time Domain Methods

The finite difference time domain method (FDTD) is a grid–based method similar to finite difference approaches [57] used to solve partial differential equations. In FDTD, Maxwell's equations are discretized using central differences with respect to the space and time derivatives. The resulting set of equations are solved in a leapfrog manner on a staggered grid, a technique which is also quite popular in fluid dynamics [48].

For the sake of simplicity, we will only describe the basic mathematical formalism and some of the numerical details in one spatial and one temporal dimension. The corresponding formalism in four dimensional space–time can be found in [49].

Outline of the FDTD method

The frequency–domain methods are very successful to understand the properties of periodic systems like photonic crystals. But in order to examine a finite system, one has to use a supercell approach, which easily becomes very expensive from a numerical point of view. In such cases one needs a more robust numerical technique suitable for such systems, which is provided by the finite difference time domain method (FDTD).

In general, FDTD has some distinct advantages over the frequency–domain scheme. For instance, FDTD simulates the propagation of the electromagnetic wave in the dielectric medium itself, rather than going over a linear algebra problem. That way it becomes much easier to simulate very complex geometries, as well as non–linear media, in contrast to the FD scheme.

The key idea of the FDTD is the staggering of the vector components for the electric fields $\vec{E}$ and the magnetic fields $\vec{H}$. This is called a Yee lattice being a tribute to Kane Lee, who pioneered the method [58]. The Yee lattice represents the physical space where the electromagnetic waves propagate, and a 2D example is shown in Fig. 4.1 . In order to describe the wave propagation on this grid, Maxwell's equation have to be discretized as well.

Let us base our analysis on a very general version of Maxwell's equations. As we are interested in wave phenomena, we can assume that there are no source terms. However, there could be electric and (artificial) magnetic currents characterized by electrical conductivities σ and magnetic

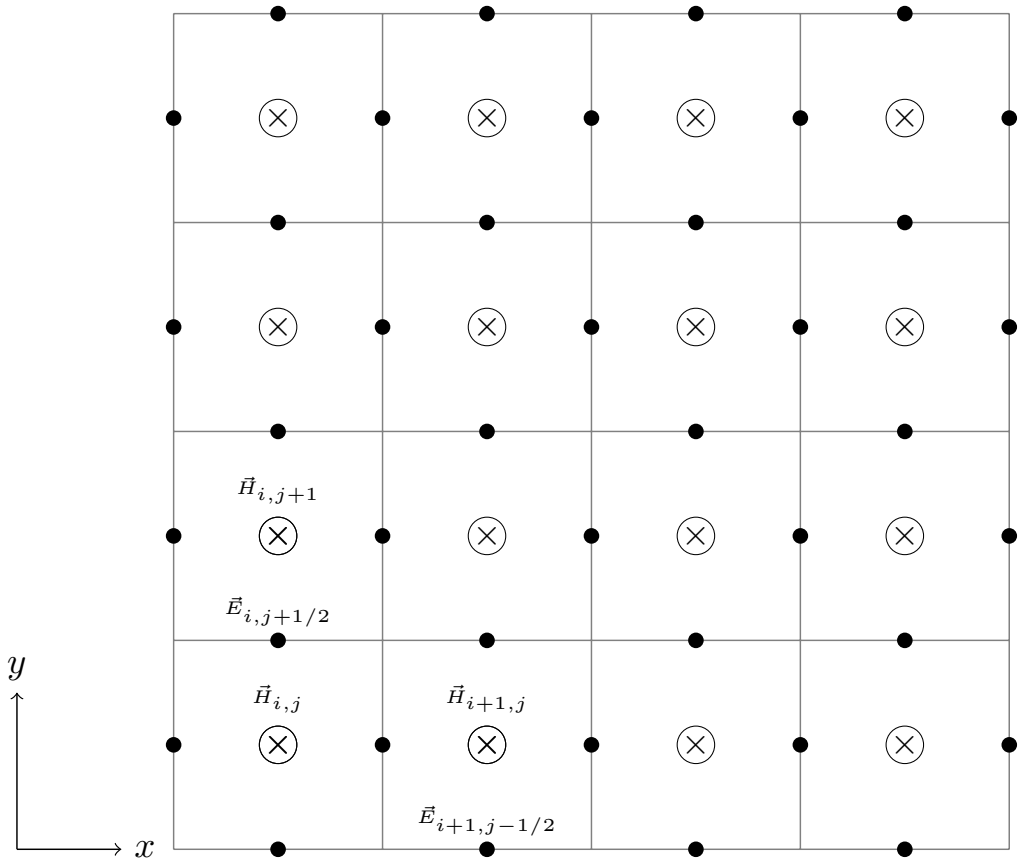

Figure 4.1: Two-dimensional Yee lattice. The solid points represent the electric field $\vec{E}$ and the $\times$ points represent the magnetic field $\vec{H}$. The electric field propagates in the x-y plane while the magnetic field is perpendicular to $\vec{E}$. At the bottom left we refer to the coordinates of the magnetic field as i, j. The neigbouring solid point in the y direction represents an electric field, which has coordinates $i, j + 1/2$.

resistivities ϱ. Thus:

$$\frac{\partial \vec{H}}{\partial t} = -\frac{1}{\mu}\nabla \times \vec{E} - \frac{\varrho}{\mu}\vec{H} \tag{4.12}$$

$$\frac{\partial \vec{E}}{\partial t} = \frac{1}{\varepsilon}\nabla \times \vec{H} - \frac{\sigma}{\varepsilon}\vec{E} \tag{4.13}$$

where ε is the electrical permittivity, and μ is the magnetic permeability.

Let us simplify Eqs. 4.12 and 4.13 by restricting the field propagation to the z-direction. Then

for the different allowed vector components of $\vec{E}$ and $\vec{H}$ these equations will simplify to

$$\frac{\partial E_x}{\partial z} = -\mu \frac{\partial H_y}{\partial t} - \varrho H_y \tag{4.14}$$

$$\frac{\partial E_y}{\partial z} = \mu \frac{\partial H_x}{\partial t} + \varrho H_x \tag{4.15}$$

and

$$\frac{\partial H_x}{\partial z} = \varepsilon \frac{\partial E_y}{\partial t} + \sigma E_y \tag{4.16}$$

$$\frac{\partial H_y}{\partial z} = -\varepsilon \frac{\partial E_x}{\partial t} + \sigma E_x \ , \tag{4.17}$$

Although the fields $\vec{E}$ and $\vec{H}$ retain their vector character in 3 dimensions, the problem is now effectively one-dimensional, because the fields can only vary in time, and in the z direction. We now introduce the general notation for the discretization scheme used in FDTD, and formulate our simplified numerical setting in this form. Let the indices i, j and k represent the increments in the three spatial coordinates as depicted in Fig. 4.1. Then for a point on the grid the x-coordinates is given by $i\Delta x$ where i takes an integer value and Δx is the size of the grid cell in that particular direction. Furthermore, the fields are time-dependant and they have to be discretized accordingly. For this purpose, we take the time increment to be n and the time step to be Δt. The discretized Eqs. 4.14 – 4.17 read

$$\begin{aligned}
\frac{E_x^{i,j,k+1/2} - E_x^{i,j,k-1/2}}{\Delta z} &= -\frac{\mu_{xy}^{ijk}}{c_\circ} \frac{H_y^{i,j,k}|_{n+1/2} - H_y^{i,j,k}|_{n-1/2}}{\Delta t} \\
&\quad - \varrho_{xy} H_y^{i,j,k}|_{n-1/2} \\
-\frac{E_y^{i,j,k+1/2} - E_y^{i,j,k-1/2}}{\Delta z} &= -\frac{-\mu_{xx}^{ijk}}{c_\circ} \frac{H_x^{i,j,k}|_{n+1/2} - H_x^{i,j,k}|_{n-1/2}}{\Delta t} \\
&\quad + \varrho_{xy} H_x^{i,j,k}|_{n-1/2}
\end{aligned}$$

and similarly for the magnetic field

$$\begin{aligned}
-\frac{H_y^{i,j,k}|_{n+1/2} - H_y^{i,j,k-1}|_{n+1/2}}{\Delta z} &= \frac{-\varepsilon_{xx}^{ijk}}{c_\circ} \frac{E_x^{i,j,k-1/2}|_{n+1} - E_x^{i,j,k-1/2}|_n}{\Delta t} \\
&\quad + \sigma_{xx} E_x^{i,j,k-1/2}|_n \\
\frac{H_x^{i,j,k}|_{n+1/2} - H_x^{i,j,k-1}|_{n+1/2}}{\Delta z} &= -\frac{-\varepsilon_{yy}^{ijk}}{c_\circ} \frac{E_y^{i,j,k-1/2}|_{n+1} - E_y^{i,j,k-1/2}|_n}{\Delta t} \\
&\quad + \sigma_{yy} E_y^{i,j,k-1/2}|_n
\end{aligned}$$

Obviously only k is incremented, since it represents the propagation along the z-axis. The fields are also temporally staggered in a way that $\vec{E}$ is computed at a point in time $n\Delta t$, then $\vec{H}$ is computed at $(n+1/2)\Delta t$ instead of $(n+1)\Delta t$, which is where the next value of $\vec{E}$ is computed.

Numerical details

The solution of the equations starts with an initial value of the electric field on a Yee lattice. From the equations above, the temporal variation of $\vec{E}$ depends on the spatial variation of $\vec{H}$, and vice versa. Thus, propagating the initial values of $\vec{E}$ in space and time will update the following values of $\vec{H}$. After that propagating $\vec{H}$ will update $\vec{E}$, and so on. It is essential to choose a proper discretization grid; a grid that is too large will propagate the solutions over small distances and time intervals which negatively impacts the efficiency of the algorithm, whereas a grid that is too small will lead to numerical instabilities [48].

The fields are updated in the above fashion until they reach the boundaries of the Yee lattice. At that point special assumptions have to be made in order to truncate the simulation. That is usually achieved via absorbing boundaries that force all outgoing or reflected fields to decay. From a numerical point of view, an artificial absorbing material is introduced and it is known as perfectly matched layers (PML) [59]. Details of this procedure are discussed in [49]. The introduction of such a hypothetical material has to be done very carefully, in order to ensure that the material really absorbs all outgoing waves, and does not generate any strange numerical artefacts [60].

5. Plasmonic Photonic Crystals

In Sec. 2.2.2 and 3.2 the properties of surface plasmon polaritons (SPPs) were discussed in detail. However, the computational details of the photonic band structure under the influence of plasmonic surface waves were not covered as part of the general discussion. In this chapter we present a perturbative approach to numerically compute the effect of SPP on photonic crystals characteristics, which leads to a systematic correction of the band structure of a reference dielectric photonic crystal.

In the following we will briefly describe the theoretical background of the first-order perturbation method used in this study. The next section contains some numerical results obtained for a two-dimensional honeycomb plasmonic photonic crystal. We will close with a short discussion of our results. The core numerical calculations are performed using the MIT Photonic Bands (MPB) code. which is a frequency–domain solver [32]. The extensions that deal with the perturbation of the bands are developed in the python programming language, see appendix A. The results as well as the discussion in this section were originally published in [3].

5.1 Perturbation theory

In contrast to textbook examples of standard photonic crystals, the variation of the dielectric function at a given frequency is crucial for the description of plasmonic photonic crystals, since the frequency dependency introduces non-linearities, which in turn modify the resulting band structures. Within the framework of perturbation theory, the change in the band structure $\Delta\omega$ is related to the change in the dielectric function $\Delta\varepsilon$, as well as to the electric field $\vec{E}(\vec{r})$ itself, see [30]:

$$\Delta\omega = -\frac{\omega}{2}\frac{\int \mathrm{d}^3 r \Delta\varepsilon |\vec{E}(\vec{r})|^2}{\int \mathrm{d}^3 r\, \varepsilon |\vec{E}(\vec{r})|^2}. \tag{5.1}$$

Here we have neglected the $\vec{k}$ dependence of the band structure $\omega(\vec{k})$ and of the fields $\vec{E}(\vec{k},\vec{r})$. The metallic substrate alters the dielectric function of a photonic crystal, which leads to different

effective dielectric functions $\varepsilon_{\rm spp}$ at both sides of the interface [37]

$$\varepsilon_{\rm spp}(\omega) = \frac{\varepsilon_m(\omega)\varepsilon_d(\vec{r})}{\varepsilon_m(\omega) + \varepsilon_d(\vec{r})} \ . \tag{5.2}$$

Here $\varepsilon_d(\vec{r})$ is the composite dielectric function of the materials forming the photonic crystal (silicon and air for example), and $\varepsilon_m(\omega)$ is the metallic dielectric function, which can be modelled using a standard formula such as the Drude model as shown in chapter 2:

$$\varepsilon_m = 1 - \frac{\omega_p^2}{\omega^2 - i\omega\gamma} \ . \tag{5.3}$$

Remember that ω_p is the plasma frequency of the metal and γ is a damping constant. It is also worth mentioning that for simulations of the plasmonic photonic band structures, only the real part of $\varepsilon_{\rm spp}$ will be of interest. The presence of the complex part does not influence the features of the band structure, it only leads to a gradual decay of the surface waves [61].

We now have a very interesting theoretical, numerical and experimental setting. We can also systematically introduce disorder into the photonic crystal component, which leads to the localization of photonic Bloch states. On top of that the imaginary part of $\varepsilon_{\rm spp}$ leads to an evanescent character of the Bloch-like states in a plasmonic photonic crystal anyway. A detailed study of such models is likely to tell us something fundamental about the character of optical localization [46], and how we can actually manipulate it in practice.

To compute the correction in the harmonic mode numerically we use first order (self-consistent) perturbation theory. In other words, we first compute the band structure using a suitable dielectric constant for the regular photonic crystal. Then, within a small window of frequencies, ω to $\omega + \Delta\omega$, we compute the change in the frequency using a standard frequency domain code [32]. We thus assume that within the small frequency window chosen, the effective dielectric function will not fluctuate very wildely, and therefore the resulting band structures are approximately self-consistent.

For this to work, we have to ensure that for a given range of frequencies, the relative change in the dielectric constant $(\Delta\varepsilon/\varepsilon)$ is less than 1%, such that Eq. 5.1 will give the main perturbative corrections. Under such conditions a first order perturbation theory is sufficient. However, larger fluctuations in the dielectric function might require higher order perturbation theories, or even iterative schemes.

5.2 The Plasmonic Band Structure

We compute the photonic band structure for a two-dimensional honeycomb lattice consisting of cylinders of radius r = 0.2α, where α is the lattice constant, see Figs. 5.1a and 5.1b. The cylindrical rods are made of silicon with dielectric constant of 13, and they are embedded in vacuum. Such high dielectric contrast increases the chances of forming a photonic band gap

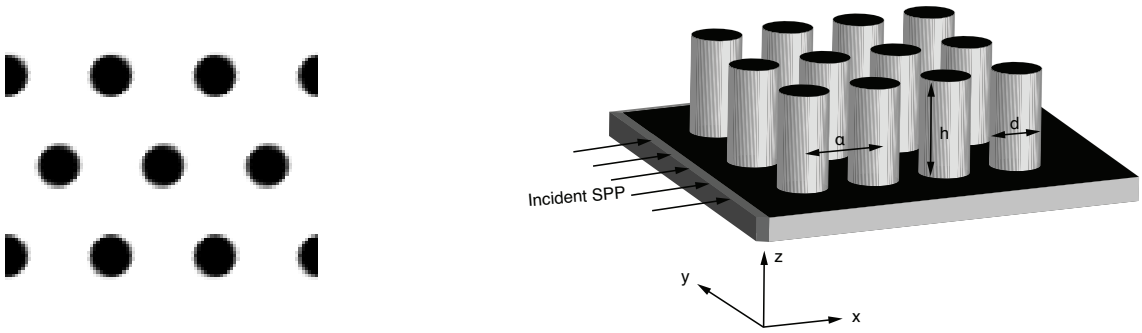

(a) (b)

Figure 5.1: (a) A schematic diagram for a 2D honeycomb photonic crystal, and the corresponding schematic 3D plasmonic photonic crystal in (b).

In Fig. 5.2a we show the TM mode photonic band structure in units of $\frac{2\pi c}{\alpha}$, where c denotes the speed of light. The density of photonic states is shown in Fig. 5.2b. This photonic crystal has a photonic band gap of width 0.14 $\frac{2\pi c}{\alpha}$ appearing between frequencies 0.28 $\frac{2\pi c}{\alpha}$ and 0.42 $\frac{2\pi c}{\alpha}$. A smaller band gap of width 0.02 $\frac{2\pi c}{\alpha}$ is observed at higher bands.

To study the effect of the plasmons on the band structure, we used a Drude model for aluminium with a plasma frequency $\omega_p = 2.24\times10^{16}$ rad/sec and a damping constant γ of 1.22×10^{14} rad/sec [24]. To evaluate the effective frequency–dependant dielectric function, we increment the range of frequencies presented in the original band structure (Fig. 5.2a). Then, we iterate over all increments and determine the effective dielectric function for each frequency in the band structure that falls within the particular increment using Eq. 5.2. It is important to mention that prior to the calculation of the effective dielectric function, the units of the frequencies have to be converted to rad/sec, which involve the lattice constant. Thus, the resulting solutions of Maxwell's equations are no longer scale-invariant, and the band structure will depend on the

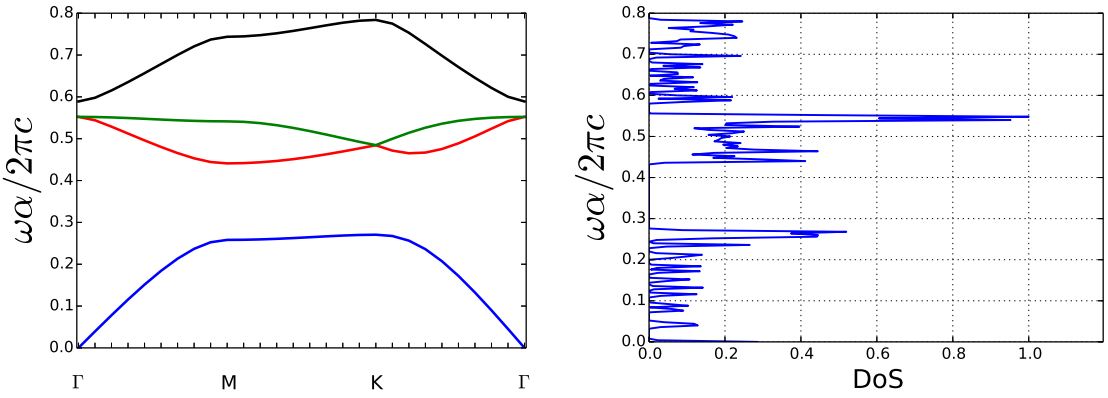

(a) (b)

Figure 5.2: (a) TM modes in units of $\frac{2\pi c}{\alpha}$ for a honeycomb photonic crystal The. In (b) we show the corresponding scaled density of states (DoS).

dimensions of a given plasmonic system. In other words, scale invariance requires frequency–independent dielectric constants, which may be justified for a typical photonic crystal, but not for plasmonic photonic crystals any more.

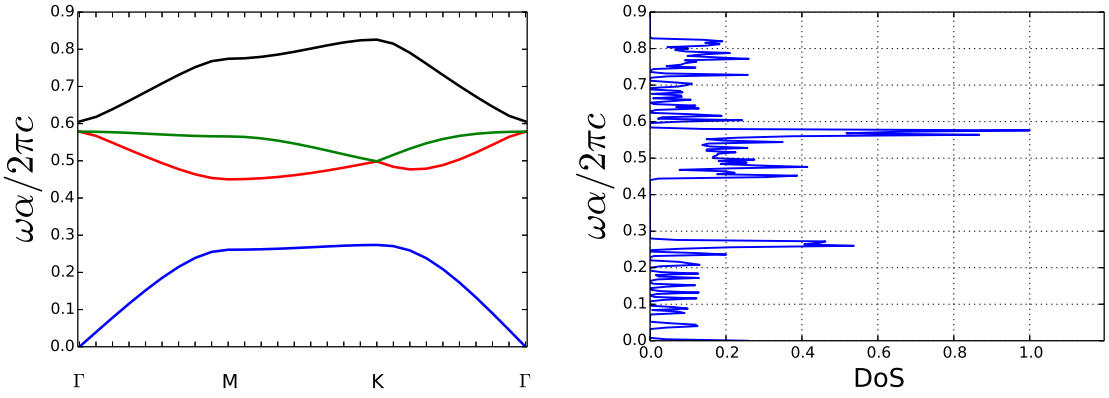

(a) (b)

Figure 5.3: (a) The plasmonic band structure computed using perturbation theory. The metallic surface consists of aluminium with $\omega_p = 2.24\times10^{16}$ rad/sec and $\gamma = 1.22\times10^{14}$ rad/sec. The lattice constant α is taken to be 500 nm. The frequencies are again represented in units of $\frac{2\pi c}{\alpha}$. In (b) we show the corresponding scaled density of states (DoS).

In Fig. 5.3a the band structure for a honeycomb photonic crystal placed on an aluminium

substrate is shown for lattice constant $\alpha = 500$ nm. For lower bands the effect of the plasmons is not evident, due to the small change in the dielectric function at low frequencies. Moreover, the lowest band appears to be almost flat along M-K vectors, which is an indication of localized states. The higher bands, however, have shifted their positions and a wider band gap is reported. For instance, the band gap between the first and the second band has increased to 0.17 $\frac{2\pi c}{\alpha}$, which corresponds to an increase of approximately 13% . However, the bands at higher frequencies do not change in width.

5.3 Summary

We have developed a numerical tool based on first-order perturbation theory to study the photonic band structure of surface plasmon polaritons at the interface between a honeycomb photonic crystal and a metallic substrate. The metallic dielectric function is modelled using a Drude function, and only the real part of the resulting effective dielectric function for the plasmonic surface waves is used to compute the corresponding plasmonic photonic band structure.

According to our treatment, the surface plasmon waves break the scale invariance of Maxwell's equations. That could be of great interest, since one geometry with different lattice sizes can now control the flow of light quite differently. Moreover we noticed an increase in the size of the band gap at low frequencies. However, the Drude approach might be largely misleading in this aspect, since the overall change in the dielectric function at such frequencies can be quite remarkable, and the change in the band structure will be much larger. A treatment using tabulated metallic dielectric data as a function of frequency might be a better a approach, together with tabulated data of the dielectric components of the photonic crystals. Such data can be taken from experiment, or obtained from numerical studies using ab initio methods based on density functional theory [62].

6. Critical States In Photonic Quasicrystals

Quasiperiodic crystals (quasicrystals) are structures that demonstrate certain geometrical patterns but have no translational symmetry. The construction of quasicrystals involves non-trivial mathematical modelling, for example methods such as cut and project are used to build quasiperiodic structures, where a higher dimensional periodic lattice is sliced irrationally using a set hyperplanes and projected into a lower dimensional space under certain restrictions [63]. Such restrictions result quasiperiodic structures. In this work, the two–stage–projection method is employed to generate quasiperiodic lattices [64]. The two–stage–projection method is a special case of the cut and project scheme, but with the distinct advantage that only one-dimensional acceptance domains (i.e. intervals) are necessary in the first step, whereas the second projection step is usually trivial (i.e. choosing a layer), see Sec. 6.1.

The unique properties of photonic quasicrystals such as a complete band gap at low index contrast [65, 66] are attributed to high structural symmetries [67]. The richness comes with the complexity of the mathematical modelling of quasicrystalline structures, in particular their relations to higher dimensional lattices. Quasicrystals are generated systematically using different mathematical techniques, with the cut and project technique being the most prominent one [63]. Although it is hard to find all of the resulting quasiperiodic structures in nature in the form of intermetallic alloys, a large number of quasicrystalline structures may easily be realized as photonic quasicrystals. Therefore the cut and project scheme allows us to construct whole families of easy-to-generate, but sufficiently complex, quasiperiodic lattices to systematically study photonic band gaps and optical localization.

In this chapter we present the model and the findings published in [2]. We investigate the optical properties of two-dimensional (2D) photonic quasicrystals. Our aim is to quantify the localization of the photons in the novel 2D dodecagonal lattice, using the standard time domain methods to evaluate the transmission coefficients. Optical localization itself is determined using the analytical concept of an inverse participation ratio (IPR), which quantifies the number of states over which

photons are distributed at a given frequency [46].

In the following sections we discuss the details of generating the quasicrystalline structure used in the simulation. The method is described in Secs. 6.1 and 6.2. That is followed by the transmission spectrum analysis, and the discussion of optical localization in such systems.

6.1 Two–stage–projection

For the cut and project scheme we consider a periodic structure in a higher dimensional space R^D, where D represents the dimensions of the space. If we try to project all of the lattice points into a lower d-dimensional subspace $\mathrm{R}^d_\parallel$ known as parallel or physical space, we will simply end up with a periodic or a dense set of lattice points, both of which will be of little use. In order to produce a discrete and aperiodic set of points in $\mathrm{R}^d_\parallel$, we introduce an intermediate subspace known as the perpendicular space $\mathrm{R}^c_\perp$ with dimensionality equal to c where $\mathrm{R}^D = \mathrm{R}^d_\parallel \times \mathrm{R}^c_\perp$. We then define an acceptance domain Γ in $\mathrm{R}^c_\perp$, which is simply the projection of a unit cell of R^D onto $\mathrm{R}^c_\perp$. Next we project the points of the R^D lattice whose projection onto $\mathrm{R}^c_\perp$ falls into the acceptance domain Γ [63].

The so–called two-stage projection method employs cut and project techniques to map higher-dimensional lattices onto lower-dimensional laminar (i.e. layered) structures, using only one-dimensional acceptance domains [64]. This has a clear numerical advantage over other schemes, which have to fallback on quite complicated and even fractal acceptance domains [63].

In principle the two stage projection method consists of two cut and project steps. The tricky step is the former, which will project a higher-dimensional lattice in R^D onto a lattice in $\mathrm{R}^{D-1}_\parallel$, using a 1D acceptance domain in $\mathrm{R}^1_\perp$. Assuming that $\mathrm{R}^{D-1}_\parallel = \mathrm{R}^\delta \times \mathrm{R}^\gamma$, we can apply the cut and project scheme a second time in order to generate the final aperiodic structure in R^δ, where the structure usually represents a stack of quasiperiodic planes, which can be projected further. Examples are given in [64].

In the following section we map a lattice from 4-dimensional space onto a laminar structure in 3-dimensional space. Each layer contains 2-dimensional quasiperiodic structures, and the second application of the cut and project scheme is rather trivial, as discussed above. We then extract

the quasiperiodic structures from all the layers that are periodically spanned along the z-axis. Finally we collapse the layers onto a 2-dimensional x-y plane, which forms the basis of patches used for our simulations.

6.2 Finite Difference Time Domain Method

A finite–difference–time–domain solver (FDTD) [20] is used to characterize the localized optical modes in a 2D quasicrystal. The samples are patches from QC's, as discusses above. The smaller the window, the fewer the points mapped, and hence a smaller QC lattice is produced. The patches generated have a length l and a width w. All dimensions are given in terms of a characteristic length scale α.

However, to run the simulation and achieve stable results, we introduce a simulation cell that has dimensions greater than those of the generated quasicrystal, so that it fits the QC as well as the perfectly matched layers (PML). The QC was then placed at the center of the simulation cell. The gap between the edges of the crystal and the borders of the simulation cell is filled with PML. We ensured that the thickness of the PML is sufficient for the electromagnetic modes to decay and that no backward reflection is encountered during our simulations.

A Gaussian source is positioned at the center of the simulation cell. The source center frequency is 0.5, and it has width of 0.55 both in units of $2\pi c/\alpha$ where c is the speed of light. The outgoing flux is measured in a direction perpendicular to the y-axis at a surface of length l. The flux quantifies the amount of energy transmitted through the surface of the structure, and it is given by:

$$P(\omega) = \hat{\mathbf{n}} \cdot \oint \vec{E}(\omega) \times \vec{H}(\omega)\ \mathbf{d}\mathrm{A} \tag{6.1}$$

where the surface integral is the Poynting vector, and $\hat{\mathbf{n}}$ is the surface normal. Given the flux computed by Eq.6.1, the transmission coefficients can be obtained as the ratio between the outgoing flux in the presence of the QC and the flux measured in its absence.

6.3 Dodecagonal Quasicrystal

In order to generate a dodecagonal quasiperiodic structure in 2D using the two–stage–projection method, we begin with a higher dimensional face-centred lattice D_4 [64]. This lattice has much higher symmetries than lattices in three-dimensions and two–dimensions (i.e. up to 12 fold symmetry) [68, 69], which makes it a potential candidate for forming photonic structures with particular optical properties, such as a complete band gap for relatively low index contrast.

The two-stage projection for the dodecagonal 2D quasiperiodic structure is based on the following orthonormal vectors [64]

$$\vec{e}_1 = \left[\frac{a}{2}, \frac{a}{2}, 0, \frac{b}{\sqrt{2}}\right] \qquad \vec{e}_2 = \left[\frac{a}{2}, -\frac{a}{2}, \frac{b}{\sqrt{2}}, 0\right]$$
$$\vec{e}_3 = \left[\frac{b}{\sqrt{2}}, 0, -\frac{a}{2}, -\frac{a}{2}\right] \qquad \vec{e}_4 = \left[0, \frac{b}{\sqrt{2}}, \frac{a}{2}, -\frac{a}{2}\right]$$

where $a^2 = 1 + \frac{1}{\sqrt{3}}$, $b^2 = 1 - \frac{1}{\sqrt{3}}$. The vectors $\vec{e}_1$, $\vec{e}_2$ and $\vec{e}_3$ represent the basis for the parallel space $R^3_{\parallel}$ and $\vec{e}_4$ is the base of $R^1_{\perp}$. We project the lattice onto parallel space using an acceptance domain in the half open interval $\left(-\left(\frac{a}{2} + \frac{b}{\sqrt{2}}\right), +\left(\frac{a}{2} + \frac{b}{\sqrt{2}}\right)\right]$. The projected set of points is then represented in these transformed coordinates, and it forms a laminar 3D structure, where each layer contains a quasiperiodic dodecagonal structure, as described in [64].

Each point in the cell is then taken to represents the center of a cylindrical object with radius r = 0.2α and dielectric constant $\varepsilon = 12.4$, corresponding to the dielectric constant of silicon. These cylindrical objects are surrounded by air which has a dielectric constant of 1. The height of the cylinders is set to 0.8α. The FDTD simulation is run until the field decays close to the borders of the cell and the values of the field at each point in the QC is stored for every 0.05 time unit.

In Fig. 6.1 the transmission coefficients reaches a minimum value of zero in the relative frequency range 0.59 – 0.649, which indicates that the propagation of states within that frequency range is forbidden, and a band gap has opened. The formation of such states is be attributed to Bragg scattering [70], where the interference of extended states at the band gap can also lead to the formation of new states in the range [46]. However the states at the mobility edges (close to the band gap) are likely to be localized.

To further understand the nature of the band edge states, we gradually increase the size of the

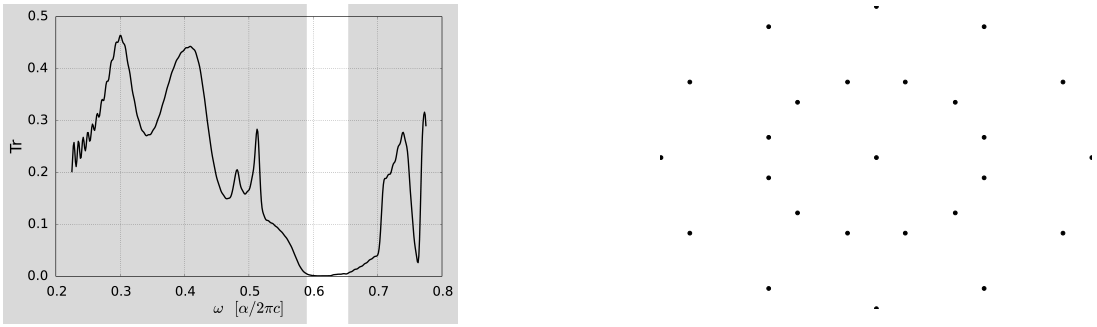

(a) (b)

Figure 6.1: In (a) we plot the transmission coefficients as a function of the frequency for the crystal shown in (b). The frequencies are given in units of $2\pi c/\alpha$ and the lattice has dimensions of 1.5 $\times$ 1.

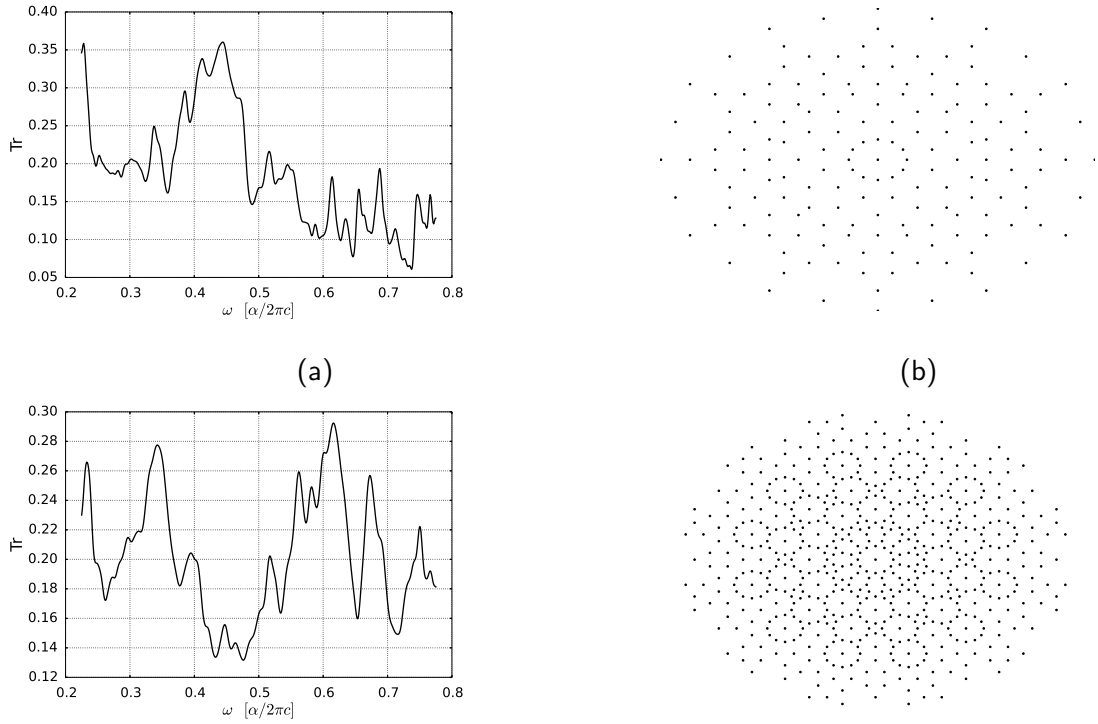

(a) (b)

(c) (d)

Figure 6.2: In (a) and (c) we plot the transmission coefficients that corresponds to crystals shown in (b) and (d) respectively. The crystal (b) has dimensions of 6 $\times$ 4 and (d) is 8.58 $\times$ 5.72.

window used in mapping the quasiperiodic structure points. In Fig. 6.2 the transmission coefficients exhibit the formation of new states at the band gap due to the constructive interference

between the neighbouring states formed by the presence of new scatterers. In contrast to a 1D case where the transmission decays exponentially as a function of the crystal size [46], the results presented in Fig. 6.2a and 6.2d show an enhancement in the transport around the band gap frequency. In a 2D world, the scaling theory is a bit more complex, and such changes in the transmission could belong to either localized or critical states. We hence plot the field profiles for different cell sizes as a function of the frequency. To this end, we accumulate the Fourier transformations of the fields at each point in space, and plot a contour of the field profiles in the lattice.

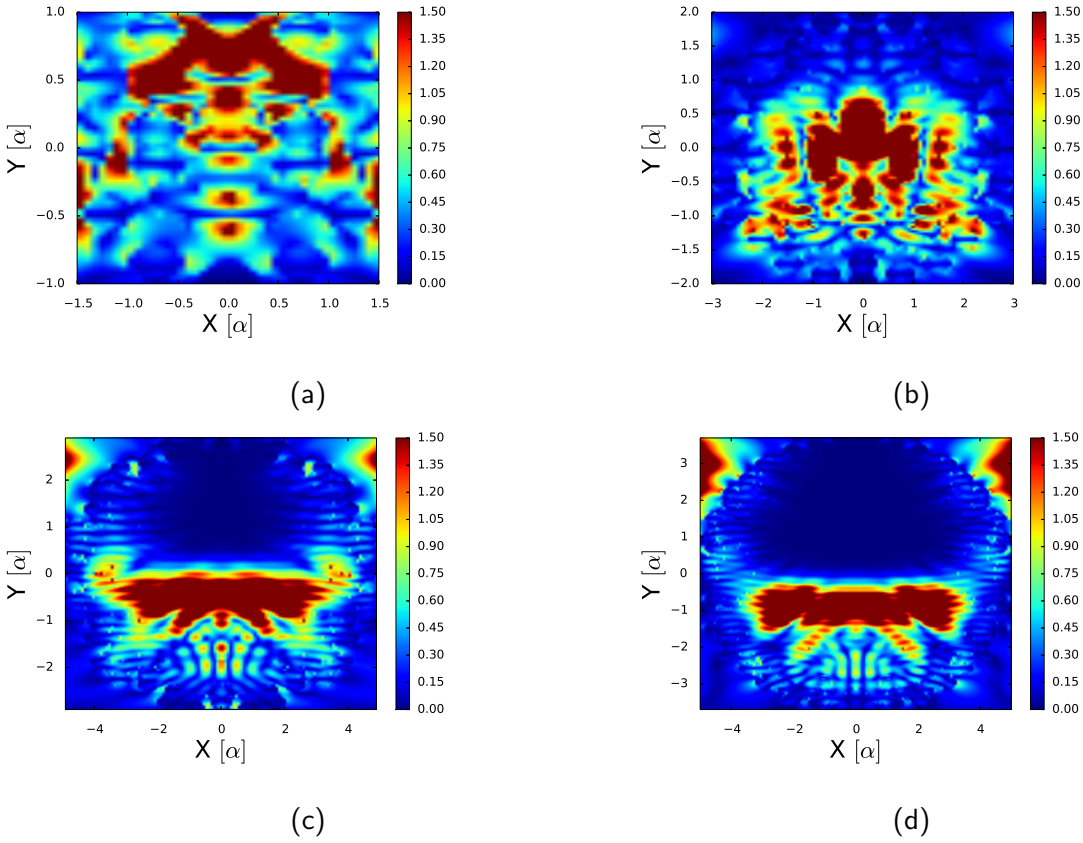

Figure 6.3: The contour represents the field profiles for a Gaussian source at the center of QC patches with dimensions (a) 3 × 2, (b) 6 × 4 (c) 8.58 × 5.72 and (d) 10.1 × 6.74. in units of α^2. Only modes with frequencies near the band gap are presented. The colour-map shows the intensity distribution in the crystal.

For a crystal with dimension 3 × 2 [α^2] the fields tend to spread across the lattice and position themselves around regions with high dielectric as shown in Fig. 6.3a. As the QC size increases,

Figs. 6.3b – 6.3d, we observe strong attenuation of the fields in regions that previously had high intensity which is due to the scattering from the extra lattice points. However, for the larger cells presented in Figs. 6.3c and 6.3d, the profile patterns do not vary remarkably and the modes are trapped at the vicinity of the Gaussian source. Some of these patterns are a visual indication that there are localized states forming in parts of the structure. Having in mind the enhancement in light propagation near band gap as seen in Figs. 6.2a and 6.2c, we further identify these modes as resonant modes.

Finally we perform the inverse participation ratio IPR analysis to identify localized states. The inverse participation ratio is given by

$$\mathrm{IPR}(\omega) = \frac{\sum_{\vec{r}} |\Psi(\omega, \vec{r})|^4}{\left[\sum_{\vec{r}} |\Psi(\omega, \vec{r})|^2\right]^2} \tag{6.2}$$

where the sum runs over all the points in real space. The localized states are identified by an IPR that is proportional to $\exp(-2\zeta L)$ where L is the size of the sample in the direction of the modes propagation. In other words, a localized state shows an exponentially decaying inverse participation ratio with increasing the system size. As the system size approaches the infinity, the IPR for localized states becomes constant.

In Fig. 6.4 we present the inverse participation ratio of the modes near the mobility edges as a function of the lattice size L. We use a least-squares fitting to determine the localization length ζ from the IPR around the band gap edges. We estimate that the localization length for the QC to be $\sim 0.3207[\alpha^{-1}]$.

6.4 Summary

We have investigated the localization of electromagnetic modes in a 2D quasiperiodic photonic crystal. The sample structure was generated using a two stage projection scheme leading to a laminar three-dimensional QC, where we map all layers into a single dodecagonal QC. The number of points mapped from a higher dimension space was systematically increased leading to larger and larger patches. The lattice points were taken as centres of cylindrical objects of radius 0.2

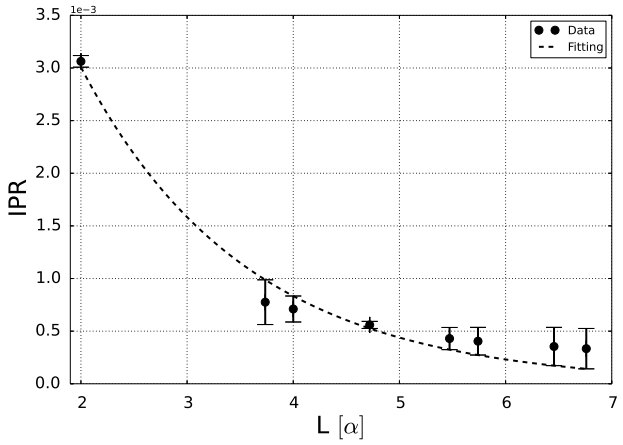

Figure 6.4: The decay of the inverse participation ratio as a function of the lattice size. The IPR values were extracted at frequencies between 0.59 – 0.649 (in units of $2\pi c/\alpha$) and averaged out. The error bars shown in the figure represent the deviation between each data point and the value obtained from the fitting.

α where α is a characteristic lattice length. These cylinders have a dielectric constant of 12.4, whereas the surrounding media has a dielectric constant of 1.

Performing finite–differences-time-domain simulations, we observed a photonic band gap at frequencies 0.59 – 0.649 (in units of $2\pi c/\alpha$). Increasing the size of the QC patches, we observed the formation of new states at the band gap. Such states are a result of a constructive interference of states at the band gap.

Plotting the field profiles showed that field intensities are diminishing at intermediate frequencies as the size of the crystal increased, and hence the number of the scatterers. The inverse participation ratio showed that some states near the mobility edges are localized. The localization length is estimated from the scaling theory to be around $0.3207[\alpha^{-1}]$. An interesting open problem remains the appearance of critical states in 2D and 3D disordered structures [46]. It can be answered by carrying out more systematic studies, where the analytical tools presented in this study should be of great use.

7. Optical Localization In Photonic Crystals

Localization as presented in Sec. 3.3 was initially proposed as a phenomenon that is associated with electronic waves. Later on, it turned out to be a wave characteristic that extends to all forms of waves. In the field of optics, however, the concept of solitons localization in waveguide arrays was proposed in the year 1988 [71]. The system is formed of a structure that is uniform in one direction and has defects (disorder) in the transverse direction and that is why it is also known as transverse localization. Such structures are perfect for the formation of discrete soliton which can hence be modelled under certain approximation using a Schrdinger-like equation.

Experimentally, the observation of transverse localization was not easy, for various reason including the fact that the theoretical aspects of localization in the physics solitons were not well understood. It was only in the year 2007 that transverse localization was seen in experiments [72, 73]. On the other hand, the study of localization in paraxial disordered photonic systems faced some difficulties due to other factors. For example obtaining sensible results that assures the existence of localized modes require the averaging over multiple defect configurations [74]. Moreover different analytical approaches can be followed to determine weather or not an optical mode is localized.

One of the approaches that can be used to analyse localized modes is the study of the behaviour of the transmission spectrum, which predicts that for localized modes the transmission function tends to decay exponentially as the size of the sample increases. Moreover, the mode intensity over a distance L also reflects their localized nature [46]. Localized photons have high densities over a short distance, while extended ones are spread over longer distances [30]. Finally the scaling of the inverse participation ratio for localized states also decays exponentially as the sample size increase [75].

In this chapter we will explore two different examples of photonic structures with the aim of covering the different approaches to understand localization. In the first example we present a periodic photonic crystal with multiple defects (disordered photonic crystal). We focus on the

analysis of the mode intensities related to defect sites in order to show the localization effect. In the second example we demonstrate the localization effect in two-dimensional quasicrystals using the technique developed in chapter 6.

7.1 Localization in Photonic Crystals

The experimental observation of localization in photonic crystals was always related to disorder, where the backscattering effect in highly disordered dielectric media will always lead to localization. In this section we start off with a simple 2D triangular lattice with defects located at a well–defined lattice sites. As presented previously in Sec. 5.2, this crystal has a photonic band gap (TM bands) between $\omega \sim 0.28$ and $\omega \sim 0.42$ in units of c/α where c is the speed of light and α is the lattice constant.

To introduce a single defect in the crystal with radius 0.2 α, one has to increase the size of the unit cell used for the computations. Initially the structure is a simple triangular lattice spanned by the unit vectors $\vec{a}_1 = \sqrt{0.75}\alpha\hat{x} + 0.5\alpha\hat{y}$ and $\vec{a}_2 = \sqrt{0.75}\alpha\hat{x} - 0.5\alpha\hat{y}$. Adding the defect requires the lattice to be bigger, which makes a supercell approach more suitable. Thus, we replicate the cell five times along both directions $\vec{a}_1$ and $\vec{a}_2$ to generate a supercell. Then a single lattice point at the origin (0, 0, 0) is removed which breaks the symmetry of the lattice and form a defect, see Fig. 7.1a.

Instead of performing a full band structure calculation on the crystal, we rather focus on the modes formed at the defect site, which hence makes the simulation independent of the reciprocal lattice vectors. It was found that new bands appear at frequencies $\omega \sim 0.391397\ c/\alpha$ which was previously a forbidden frequency (band gap). In Fig. 7.1b we show the modes formed at the defect site. To understand the nature of the newly formed band we calculate the energy intensity within the vicinity of the defect. It was found that approximately 62.05% of the bands are localized in the surroundings of the defect.

To further understand the physics of the defects, we introduce three more defects at randomly selected sites on a much larger cell (10 $\times$ 10). The field profiles shown in Fig. 7.2 represent two different geometries with five defects (Fig. 7.2a) and six in Fig. 7.2b. To analyse the newly

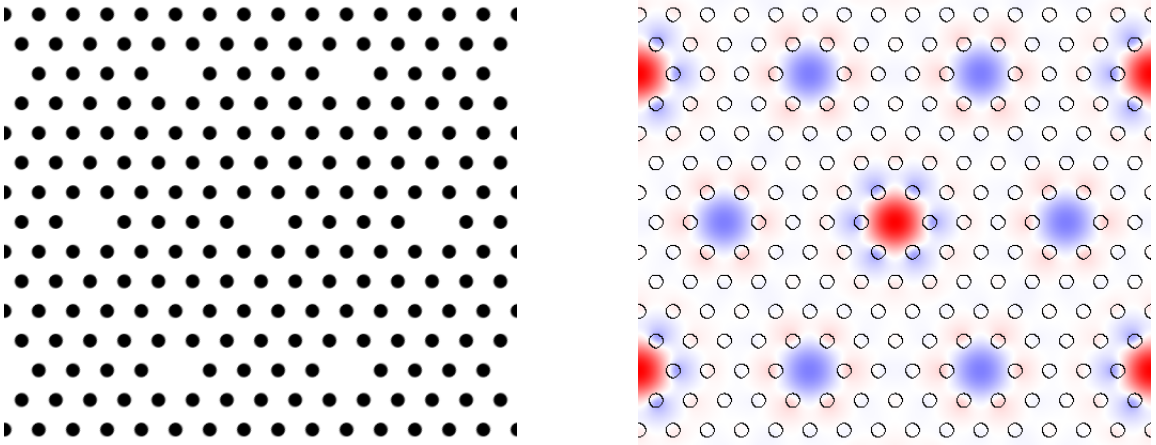

(a) (b)

Figure 7.1: (a) A 2D triangular photonic crystal with a single defect at the center of its unit cell and (b) is the localized field intensity around the defect.

formed bands we study ten different realizations of each lattice. It was found that the new states occur at $\omega \sim 0.3584\, c/\alpha$. For the geometry presented in Fig. 7.2a, 71.4 % of the fields intensity is localized in the vicinity of a single defect.

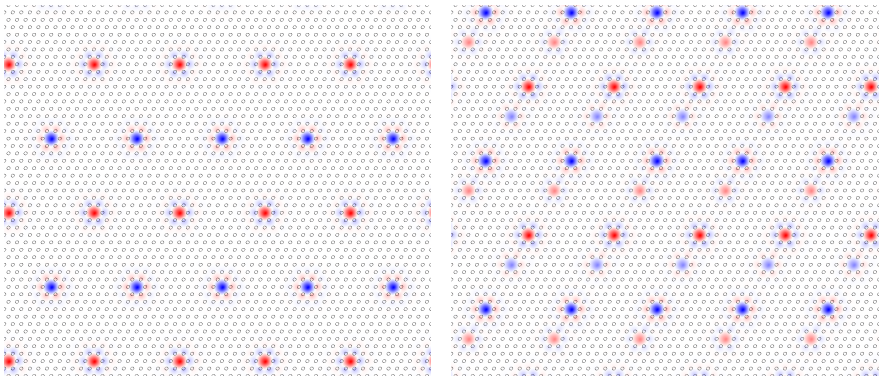

(a) (b)

Figure 7.2: In (a) the field intensity of the localized modes is shown around the defects for a photonic crystal with five defects in the unit cell, where (b) represents a crystal with six defects in the unit cell. Only a limited size is shown in each figure.

As the number of defects increase, the behaviour of the optical modes change, which justifies why the average has to be considered. For instance, adding one more defect does not change much rather than a slight fluctuation in the intensity of the fields at the defect sites. However,

adding additional defects may impact that percentage noticeably, and it changes the distribution of the optical modes. For the structure shown in Fig. 7.2b 49.8 % of the modes are localized around one defect while 21.5 % are found in the surroundings of another defect. In a different geometry that contained the same number of defects but distributed differently, the percentages of the field intensities at two defect sites varied from 58.6 % to 12.6 %.

7.2 Localization in Photonic Quasicrystals

In the field of photonics the search for novel types of band gap materials has been a major motivation for scientists to explore a large variety of different structures. Periodic structures, for instance, have interesting properties and a wide range of applications (see [76] and [77] for review). However, only a limited number of basic photonic geometries has allowed for the formation of photonic band gaps. This has culminated in the growing interest in aperiodic structures, as a result of a wide variety of different candidate geometries for photonic band gap materials, and hence a much richer physics. Of particular interest are quasicrystals (QCs), which are well organized structures that lack translational symmetry at a short range [63]. But they obviously display some aperiodic long range order, as suggested by their sharp and unusual diffraction patterns [78].

Photonic quasicrystals (PQCs) have been shown to give rise to photonic band gaps formed via Bragg scattering [70]. In 1D, band gaps have been found in Fibonacci-like QCs [79, 80], and the higher dimensional octagonal quasicrystals were also shown to form a band gap [66]. Interestingly, a band gap for a very low refractive index contrast has been reported for dodecagonal QCs [65]. Moreover, related effects such as field enhancement and slow modes at the band edge were observed in various experimental studies [81]. In addition to that, photonic modes were found to be localized in ten-fold Penrose tiling. In such structures localized modes were associated with the tunnelling phenomena and the presence of fast light [82]. Experimentally, the localized states were observed in Fibonacci sequences where the transmission scales and the light propagation is enhanced due to resonant localized states [83, 2].

In this section we follow the scheme developed previously in chapter 6 to generate a quasiperiodic

structure from a four–dimensional (4D) square lattice, and investigate its optical characteristics. In contrast to the results presented in the Sec. 6.3, we show that states formed in the quasiperiodic layer are localized.

7.3 Octagonal Quasicrystal

The structure used to study the optical localization is a quasiperiodic lattice generated using the technique described in Sec. 6.1. Initially we start with a 4D square lattice [64] with a set of unit vectors

$$\vec{e}_1 = [2,0,0,0] \qquad \vec{e}_2 = [0,2,0,0]$$
$$\vec{e}_3 = [0,0,2,0] \qquad \vec{e}_4 = [0,0,0,2]$$

The lattice is spanned over the 4D space using the unit vectors as basis. The resulting set of vectors is then projected onto the following orthogonal vectors:

$$\vec{p}_1 = [1,0,0,0] \qquad \vec{p}_2 = \left[0,0,\frac{1}{\sqrt{2}},\frac{1}{\sqrt{2}}\right]$$
$$\vec{p}_3 = \left[0,\frac{1}{\sqrt{2}},\frac{1}{2},-\frac{1}{2}\right] \qquad \vec{p}_4 = \left[0,-\frac{1}{\sqrt{2}},\frac{1}{2},-\frac{1}{2}\right]$$

which generates a set of dense points. However, only those points whose projection onto the perpendicular space fall into the 1D acceptance domain $\left[-1-(3\times\sqrt{2}/2), 1-(\sqrt{2}/2)\right]$, are projected. The resulting crystal is a 3D quasicrystal periodic in one direction. In contrast to the crystal modelled in chapter 6, a single layer of the three–dimensional structure is considered. In Fig. 7.3b we show the smallest generated crystal that represented the basis of the FDTD simulation.

Similar to the simulation of the dodecagonal lattice in Sec. 6.3, the lattice points generated here also represent the center of cylindrical objects with dielectric function 12.6, radius of 0.25 α and height of 0.8 α where α is a lattice constant. The default dielectric constant (background) is taken to be 1.

The transmission spectrum obtained for the geometry in Fig. 7.3b is presented in Fig. 7.3a does not demonstrate any band gaps, however, a small resonance peak appears at $\omega \sim 0.42\ c/\alpha$.

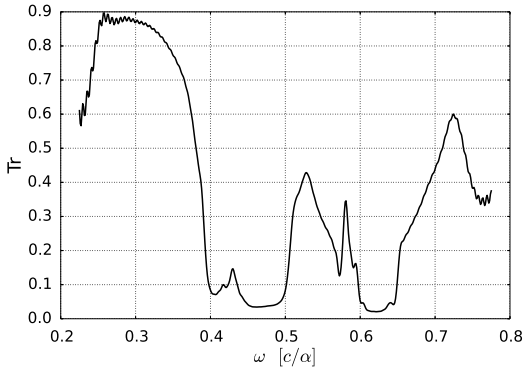

(a)

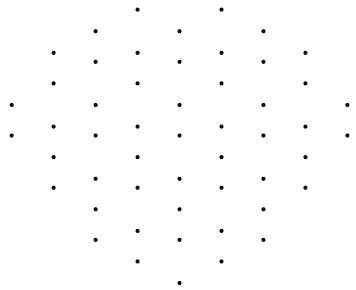

(b)

Figure 7.3: (a) The transmission coefficients for a photonic quasicrystal with the geometry depicted in (b). The crystal is of dimensions 17×13.1 in the units of the lattice constant α and it represents a single layer in a 3D octagonal quasicrystal.

To analyse the behaviour of the transmission coefficients we further increase the number of the mapped points in the quasicrystal lattice, and hence the size of the crystal.

In Fig. 7.4 we show the transmission coefficients as well as the corresponding field profiles for three different crystal sizes; 25.5×19.5, 34×25.3 and 42.4×31.4 where all values are given in terms of the lattice constant α.

The spectrum observed in Fig. 7.4a shows that the transmission coefficients in the frequency window $\omega = 0.42 - 0.5\ c/\alpha$ are decreasing as the size of the lattice increases. The depletion of the transmission function highlights the possibility for the formation of a band gap. In Fig. 7.4c a clear evidence that a band gap is forming in the same frequency range. Moreover, the continuous decrease in the transmission coefficients as a function of the lattice size suggests the presence of localized modes.

The evolution of the field profiles as a function of the lattice size is presented in Figs. 7.4b – 7.4f. In Fig. 7.4d evidences for the formation of localized modes appear as the fields tend to concentrate themselves around the edges of the structure in a low dielectric region. The field profiles shows a prominent increase in the intensity around the edges as depicted in Fig. 7.4f which serves as a clear indication of the nature of the modes.

In Fig. 7.5 the inverse participation ratio near the band gap is plotted against the crystal size L.

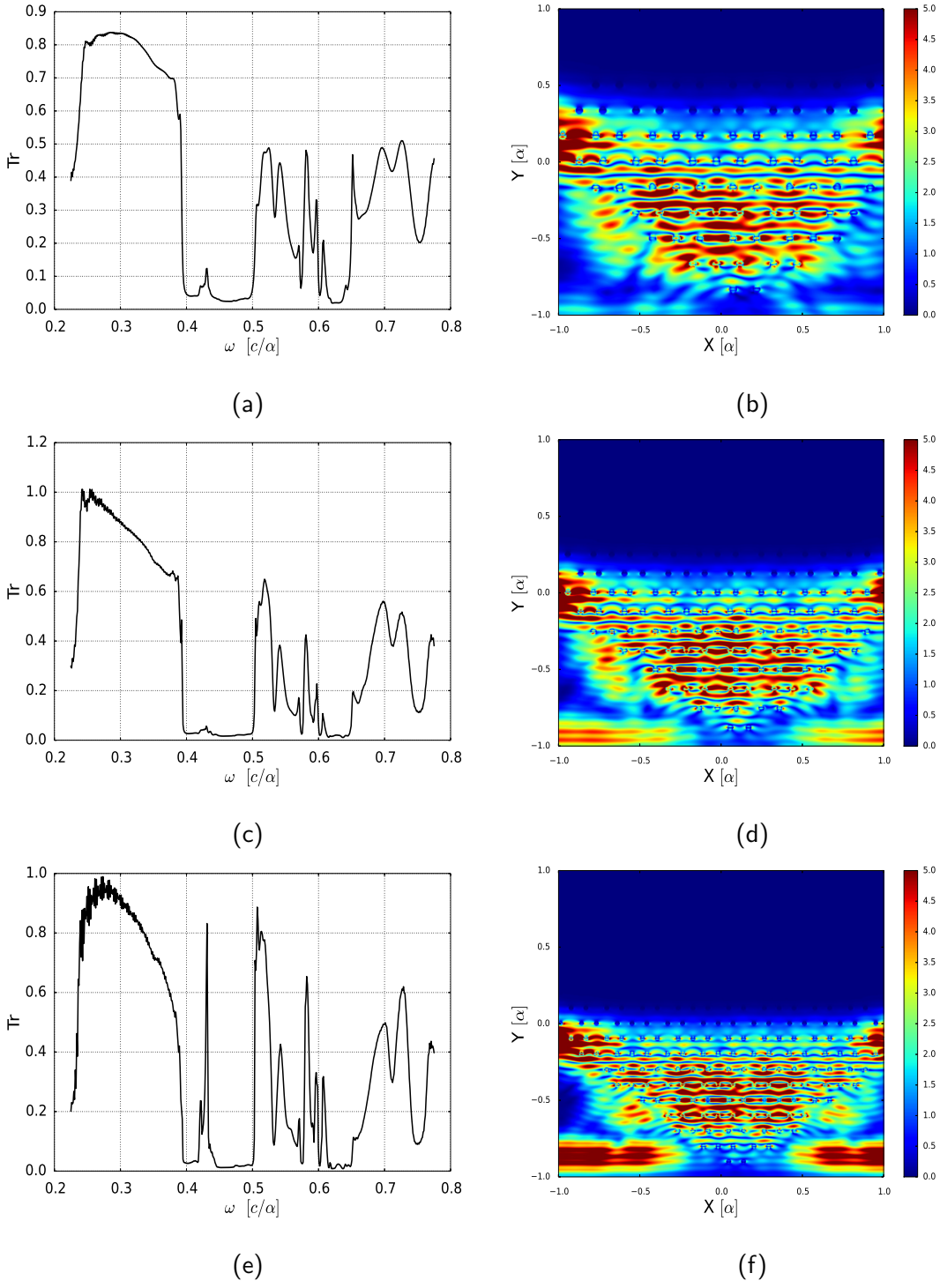

Figure 7.4: The transmission coefficients and the corresponding field profiles for crystals with dimensions (a, b) 25.5×19.5, (c, d) 34×25.3 and (e, f) 42.4×31.4 in units of α.

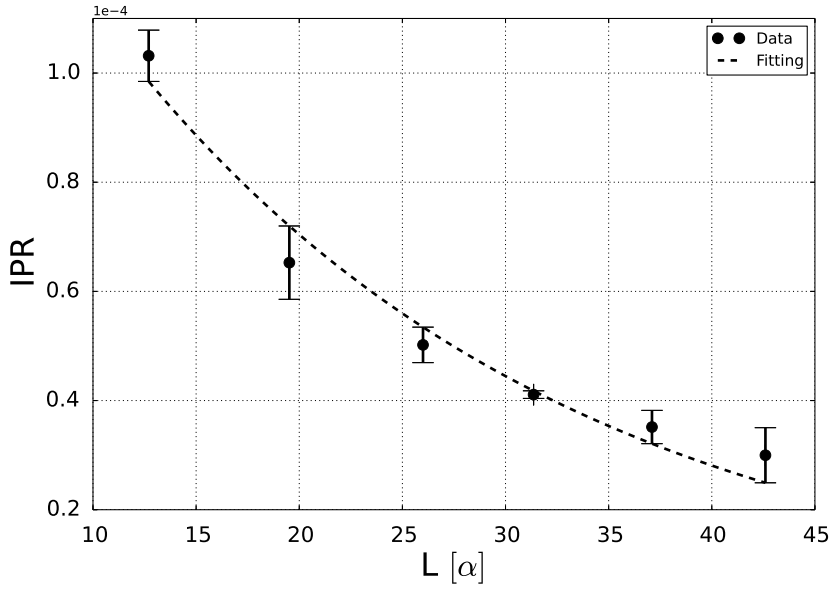

Figure 7.5: The decay of the inverse participation ratio as a function of the lattice size. The IPR values were extracted at frequencies between 0.44 – 0.50 (in units of $2\pi c/\alpha$) and averaged out. The error bars shown in the figure represent the deviation between the data points and the fitting.

In contrast to the IPR presented in Fig. 6.4, we notice that the exponential decay is slower, which is attributed to the higher density of scatterers in the lattice. In turn, that leads to a smaller localization length ζ. For the lattice modelled here the value obtained for the localization length is approximately 0.023 $[\alpha^{-1}]$, which is an order of magnitude smaller than that computed in Sec. 6.3.

7.4 Summary

In this chapter we explored different approaches to qualitatively understand light localization phenomenon. In the first part of the chapter we studied the localization of optical modes around defects in a two–dimensional triangular photonic crystal. The defects were gradually introduced to the structure. In all geometries new states usually form in the band gap and those states tend to be concentrated around the defects. As the number of defects as well as the size crystal

increase, a single configuration may not reflect the true nature of the optical modes. Thus the energy intensity has to be averaged over multiple configurations.

In the second part of the chapter we studied the localization of light in octagonal quasicrystalline layers. The crystal was generated by applying the two–stage cut and project approach on a periodic four–dimensional lattice. Then a single layer of the resulting crystal was used as the basis for the computational unit cell. To identify localized modes the scaling of the evolution of the transmission coefficients as a function of the lattice size was used. As the size of the crystal increases, and hence the number of scatterers, the transmission spectrum corresponding to the localized states exponentially decreases with the increase in the dimensions of the lattice. In contrast to the states presented previously in chapter 6, these localized modes formed resonant peaks that became prominent as the size of the lattice increased, which is considered to be an indication of critical states [46].

8. Conclusive Remarks

The control over the properties of materials at all scales is a key in advancing new technologies. The development of sophisticated photonic technologies is a rich field of science due to many facts. For instance, in the field of solar cells, the control over the photons can help improve the performance of the cell in two different ways; filtering out photons with undesired frequencies [84] and enhance the absorption of photons within a certain range of frequencies [85]. Moreover, optical fibres can perform better in guiding beams of light when the fibre core is surrounded by carefully designed photonic crystals clad [86].

The difficulty in the field of photonics arises from the fact that manufacturing devices can sometimes be sophisticated, but there is absolutely no guarantee that the desired results will be obtained. Here the numerical simulations play an important role in bridging the gap between theoretical equations and experiments carried out in the lab. The simulations often make useful predictions about the properties of the systems prior to fabrication, which cuts the financial costs and saves a lot of time.

The work carried out in this thesis primarily aimed at developing new types of numerical tools and methods to compute the optical properties of photonic crystals. A first study focused on analysing the effect of surface plasmon polaritons in photonic crystals [3]. In a two–dimensional photonic crystal with an initial photonic band gap, evanescent surface waves affects the dielectric function of the material and transform a regular, constant dielectric function into a frequency–dependent counterpart. A simple perturbation theory was developed to study the resulting photonic band structure. It turned out that the band gap in a simple photonic crystal was enhanced.

The topic optical localization in photonic crystals and quasicrystals then became the main focus for the rest of this work [2]. Two different cases of photonic quasicrystals were demonstrated. A technique to identify and quantify the localized states was developed using the transmission spectrum, as well as the inverse participation ratio. A first example characterized some states created in a dodecagonal quasiperiodic structure to be critical, although the inverse participation ratio did scale exponentially as the size of the lattice increased. However, the transmission spectrum shows the appearance of resonant states, which is a feature associated with critical

states. Furthermore, we provided another example where we demonstrate a method to identify localized states formed at defect sites in regular photonic crystals. The technique quantifies the density of the states in the vicinity of a defect site and use it as a measure of localization. Finally we analyse the states in a different quasicrystalline structure, and showed that the transmission spectrum for such structure also decays exponentially.

In the analysis carried out in this work two types of dielectric functions were used; a uniform constant dielectric function and frequency–dependent dielectric constant. The latter was modelled using a Drude–Lorentz model. Despite the success of the formula, it has some limitations when dealing with realistic structures, where other methods such as *ab initio* yield much better results compared to a simple model such as Drude–Lorentz [4, 5, 62]. However, the numerical tools as they stand are limited to these well defined formulas and can not deal with tabulated data and random dielectric function. They will have to be added to the newly developed libraries in the future.

Another problem with the current techniques is the numerical stability of some of the vital methods used. For instance, the finite–differences–time–domain method is coupled to the so–called perfectly matched layers and the results of the simulations can be affected by the values chosen for these layers. The perfectly matched layer is an imaginary material that is introduced in order to mimic the behaviour of the real system during a numerical simulation, and absorb all outgoing waves at the boundaries. A better approach should treat the boundaries as a genuine part of the system, which would improve the accuracy of the algorithm, reduce numerical errors and decouple the simulation from any artificial material.

Appendix A. The Program Design

The calculations in this work are performed using scripts written in the python programming language. These scripts extended the functionalities of the standard packages of MIT Photonic Bands (MPB) [1] for calculating the electromagnetic modes in periodic dielectric systems, and MIT Electromagnetic Equation Propagation (MEEP) [2], which implements the finite–difference–time–domain method. The main reason python scripts were developed is to use the power of python to build numerical libraries that are easy to maintain and extend. Moreover, the ultimate goal would be to develop a transparent software that offers an application programming interface (API) rather than a black box that encapsulate all the logic and offers limited entry points.

The package consists of modules where each module is meant to do a specific task. The base libraries used in the work are: python 2.7.7, python-unit, python-mockito, numpy, scipy, matplotlib, MPB and MEEP.

At a higher level, MIT packages (MPB and MEEP) play the role of the engine that performs the actual simulations, either as frequency–domain method for band structure calculation or as finite–differences–time–domain method for computational electrodynamics. The input required by those packages (control files) is provided via special python modules that build and ensure the validity of those inputs. Then, the data produced by MPB/MEEP is sent to output–processing modules for further treatment. Eventually, the resulting data is stored in binary format for future use.

In the following sections we present each of the main modules in addition to a brief description of its role with code snippets. The code is hosted on bitbucket.org which offers private free hosting for code repositories.

[1] http://ab-initio.mit.edu/wiki/index.php/MIT_Photonic_Bands

[2] http://ab-initio.mit.edu/wiki/index.php/Meep

A.1 The Modules

A.1.1 MIT Package

This modules wraps the object needed by both MPB and MEEP. It has a material, lattice, objects, control file and fields submodules. All of the mentioned submodules except the fields submodule are responsible for creating the input needed by the core engine as described in more details below. For example, the lattice module has two methods that return a string representing the lattice objects needed by MPB and MEEP:

```
from src.mit_packages.objects import Objects


class Lattice(Objects):

    def __init__(self, positions, epsilon_inf, omega=[], gamma=[], sigma=[]):
        Objects.__init__(self, epsilon_inf, omega, gamma, sigma)
        self.positions = positions

    def spheres(self, radius):
        objects = ''
        for position in self.positions:
            objects += self.sphere(position, radius)
        return objects

    def cylinders(self, radius, height):
        objects = ''
        for position in self.positions:
            objects += self.cylinder(position, radius, height)
        return objects
```

where *Objects* is used as a base class that abstract out the creation of a single object (sphere or cylinder). Each object consist of a material that has certain properties such polarization and dielectric function. The material is represented in the material class within the same package.

Finally, the control file module has one method that creates the physical control file needed to execute the simulation. The control file is generated from a basic template, which contains variable that will simply be substituted with the values generated by the other modules;

```
class ControlFile:
    def __init__(self, filename, template, replacement_dict):
        ControlFile._create(filename, template, replacement_dict)

    @staticmethod
    def _create(ctl_file, template, replacement_dict):
        controlfile = open(ctl_file, 'w')
        template = open(template)
        for line in template:
            for key, value in replacement_dict.iteritems():
                line = line.replace(key, value)
            controlfile.write(line)
        controlfile.close()
        template.close()
```

On the other hand, the fields submodule is responsible for processing the fields produced in MEEP calculations. It has special functions to find the field profiles and compute the inverse participation ratio.

A.1.2 Perturbation Package

The perturbation package is responsible for performing the band structure calculations using the perturbation theory developed in chapter 5. The results presented in Ref. [3] are produced using the same modules. The package has different classes that have different tasks; the single input module in the package is the dielectric class that computes the metallic as well the effective dielectric functions. Here is a sample of the routines, where the methods that compute the different types of dielectric functions are presented:

```
from __future__ import division
import numpy as np
import src.perturbation.base as base
```

```
def drude(omega, epsilon, sigma, omega_p, gamma):
    return epsilon + (sigma * omega_p ** 2 / (- omega ** 2 + 1j * gamma * omega))


def __oscillator__(epsilon, gamma_k, omega_k, omega_p, sigma_k, w):
    return epsilon + np.sum(
        ((sigma_k * omega_p ** 2) / (omega_k ** 2 - w ** 2 + 1j * gamma_k * w)))


def lorentz(omega, epsilon, omega_p, sigma_k, omega_k, gamma_k):
    omega = np.array(omega)
    dielectric = []
    if omega.size > 1:
        for w in omega:
            dielectric.append(
                __oscillator__(epsilon, gamma_k, omega_k, omega_p, sigma_k, w))
        return np.array(dielectric)
    else:
        return __oscillator__(epsilon, gamma_k, omega_k, omega_p, sigma_k, omega)


def effective(epsilon, epsilon_metal):
```

Prior to processing the output from the engine which is normally a plain text we have to manipulate the result to extract the data needed. The external data gets passed on to the bands class where most of the plasmonic band structure calculations are carried out. The module contains most of the logic described in Sec. (5.1) Finally, the package also has a special module to compute the density of plasmonic states.

```
import numpy as np
import os
import sys

from src.perturbation.dielectric import Dielectric
import src.perturbation.base as base
```

```
class Bands:
    def __init__(self, filename, _from, _to, default_eps, material_eps):
        self._from = _from
        self._to = _to
        self.initial = base.frequencies(filename, _from, _to)
        self.no_of_k_points = self.initial.shape[0]
        self.no_of_bands = self.initial.shape[1]
        self.default_eps = default_eps
        self.material_eps = material_eps

    def minimum(self):
        min_freqs = []
        for index in range(self.no_of_bands):
            min_freqs.append(min(self.initial[:, index]))
        return min(min_freqs)

    def maximum(self):
        max_freqs = []
        for index in range(self.no_of_bands):
            max_freqs.append(max(self.initial[:, index]))
        return max(max_freqs)

    def __frequencies__(self, steps):
        max_freq = self.maximum()
        min_freq = self.minimum()
        step = (max_freq - min_freq) / steps
        shift = 2 * step
        return np.arange(min_freq, max_freq + shift, step).tolist()

    def photonic(self):
        return self.initial

    @staticmethod
    def __any__(bands, lower_freq, upper_freq):
        indices = []
```

```
        elements = np.where((bands >= lower_freq) & (bands < upper_freq))

        for index in range(len(elements[0])):
            indices.append([elements[0][index], elements[1][index]])

        return indices

    @staticmethod
    def __update_bands__(bands, index, plasmonic_bands, is_valid):
        plasmonic_bands[index[0], index[1]] = bands[index[0], index[1]]
        is_valid[index[0], index[1]] = True

    def __compute_band_at__(self, ctrl_file, sigma, plasma_freq, omega, gamma):
        args = "plasmonicDefaultDielectric={0} plasmonicMaterialDielectric={1} "
        default_spp = Dielectric.effective(
                self.default_eps, sigma, plasma_freq, omega, gamma)
        material_spp = Dielectric.effective(
                self.material_eps, sigma, plasma_freq, omega, gamma)

        os.system(('mpb ' + args + ctrl_file + ' > tmp_output'
                   ).format(default_spp, material_spp))
        os.system('wait')

        return base.frequencies('tmp_output', self._from, self._to)

    def __plasmonic_bands__(self, lower_freq, upper_freq,
                            ctrl_file, sigma,
                            plasma_freq, gamma,
                            plasmonic_bands, isvalid):
        indices = Bands.__any__(self.initial, lower_freq, upper_freq)
        if indices:
            for index in indices:
                omega = self.initial[index[0], index[1]]
                bands = self.__compute_band_at__(
                        ctrl_file, sigma, plasma_freq, omega, gamma)
                Bands.__update_bands__(bands, index, plasmonic_bands, isvalid)
```

```
    @staticmethod
    def store(filename, data):
        np.save(filename, data)

    @staticmethod
    def load(filename):
        return np.load(filename)

    def plasmonic(self, ctrl_file, sigma, plasma_freq, gamma, steps):
        plasmonic_bands = np.zeros(
                (self.no_of_k_points, self.no_of_bands), dtype=float)
        isvalid = np.zeros((self.no_of_k_points, self.no_of_bands), dtype=bool)
        _frequencies = self.__frequencies__(steps)
        steps += 2

        for step in range(len(_frequencies) - 1):
            lower_freq = _frequencies[step]
            upper_freq = _frequencies[step + 1]
            self.__plasmonic_bands__(lower_freq, upper_freq,
                                     ctrl_file, sigma,
                                     plasma_freq, gamma,
                                     plasmonic_bands, isvalid)

        if np.any(isvalid is False):
            sys.exit('Some frequencies were not considered in the process!')
        else:
            return plasmonic_bands
```

A.1.3 Lattice Package

In this package we gather the modules responsible for creating lattice points. For the first release, there is a single module, quasicrystals, that takes a higher dimensional vector and carries out the cut and project scheme to produce a quasicrystalline structure in lower dimensions.

```
from __future__ import division
```

```
from src.helpers import gram_schmidt
import numpy as np
import sys
import itertools


class Quasicrystal:
    def __init__(self, lattice_vectors, projection_vectors):
        self.unit_vectors = lattice_vectors
        self.projection_vectors = projection_vectors

    def __is_orthogonal__(self):
        transpose = self.projection_vectors.transpose()
        product = np.dot(self.projection_vectors, transpose)
        diagonal = product.diagonal()
        identity = diagonal * np.identity(self.projection_vectors.shape[0])
        if np.allclose(product, identity):
            return True
        return False

    def orthogonalize_basis(self):
        vec1 = np.dot(self.unit_vectors[0],
                      self.projection_vectors.transpose())[0: 3]
        vec2 = np.dot(self.unit_vectors[1],
                      self.projection_vectors.transpose())[0: 3]
        vec3 = np.dot(self.unit_vectors[2] +
                      self.unit_vectors[3],
                      self.projection_vectors.transpose())[0: 3]
        projected_vectors = np.array([vec1, vec2, vec3])

        return gram_schmidt.orthogonalize(projected_vectors)

    def __first_projection__(self, generator):
        return np.dot(generator, self.unit_vectors)

    def __second_projection__(self, crystal_vortex, window=None):
```

```
        norm = np.linalg.norm(crystal_vortex)
        if window is None or norm <= window:
            return (crystal_vortex * self.projection_vectors).sum(axis=1)
        return None

    def __map_vertices__(self, _from, _to, projected_vertices, window=None):
        dimensions = len(self.unit_vectors)
        for generator in itertools.product(range(_from, _to), repeat=dimensions):
            crystal_vortex = self.__first_projection__(generator)
            projected_vertices.append(
                self.__second_projection__(crystal_vortex, window))

    def project(self, _from, _to, window=None):
        projected_vertices = []
        if self.__is_orthogonal__():
            self.__map_vertices__(_from, _to, projected_vertices, window)
            projected_points = filter(lambda element: element is not None,
                                      projected_vertices)
            return np.array(projected_points)
        sys.exit('Projection vectors are not orthogonal')

    def layer(self, _from, _to, window, delta):
        layer = []
        lattice = self.project(_from, _to, window)[:, :3]
        basis = self.orthogonalize_basis()
        layer_direction = basis[0]
        _zeta = np.linalg.norm(layer_direction)
        _min = delta
        _max = _zeta + delta
        for vector in lattice:
            base3norm = np.dot(vector, layer_direction)
            if _min < base3norm <= _max:
                vec1 = np.dot(vector, basis[0])
                vec2 = np.dot(vector, basis[1])
                vec3 = np.dot(vector, basis[2])
                layer.append([vec1, vec2, vec3])
```

```
        if layer:
            return np.array(layer)
        else:
            sys.exit('There is no layer at the provided coordinates')

    @staticmethod
    def scale(scaling_vector, projected_points):
        return scaling_vector * projected_points

    @staticmethod
    def store(filename, data):
        np.save(filename, data)

    @staticmethod
    def load(filename):
        return np.load(filename)
```

The package played the central role in providing input points for the lattice module presented in Sec A.1.1.

A.2 Summary

The package is evolving rapidly however we are limited by the capabilities of the core engine. Some of these features can be extended outside the core engines by writing routines to process the output. Unfortunately, even those extendible features can not go much beyond what is supported by MPB and MEEP. For instance, the types of dielectric functions supported by both MIT packages is very limited; MPB accepts only constant dielectric functions and that was the main reason for developing the perturbation technique, while MEEP somehow supports frequency–dependent dielectric function, but they have to be in a specific format. In the future we are considering the removal of third party dependencies and write our own python–based core engines.

Appendix B. A Simple Perturbative Tool To Calculate Plasmonic Photonic Bandstructures

In this appendix we attach our work that has been cited in [3]. It is co-authored by Alex Quandt. The content as well as the results are summarized in chapter 5.

Optical Materials 56 (2016) 107–109

Contents lists available at ScienceDirect

Optical Materials

journal homepage: www.elsevier.com/locate/optmat

A simple perturbative tool to calculate plasmonic photonic bandstructures

Faris Mohammed [a,b,*], Alexander Quandt [a,b,c]

[a] School of Physics, University of the Witwatersrand, Johannesburg, South Africa
[b] Materials for Energy Research Group, University of the Witwatersrand, Johannesburg, South Africa
[c] DST–NRF Centre of Excellence in Strong Materials, University of the Witwatersrand, Johannesburg, South Africa

ARTICLE INFO

Article history:
Received 11 November 2015
Received in revised form 22 December 2015
Accepted 23 December 2015
Available online 28 December 2015

Keywords:
Frequency domain methods
Perturbation theory
Plasmonic photonic crystals
Photonic band gap
Numerical methods

ABSTRACT

We use first order perturbation theory to study the effect of surface plasmon polaritons on the photonic band structure of plasmonic photonic crystals. Our results are based on a simple numerical tool that we have developed to extend the standard frequency domain methods to compute the photonic band structure of plasmonic photonic crystals. For a two-dimensional honeycomb photonic crystal with a lattice constant of 500 nm placed on an aluminium substrate, we show that the band gap for TM modes is enhanced by 13%. Thus a slight variation in the effective dielectric function results in a plasmonic band structure that is not scale-invariant, which is reminiscent of the inherent non-linear properties of the effective dielectric constant.

© 2015 Elsevier B.V. All rights reserved.

1. Introduction

The interaction between the free electrons and the optical electromagnetic waves at the interface between a metal and a dielectric material results in evanescent electromagnetic waves known as surface plasmon polaritons (SPP). Due to their evanescent character the wavelength of SPP can be shorter than the wavelength of their optical counterparts in the dielectric medium [1–4]. Similar to light, the surface plasmons can also be manipulated by a photonic crystal placed on a metallic surface, a particular case that will be examined in this study.

SPP waves play an important role in the field of photonics due to their potential applications and interesting physics. In previous studies Raman scattering is enhanced using the localised surface plasmon resonance [5]. Also surface plasmons can enhance the absorption of light which can be used to improve the efficiency of solar cells [6]. For plasmonic photonic crystals a bandgap is found to open up at a specific frequency range in periodic structures due to Bragg resonance at the boundaries of the Brillouin zone leading to the development of waveguides [7,8], high efficiency Bragg reflectors and resonators [9,10]. Moreover, a one-way waveguide can be achieved under static magnetic fields [11].

In order to predict the optical properties of such devices, one needs the systematic analytical methods similar to the plane wave expansion method [12] and multiple scattering theory [13]. In this paper we present a perturbative approach to numerically compute the effect of SPP on photonic crystals characteristics, which leads to a systematic correction of the band structure of a reference dielectric photonic crystal. In the following section we will briefly describe the theoretical background of the first-order perturbation method used in this study. The last section contains some numerical results obtained for a two-dimensional honeycomb plasmonic photonic crystal. We will close with a short discussion of our results.

2. Perturbation theory

A slight variation of the dielectric function necessary to describe plasmonic photonic crystals might introduce non-linearities as well as absorption [14]. Such slight modifications will lead to a slight modification of the resulting band structures. For such cases the change in frequency $\Delta\omega$ as a function of the frequency ω, the change in the dielectric function $\Delta\varepsilon$ and the electric field $E(r)$ is:

$$\Delta\omega = -\frac{\omega}{2}\frac{\int d^3r\Delta\varepsilon \mid E(r)\mid^2}{\int d^3r\varepsilon \mid E(r)\mid^2}. \quad (1)$$

* Corresponding author at: School of Physics, University of the Witwatersrand, Johannesburg, South Africa.
E-mail address: faris@aims.ac.za (F. Mohammed).

http://dx.doi.org/10.1016/j.optmat.2015.12.037
0925-3467/© 2015 Elsevier B.V. All rights reserved.

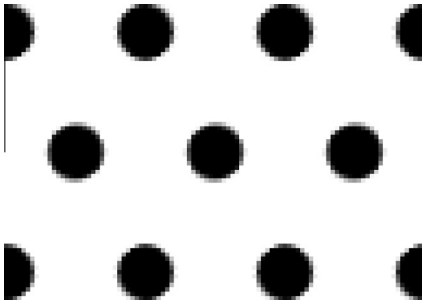

Fig. 1. A schematic diagram for a 2D honeycomb photonic crystal.

Placing the photonic crystal on a metallic substrate alters the dielectric function, yielding an effective dielectric function ε_{spp} [15]

$$\varepsilon_{spp}(\omega) = \frac{\varepsilon_m(\omega)\varepsilon(\overline{r})}{\varepsilon_m(\omega) + \varepsilon(\overline{r})} \tag{2}$$

where $\varepsilon(\overline{r})$ is the composite dielectric function of the photonic crystal and $\varepsilon_m(\omega)$ is the metallic dielectric function. The latter is modelled using a Drude formula

$$\varepsilon_m = 1 - \frac{\omega_p^2}{\omega^2 - i\omega\gamma} \tag{3}$$

where ω_p is the plasma frequency of the metal and γ is a damping constant. However, for our simulation we only consider the real part of the dielectric function, owing to the fact that the band structure is not affected by the imaginary part [16], which only leads to a gradual decay of the surface waves.

To compute the correction in the harmonic mode numerically we use a first order (self-consistent) perturbation theory. In other words, we first compute the band structure using a suitable dielectric constant for the regular photonic crystal. Then, within a small window of frequencies, ω to $\omega + \Delta\omega$, we compute the change in the frequency using a standard frequency domain code [12]. We thus assume that within the small frequency window chosen, the effective dielectric function will not fluctuate very wildly, and therefore the resulting band structures are approximately self-consistent.

For this to work, we have to ensure that for a given range of frequencies, the relative change in the dielectric constant $(\Delta\varepsilon/\varepsilon)$ is less than 1%, such that Eq. (1) will give the main perturbative corrections. Under such conditions a first order perturbation theory is sufficient. However, larger fluctuations in the dielectric function might require higher order perturbation theories, or even iterative schemes.

3. Results

We compute the photonic band structure for a two-dimensional honeycomb lattice consisting of cylinders of radius $r = 0.2\alpha$, where α is the lattice constant, see Fig. 1. The cylindrical rods are made of silicon with dielectric constant of 13, and they are embedded in

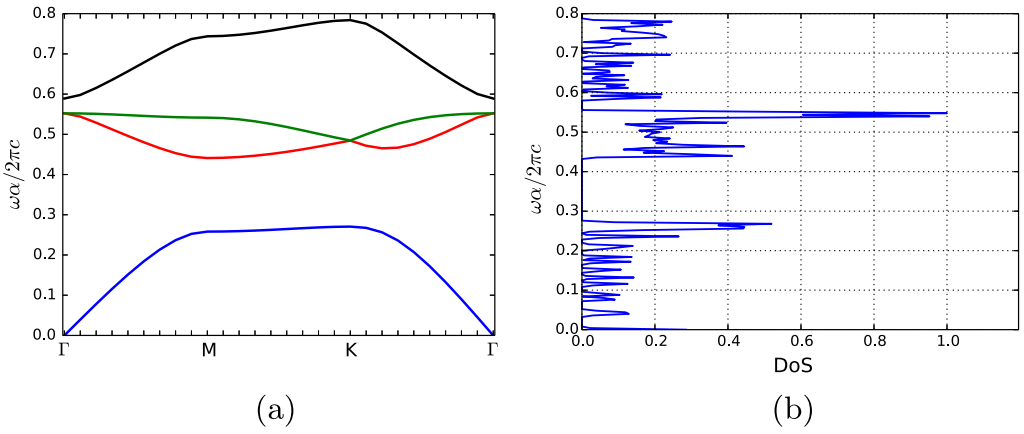

Fig. 2. (a) TM modes in units of $\frac{\alpha}{2\pi c}$ for a honeycomb photonic crystal. In (b) we show the corresponding scaled density of states (DoS).

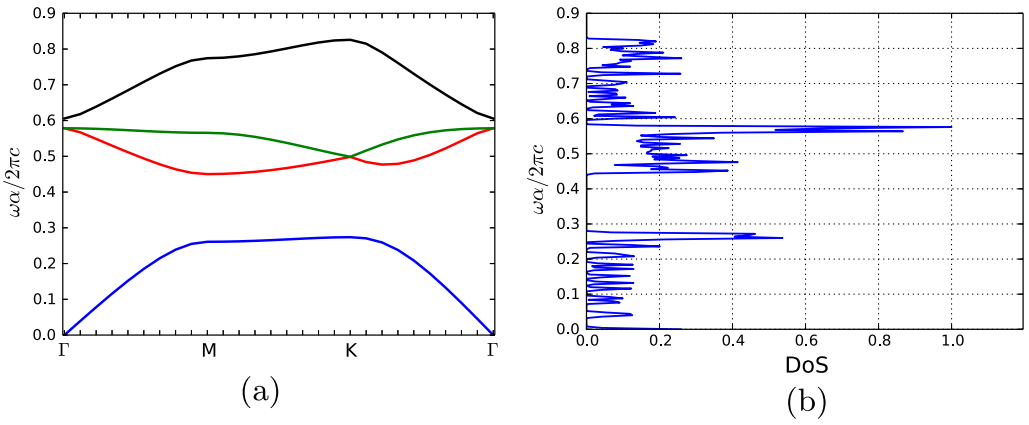

Fig. 3. (a) The plasmonic band structure computed using perturbation theory. The metallic surface used is Aluminium with $\omega_p = 2.24 \times 10^{16}$ rad/s and $\gamma = 1.22 \times 10^{14}$ rad/s. The lattice constant α is taken to be 500 nm. The frequencies are again represented in units of $\frac{\alpha}{2\pi c}$. In (b) we show the corresponding scaled density of states (DoS).

vacuum. Such high dielectric contrast increases the chances of forming a photonic band gap.

In Fig. 2a we show the TM mode photonic band structure in units of $\frac{\alpha}{2\pi c}$, where c denotes the speed of light. The density of photonic states is shown in Fig. 2b. This photonic crystal has a photonic band gap of width 0.14 $\frac{\alpha}{2\pi c}$ appearing between frequencies 0.28 $\frac{\alpha}{2\pi c}$ and 0.42 $\frac{\alpha}{2\pi c}$. A smaller band gap of width 0.02 $\frac{\alpha}{2\pi c}$ is observed at higher bands.

To study the effect of the plasmons, we use a Drude model for aluminium with a plasma frequency $\omega_p = 2.24 \times 10^{16}$ rad/s and a damping constant γ of 1.22×10^{14} rad/s [17]. The metallic dielectric function at a given frequency ω in Eq. (3) requires a specification of realistic plasma frequencies. We then have to match those frequencies to the general band structure presented in Fig. 2a, which is scale-invariant. As a result the dielectric function becomes frequency-dependent (Eq. (2)). More importantly, the resulting solutions of Maxwell's equations are no longer scale-invariant, and the band structure will depend on the dimensions of a given plasmonic system.

In Fig. 3a the band structure for a honeycomb photonic crystal placed on an aluminium substrate is shown for lattice constant $\alpha = 500$ nm. For lower bands the effect of the plasmons is not remarkable, due to the small change in the dielectric function at low frequencies. Moreover, the lowest band appears to be flat along M–K vectors, which is an indication of localised states. The higher bands, however, have shifted their positions and a wider band gap is reported. For instance, the band gap between the first and the second band has increased to 0.17 $\frac{\alpha}{2\pi c}$, which corresponds to an increase of approximately 13% . However, the bands at higher frequencies do not change in width.

4. Conclusion

We have developed a numerical tool based on first-order perturbation theory to study the photonic band structure of surface plasmon polaritons at the interface between a honeycomb photonic crystal and a metallic substrate. The metallic dielectric function is modelled by a Drude function, and only the real part of the resulting effective dielectric function for the plasmonic surface waves is used to compute the corresponding plasmonic photonic band structure.

According to our treatment, the surface plasmon waves break the scale invariance of Maxwell's equations. That could be of great interest since one geometry with different lattice sizes can control the flow of the light quite differently. Moreover we noticed an increase in the size of the band gap at low frequencies. However, the Drude approach might be largely misleading in this aspect, since the overall change in the dielectric function at such frequencies can be quite remarkable. A treatment using tabulated metallic dielectric data as a function of frequency might be a better a approach, together with tabulated data of the dielectric components of the photonic crystals. Such data can be taken from experiment, or obtained from numerical studies using ab initio methods based on density functional theory [18].

Acknowledgments

The authors would like to thank the National Institute for Theoretical Physics (NITheP), the Mandelstam Institute for Theoretical Physics (MITP) and the DST-NRF Centre of Excellence in Strong Materials (CoE-SM) for support. We also acknowledge additional support through a bilateral project *Plasmonics for a better efficiency of solar cells* between South Africa and Italy (contributo del Ministero degli Affari Esteri e della Cooperazione Internazionale, Direzione Generale per la Promozione del Sistema Paese).

References

[1] H. Raether, Surface Plasmons on Smooth and Rough Surfaces and on Gratings, Springer, Berlin, 1988.
[2] S.A. Maier, Plasmonics: Fundamentals and Applications, Springer, New York, 2007.
[3] W.L. Barnes, A. Dereux, T.W. Ebbesen, Review article surface plasmon subwavelength optics, Nature 424 (2003) 824–830.
[4] E. Ozbay, Plasmonics: merging photonics and electronics at nanoscale dimensions, Science 311 (5758) (2006) 189–193.
[5] S. Guddala, S.A. Kamanoor, A. Chiappini, M. Ferrari, N.R. Desai, Experimental investigation of photonic band gap influence on enhancement of raman-scattering in metal–dielectric colloidal crystals, J. Appl. Phys. 112 (084303) (2012) 1–7.
[6] N.N. Lal, B.F. Soares, J.K. Sinha, F. Huang, S. Mahajan, P.N. Bartlett, N.C. Greenham, J.J. Baumberg, Enhancing solar cells with localized plasmons in nanovoids, Opt. Exp. 19 (12) (2011) 11256–11263.
[7] S.I. Bozhevolnyi, J.E. Erland, K. Leosson, P.M.W. Skovgaard, J.M. Hvam, Waveguiding in surface plasmon polariton band gap structures, Phys. Rev. Lett. 86 (14) (2001) 3008–3011.
[8] C. Marquart, S.I. Bozhevolnyi, K. Leosson, Near-field imaging of surface plasmon-polariton guiding in band gap structures at telecom wavelengths, Opt. Exp. 13 (9) (2005) 3303–3309.
[9] M.U. Gonzlez, J.-C. Weeber, A.-L. Baudrion, A. Dereux, A.L. Stepanov, J.R. Krenn, E. Devaux, T.W. Ebbesen, Design, near-field characterization, and modeling of 45 surface-plasmon Bragg mirrors, Phys. Rev. B 73 (15) (2006) 155416–155429.
[10] J.-C. Weeber, A. Bouhelier, G.C. des Francs, L. Markey, A. Dereux, Submicrometer in-plane integrated surface plasmon cavities, Nano Lett. 7 (5) (2007) 1352–1359.
[11] Z. Yu, G. Veronis, Z. Wang, S. Fan, One-way electromagnetic waveguide formed at the interface between a plasmonic metal under a static magnetic field and a photonic crystal, Phys. Rev. Lett. 100 (02) (2008) 023902–023906.
[12] S.G. Johnson, J. Joannopoulos, Block-iterative frequency-domain methods for maxwell's equations in a planewave basis, Opt. Exp. 8 (3) (2001) 173–190.
[13] B. Ravel, A practical introduction to multiple scattering theory, J. Alloys Comp. 401 (1–2) (2005) 118–126.
[14] J.D. Joannopoulos, S.G. Johnson, J.N. Winn, R.D. Meade, Photonic Crystals Molding the Flow of Light, second ed., Princeton University Press, 2008.
[15] L. Feng, M.-H. Lu, V. Lomakin, Y. Fainman, Plasmonic photonic crystal with a complete band gap for surface plasmon polariton waves, Appl. Phys. Lett. 93 (23) (2008) 231105.
[16] L. Feng, X.-P. Liu, Y.-F. Tang, Y.-F. Chen, J. Zi, S.-N. Zhu, Y.-Y. Zhu, Tunable negative refraction in a two-dimensional active magneto-optical photonic crystal, Phys. Rev. B 71 (19) (2005) 195106–195112.
[17] I. El-Kady, M.M. Sigalas, R. Biswas, K.M. Ho, C.M. Soukoulis, Metallic photonic crystals at optical wavelengths, Phys. Rev. B 62 (23) (2000) 15229–15302.
[18] Ab initio simulations of optical materials, in: 2014 16th International Conference on Transparent Optical Networks (ICTON), IEEE, 2014.

Appendix C. About Optical Localization In Photonic Quasicrystals

This appendix includes the work that has been cited in [2], and presented in chapter 6. The technique developed throughout the work is also used in the simulations carried out in Sec. 7.2. It is co-authored by Alex Quandt.

Opt Quant Electron (2016) 48:380
DOI 10.1007/s11082-016-0648-1

About optical localization in photonic quasicrystals

Faris Mohammed[1,2] · **Alexander Quandt**[1,2,3]

Received: 10 August 2015 / Accepted: 7 July 2016 / Published online: 12 July 2016
© Springer Science+Business Media New York 2016

Abstract We employ the two stage cut and project scheme to generate a dodecagonal two-dimensional quasiperiodic structure. The finite-differences-time-domain method is applied to simulate the propagation of electromagnetic modes in the system. We compute the transmission coefficients as well as the inverse participation ratio for a quasicrystal consisting of dielectric cylindrical rods. We find that for a small crystal the band gap forms due to destructive interference between extended states. The quasiperiodic geometry exhibits modes with enhanced transmission coefficients. The inverse participation ratio analysis indicates that these modes are localized and that the localization length is estimated to be 0.3207 in the inverse units of a lattice characteristic length scale.

Keywords Photonic quasicrystals · Optical localization · Finite-differences-time-domain method

This article is part of the Topical Collection on Optical Wave and Waveguide Theory and Numerical Modelling, OWTNM' 15.

Guest edited by Arti Agrawal, B.M.A. Rahman, Tong Sun, Gregory Wurtz, Anibal Fernandez and James R. Taylor.

✉ Faris Mohammed
faris@aims.ac.za

Alexander Quandt
alex.quandt@wits.ac.za

[1] School of Physics, University of the Witwatersrand, Johannesburg, South Africa

[2] Materials for Energy Research Group, University of the Witwatersrand, Johannesburg, South Africa

[3] DST-NRF Centre of Excellence in Strong Materials, University of the Witwatersrand, Johannesburg, South Africa

1 Introduction

In the field of photonics the search for novel types of band gap materials has been a major motivation for scientists to explore a large variety of different structures. Periodic structures, for instance, have interesting properties and a wide range of applications (see Vardeny et al. 2013; Jin et al. 2013 for review). However, the limited number of allowed geometries has culminated in the growing interest in aperiodic structures with a wide variety of different candidate geometries for photonic band gap materials, and hence a much richer physics. Of particular interest are quasicrystals (QCs), which are well organized structures that lack translational symmetry on the short range (Janot 1994). But they obviously display some aperiodic long range order, as suggested by their sharp and unusual diffraction patterns (Shechtman et al. 1984).

Photonic quasicrystals (PQCs) have been shown to give rise to photonic band gaps formed via Braag scattering (Edagawa 2014). In one-dimension (1D) band gaps have been found in Fibonacci-like QCs (Gellermann et al. 1994; Hattori et al. 1994), and the higher dimensional octagonal quasicrystals were also shown to form a band gap (Zhang et al. 2001). Interestingly, a band gap for a very low refractive index contrast has been reported for dodecagonal QCs (Zoorob et al. 2000). Moreover, related effects such as field enhancement and slow modes at the band edge were observed in various experimental studies (Dal Negro et al. 2003). In addition to that, photonic modes were found to be localized in tenfold Penrose tiling. In such structures localized modes were associated with the tunnelling phenomena and the presence of fast light (Neve-Oz et al. 2010). Experimentally, the localized states were observed in Fibonacci sequences where the transmission scales and the light propagation is enhanced due to resonant localized states (Kohmoto et al. 1987).

In this study we investigate the optical properties of two-dimensional (2D) photonic quasicrystals. Our aim is to quantify the localization of the photons in the novel 2D dodecagonal lattice, using the standard time domain methods to evaluate the transmission coefficients. Optical localization itself is determined using the analytical concept of an inverse participation ratio (IPR).

In the following section we first describe the two-stage-projection method to construct quasicrystalline structure, and then give the technical details of the time domain simulation. Thereafter, the presentation of our findings will proceed.

2 Modelling

Unique properties of PQCs such as a complete band gap at low index contrast (Zoorob et al. 2000; Zhang et al. 2001) are attributed to high statistical symmetries (Della Villa et al. 2006). The richness comes with the complexity of the mathematical modelling of quasi-crystalline structures, in particular their relations to higher dimensional lattices. Quasicrystals are generated systematically using different mathematical techniques, with the cut and project technique being the most prominent one (Janot 1994). Although it is hard to find all of the resulting structures in nature in the form of intermetallic alloys, the various quasicrystalline structures that can be generated by the cut and project method may easily be realized as photonic quasicrystals. Therefore the cut and project scheme allows us to construct whole families of easy-to-generate but sufficiently complex quasiperiodic lattices to systematically study photonic band gaps and optical localization.

2.1 Two-stage-projection

For the cut and project scheme we consider a periodic structure in a higher dimensional space R^D, where D represents the dimensions of the space. If we try to project all of the lattice points into a lower d-dimensional subspace $R^d_{\parallel}$ known as parallel or physical space, we will simply end up with a periodic or a dense set of lattice points, both of which will be of little use. In order to produce a discrete and aperiodic set of points in $R^d_{\parallel}$, we introduce an intermediate subspace known as the perpendicular space $R^c_{\perp}$ with dimensionality equal to c where $R^D = R^d_{\parallel} \times R^c_{\perp}$. We then define an acceptance domain Γ in $R^c_{\perp}$, which is simply the projection of a unit cell of R^D onto $R^c_{\perp}$. Next we project the points of the R^D lattice whose projection onto $R^c_{\perp}$ falls into the acceptance domain Γ (Janot 1994).

The so called two-stage projection method employs cut and project techniques to map higher-dimensional lattices onto lower-dimensional laminar (i.e. layered) structures, using only one-dimensional acceptance domains (Ben-Abraham 2007). This has a clear numerical advantage over other schemes, which have to fallback on quite complicated and even fractal acceptance domains (Janot 1994).

In principle the two state projection method consists of two cut and project steps. The tricky step is the former, which will project a higher-dimensional lattice in R^D onto a lattice in $R^{D-1}_{\parallel}$, using a 1D acceptance domain in $R^1_{\perp}$. Assuming that $R^{D-1}_{\parallel} = R^{\delta} \times R^{\gamma}$, we can apply the cut and project scheme a second time in order to generate the final aperiodic structure in R^{δ}, using R^{γ} as acceptance domain. Examples are given in (Ben-Abraham 2007).

In the following section we map a lattice from 4-dimensional space onto a laminar structure in 3-dimensional space. Each layer contains 2D quasiperiodic structures, hence the second application of the cut and project scheme is rather trivial. We then extract the quasiperiodic structures from all the layers that are periodically spanned along the z-axis. Finally we collapse the layers onto a 2D x-y plane forming the basis of the lattice used for our simulations.

2.2 Finite difference time domain method

In this report a finite-difference-time-domain solver (FDTD) (Oskooi et al. 2010) is used to characterize the localized optical modes in a 2D quasicrystal. The samples are patches from QC's which are generated using a specific window size to limit the number of the mapped points. The smaller the window, the fewer the points mapped, and hence a smaller QC lattice is produced. The patches generated have a length L and a width W. All dimensions are given in terms of a characteristic length scale α.

However, to run the simulation and achieve stable results, we introduce a simulation lattice that has dimensions greater than those of the generated quasicrystal. The QC was then placed at the center of the simulation lattice. The gap between the edges of the crystal and the borders of the simulation cell is filled with perfectly matched layers (PML). We ensured that the thickness of the PML is sufficient for the electromagnetic modes to decay and that no backward reflection is encountered during the simulations.

A Gaussian source is positioned at the center of the simulation cell. The source center frequency is 0.5, and it has width of 0.55 both in units of $\alpha/2\pi c$ where c is the speed of light. The outgoing flux is measured in a direction perpendicular to the y-axis at a surface of length L. The flux quantifies the amount of energy transmitted through the surface of the structure, and it is given by:

$$P(\omega) = \hat{\mathbf{n}} \cdot \oint \mathbf{E}(\omega) \times \mathbf{H}(\omega) \mathbf{dA} \tag{1}$$

where the surface integral is the Poynting vector, and $\hat{\mathbf{n}}$ is the surface normal. Given the flux computed by Eq. (1), the transmission coefficients can be obtained as the ratio between the outgoing flux in the presence of the QC and the flux measured in a vacant simulation lattice.

3 Dodecagonal quasicrystal

In order to generate a dodecagonal quasiperiodic structure in 2D using the two-stage-projection method, we begin with a higher dimensional face-centred lattice D_4 (Ben-Abraham 2007). This lattice has much higher symmetries than lattices in three-dimensions and two-dimensions (i.e. up to twelvefold symmetry) (Baake et al. 1991; Conway and Sloane 1999), which makes it a potential candidate for forming photonic structures with particular optical properties such as complete band gap for relatively low index contrast.

The two-stage projection for the dodecagonal 2D quasiperiodic structure is based on the following orthonormal vectors (Ben-Abraham 2007)

$$\mathbf{e}_1 = \left[\frac{a}{2}, \frac{a}{2}, 0, \frac{b}{\sqrt{2}}\right]$$
$$\mathbf{e}_3 = \left[\frac{b}{\sqrt{2}}, 0, -\frac{a}{2}, -\frac{a}{2}\right]$$

where $a^2 = 1 + \frac{1}{\sqrt{3}}, b^2 = 1 - \frac{1}{\sqrt{3}}$. The vectors $\mathbf{e}_1, \mathbf{e}_2$ and $\mathbf{e}_3$ represent the basis for the parallel space $R^3_{\parallel}$ and $\mathbf{e}_4$ is the base of $R^1_{\perp}$. We project the lattice onto parallel space using an acceptance domain in the half open interval $\left(-\left(\frac{a}{2} + \frac{b}{\sqrt{2}}\right), +\left(\frac{a}{2} + \frac{b}{\sqrt{2}}\right)\right]$. The projected set of points is then represented in these transformed coordinates, and it forms a laminar 3D structure, where each layer contains a quasiperiodic dodecagonal structure, as described in Ben-Abraham (2007).

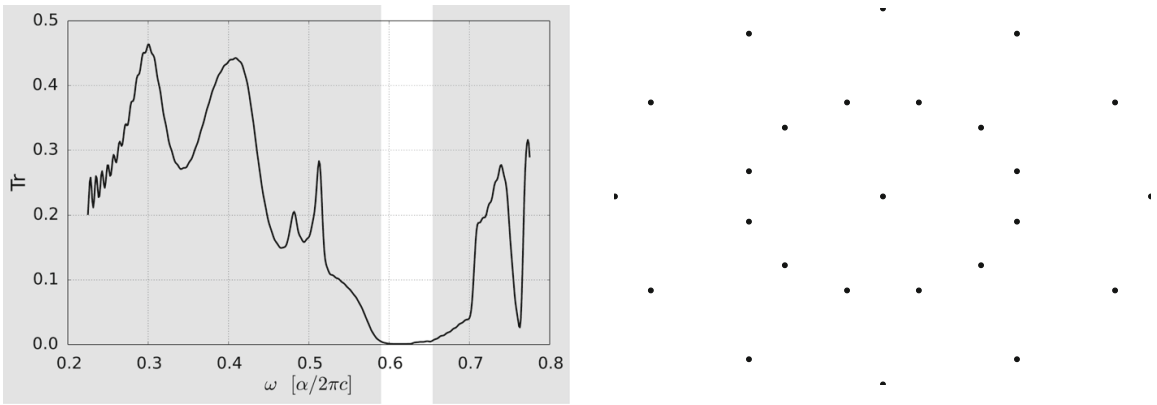

(a) (b)

Fig. 1 In **a** we plot the transmission coefficients as a function of the frequency for the crystal shown in (**b**). The frequencies are given in units of $\alpha/2\pi c$ and the lattice has dimensions of 1.5×1. The localized states falls into the frequency region with *lighter shades*

Each point in the cell is then taken to represents the center of a cylindrical object with radius r = 0.2α and dielectric constant ε = 12.4, corresponding to the dielectric constant of silicon. These cylindrical objects are surrounded by air which has a dielectric constant of 1. The height of the cylinders is set to 0.8α. The FDTD simulation is run until the field decays and the values of the field at each point in the QC is stored for every 0.05 time unit.

In Fig. 1 the transmission coefficients reaches a minimum value of zero in the frequency range 0.59–0.649 which indicates that the propagation of states within that frequency range is forbidden, and a band gap has opened. The formation of such states is be attributed to Braag scattering (Edagawa 2014), where the interference of extended states at the band gap can also lead to the formation of new states in the range (Sheng 2006). However the states at the mobility edges (close to the band gap) are likely to be localized.

To further understand the nature of the band edge states, we gradually increase the size of the window used in mapping the quasiperiodic structure points. In Fig. 2 the transmission coefficients exhibit the formation new states at the band gap due to the constructive interference between the neighbouring states formed by the presence of new scatterers. In contrast to a 1D case where the transmission decays exponentially as a function of the crystal size (Sheng 2006), the results presented in Fig. 2a, d show an enhancement in the transport around the band gap frequency. In a 2D world, the scaling theory is a bit more complex, and such changes in the transmission could belong to either localized or critical states. We hence plot the field profiles for different cell sizes as a

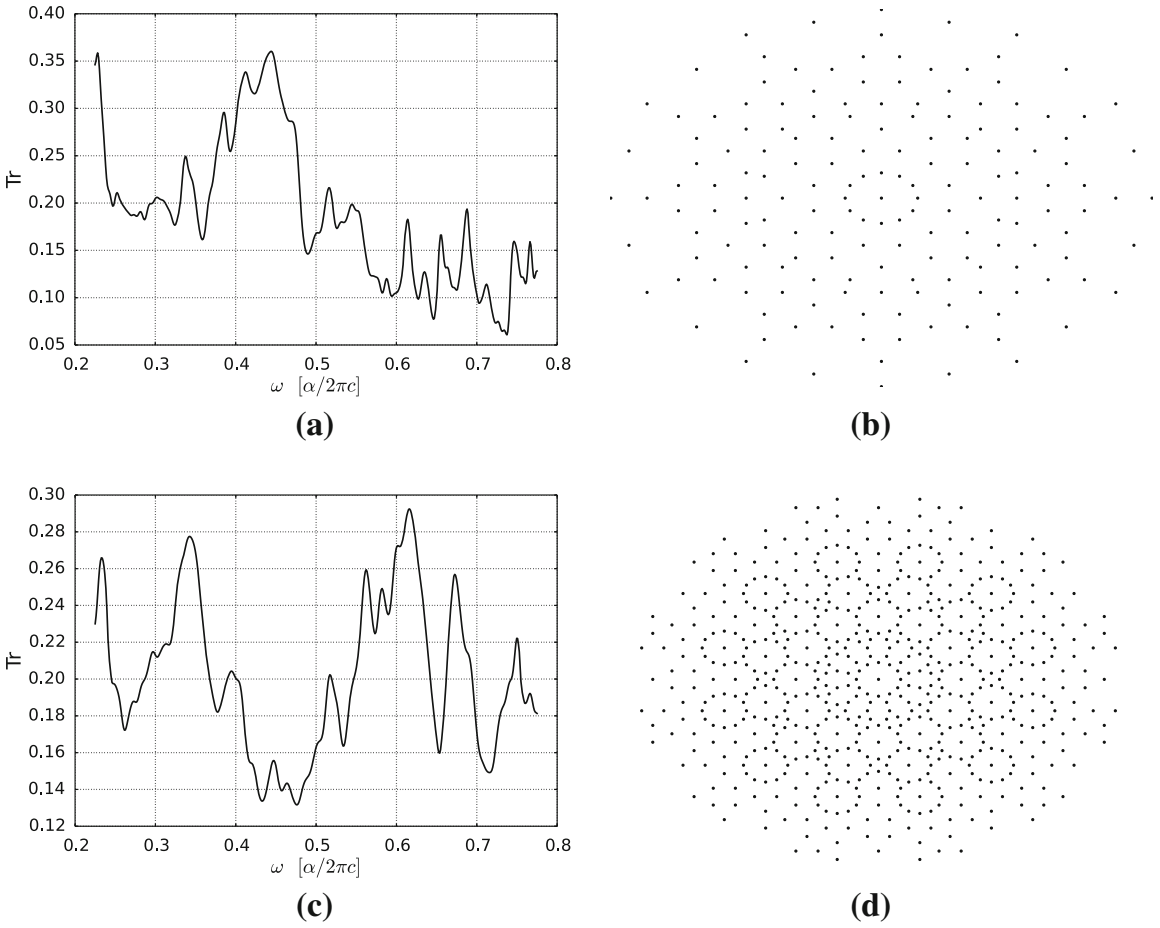

Fig. 2 In **a** and **c** we plot the transmission coefficients that corresponds to crystals shown in (**b**) and (**d**) respectively. The crystal (**b**) has dimensions of 6 × 4 and **d** is 8.58 × 5.72

function of the frequency. To this end, we accumulate the Fourier transformations of the fields at each point in space, and plot a contour of the field profiles in the lattice.

For a crystal with dimension $3 \times 2[\alpha^2]$ the fields tend to spread across the lattice and position themselves around regions with high dielectric as shown in Fig. 3a. As the QC size increases, Fig. 3b–d, we observe strong attenuation of the fields in regions that previously had high intensity which is due to the scattering from the extra lattice points. However, for the larger cells presented in Fig. 3c, d, the profile patterns do not vary remarkably and the modes are trapped at the vicinity of the Gaussian source. Some of these patterns are a visual indication that there are localized states forming in parts of the structure. Having in mind the enhancement in light propagation near band gap as seen in Fig. 2a, c, we further identify these modes as resonant modes.

Finally we perform the inverse participation ratio IPR analysis to identify localized states. The inverse participation ratio is given by

$$\mathrm{IPR}(\omega) = \frac{\sum_{\underline{\mathbf{r}}} |\Psi(\omega, \underline{\mathbf{r}})|^4}{\left[\sum_{\underline{\mathbf{r}}} |\Psi(\omega, \underline{\mathbf{r}})|^2\right]^2} \tag{2}$$

where the sum runs over all the points in real space. The localized states are identified by an IPR that is proportional to $\exp(-2\zeta L)$ where L is the size of the sample in the direction

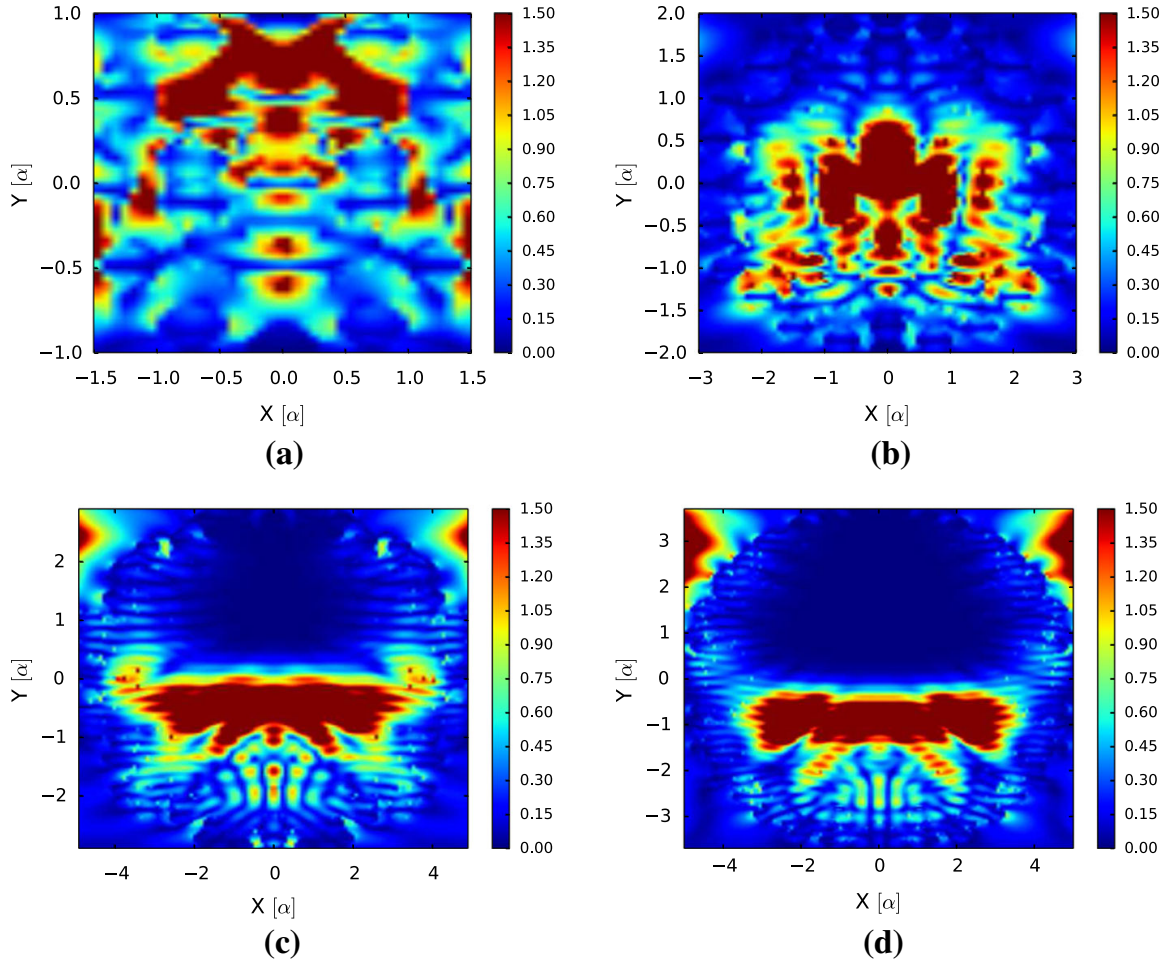

Fig. 3 The *contour* represents the field profiles for a Gaussian source at the center of QC patches with dimensions **a** 3×2, **b** 6×4, **c** 8.58×5.72 and **d** 10.1×6.74 in units of α^2. Only modes with frequencies near the band gap are presented. The *colour-map* shows the intensity distribution in the crystal

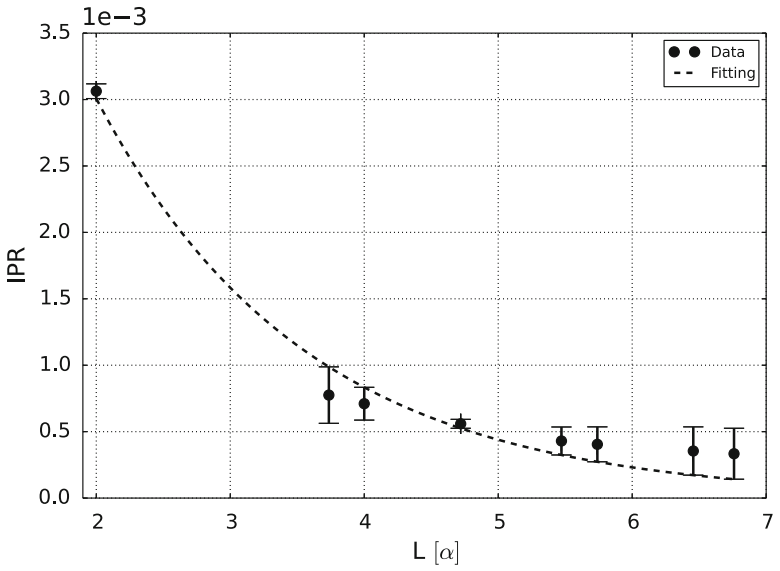

Fig. 4 The decay of the inverse participation ratio as a function of the lattice size. The IPR values were extracted at frequencies between 0.59 and 0.649 (in units of $\alpha/2\pi c$) and averaged out. The *error bars* shown in the figure represent the deviation between the data points and the fitting

of the modes propagation. In other words, a localized state shows an exponentially decaying inverse participation ratio with increasing the system size. As the system size approaches the infinity, the IPR for localized states becomes constant.

In Fig. 4 we present the inverse participation ratio of the modes near the mobility edges as a function of the lattice size L. We use a least-squares fitting to determine the localization length ζ from the IPR around the band gap edges. We estimate that the localization length for the QC to be $\sim 0.3207[\alpha^{-1}]$.

4 Summary

We have investigated the localization of electromagnetic modes in a 2D quasiperiodic photonic crystal. The sample structure was generated using a two stage projection scheme leading to a laminar three-dimensional QC, where we map all layers into a single dodecagonal QC. The number of points mapped from a higher dimension space was systematically increased leading to larger and larger patches. The lattice points were taken as centres of cylindrical objects of radius 0.2 α where α is a characteristic lattice length. These cylinders have a dielectric constant of 12.4, whereas the surrounding media has a dielectric constant of 1.

Performing finite-differences-time-domain simulations, we observed a photonic band gap at frequencies 0.59–0.649 (in units of $\alpha/2\pi c$). Increasing the size of the QC patches, we observed the formation of new states at the band gap. Such states are a result of a constructive interference of states at the band gap.

Plotting the field profiles showed that field intensities are diminishing at intermediate frequencies as the size of the crystal increased, and hence the number of the scatterers. The inverse participation ratio showed that some states near the mobility edges are localized. The localization length is estimated from the scaling theory to be around $0.3207[\alpha^{-1}]$. An Interesting open problem like the appearance of critical states in 2D and 3D disordered structures (Sheng 2006) could be answered by carrying out more systematic studies, where the analytical tools presented in this study should be of great use.

Acknowledgments The authors would like to thank the National Research Foundation (NRF) and the Department of Science and Technology (DST) for financial support.

References

Baake, M., Joseph, D., Schlottmann, M.: The root lattice D_4 and planar quasilattices with octagonal and dodecagonal symmetry. Int. J. Mod. Phys. B **05**, 1924 (1991)

Ben-Abraham, S.I., Alexander, Q.: Hybrid quasiperiodic-periodic structures constructed by projection in two stages. Acta Crystallogr. **A63**, 177–185 (2007)

Conway, J.H., Sloane, N.J.A.: Sphere Packings, Lattices and Groups, 3rd edn. Springer, New York (1999)

Dal Negro, L., Oton, C.J., Gaburro, Z., Pavesi, L., Johnson, P., Lagendijk, A., Righini, R., Colocci, M., Wiersma, D.S.: Light transport through the band-edge states of Fibonacci quasicrystals. Phys. Rev. Lett. **90**, 055501 (2003)

Della Villa, A., Enoch, S., Tayeb, G., Capolino, F., Pierro, V., Aldi, V.: Localized modes in photonic quasicrystals with Penrose-type lattice. Opt. Express **14**(21), 10021 (2006)

Edagawa, K.: Photonic crystals, amorphous materials, and quasicrystals. Sci. Technol. Adv. Mater. **15**, 034805 (2014)

Gellermann, W., Kohmoto, M., Sutherland, B., Taylor, P.C.: Localization of light waves in Fibonacci dielectric multilayers. Phys. Rev. Lett. **72**, 633 (1994)

Hattori, T., Tsurumachi, N., Kawato, S., Nakatsuka, H.: Photonic dispersion relation in a one-dimensional quasicrystal. Phys. Rev. B **50**, R4220 (1994)

Janot, C.: Quasicrystals, 2nd edn. Clarendon Press, Oxford (1994)

Jin, W., Ju, J., Ho, H.L., Hoo, Y.L., Zhang, A.: Photonic crystal fibers devices and applications. Front. Optoelectron. **6**, 3–24 (2013)

Kohmoto, M., Sutherland, B., Iguchi, K.: Localization in optics: quasiperiodic media. Phys. Rev. Lett. **58**, 23 (1987)

Neve-Oz, Y., Pollok, T., Burger, S., Golosovsky, M., Davidov, D.: Resonant transmission of electromagnetic waves through two-dimensional photonic quasicrystals. J. Appl. Phys. **107**, 063105 (2010)

Oskooi, A.F., Roundy, D., Ibanescu, M., Bermel, P., Joannopoulos, J.D., Johnson, S.G.: Meep: a flexible free-software package for electromagnetic simulations by the FDTD method. Comput. Phys. Commun. **181**, 687–702 (2010)

Shechtman, D., Blech, J., Gratias, D., Cahn, J.W.: Metallic phase with long range orientational order and no translational symmetry. Phys. Rev. Lett. **53**, 1951–1953 (1984)

Sheng, P.: Introduction to Wave Scattering, Localization, and Mesoscopic Phenomena, 2nd edn. Springer, Berlin (2006)

Vardeny, Z.V., Nahata, A., Agrawal, A.: Optics of photonics quasicrystals. Nat. Photonics **7**, 177–187 (2013)

Zhang, X., Zhang, Z.-Q., Chan, C.T.: Absolute photonic band gap in 12-fold symmetric photonic crystals. Phys. Rev. B **63**, 081105 (2001)

Zoorob, M.E., Charleton, M.D.B., Parker, G.J., Baumberg, J.J., Netti, M.C.: Complete photonic band gap in 12-fold symmetric quasicrystals. Nature **404**, 740743 (2000)

Appendix D. Computational Plasmonics: Theory and Applications

In this appendix, we include the reference cited in [4]. It is co-authored by Robert Warmbier and Alex Quandt. The content of the chapter is summarized in the sections of chapter 2.

11

Computational Plasmonics: Theory and Applications

F. Mohammed, R. Warmbier, and A. Quandt

[1] School of Physics, Centre of Excellence in Strong Materials, University of the Witwatersrand, Wits 2050, Johannesburg, South Africa
[2] Materials for Energy Research Group (MERG), University of the Witwatersrand, Wits 2050, Johannesburg, South Africa faris.aims.ac.za
[3] Centro studi e ricerche Enrico Fermi, Piazza del Viminale, 00184 Roma, Italy

Abstract. In two Chapters we will give a detailed introduction into the field of computational plasmonics. The present Chapter covers the essential theoretical background of modern plasmonics, based on simple models of light-matter interactions. We will focus on the physical properties of bulk plasmons, surface plasmon polaritons and localized plasmons, and give a number of analytical and numerical examples. As a motivation for more the detailed numerical studies described in Chapter 12, and as an example for new types of technological applications, we also present the field of plasmon enhanced solar cells and other exciting new research directions.

11.1 Introduction

Plasmonics is a branch of modern nano-optics that studies the interaction of electromagnetic waves with free charge carriers. For a typical bulk material, these free charge carriers are the electrons in the conduction band. Many light-matter interaction processes only involve the creation of a single electron-hole pair due to an incoming photon. But in the case of plasmonics we are dealing with collective excitations, i.e. processes that involve a large number of charge carriers.

This large number of charge carriers is of course a fundamental problem of plasmonics. The charge carriers that contribute to these collective phenomena will not all act as if they were part of an ideal solid, but they will also be

influenced by structural defects and large-scale features of a solid like dislocations and grains. Ultimately they may even be influenced by the shape of a nanoparticle containing these charge carriers. Therefore a typical approach to model a plasmonic system will involve multi-scale modeling at various levels of structural complexity, starting from the atomic structure of a solid. This is what the following Chapters is all about.

But it will not be a typical review article about plasmonics. Trying to put the vast literature about plasmonics into a single document will lead to a very superficial type of literature survey. The problem starts with the fact that there are several different types of plasmonic excitations in a bulk material, namely bulk plasmons, surface plasmon polaritons and localized plasmons in metallic nanoparticles. Furthermore there is a large variety of technological applications based on each of these various plasmonic excitations. And also the various theoretical and numerical methods involved in a typical multi-scale approach have their own extended literature.

In order to avoid the style of a typical literature review we will focus here and in Chapter 12 on the practice of computational plasmonics, and with some major goals: First we want to collect in one compact document the most important facts about plasmonics in general, which is the topic of the present Chapter. But we also want to present the most important facts about the various numerical techniques of computational plasmonics, which is the topic of Chapter 12. Another goal is to illustrate the practice of computational plasmonics based on a number of examples. For many readers unfamiliar with plasmonics, this hands-on approach could actually provide a better jump start than a typical extended literature survey with only cryptic explanations.

We have organized this Chapter as follows: In Sec. 11.2 we will give a general overview of light-matter interactions, where the material aspects will enter the theoretical formalism mainly through the complex dielectric tensor $\varepsilon(\omega)$ ("dielectric function"). We will content ourselves with a simple Drude–Lorentz type of mode to get some insight into the basic light-matter interaction processes in plasmonics, some of them leading to the formation of bulk plasmons, surface plasmon polaritons and localized plasmons in metallic nanoparticles.

In Sec. 11.3 we will provide more details about the application of plasmonic technologies in the field of photovoltaics. This topic is of great technological relevance, and (computational) plasmonics could make major contributions to this field in the near future.

In Sec. 11.4 we will give a brief survey of some of the most exciting new research directions in (computational) plasmonics. And finally in Sec. 11.5 we will close this Chapter with a short summary, and an outlook on the more technical Chapter 12.

11.2 Theoretical Background

We aim at a more intuitive approach to understand the basic concepts and phenomena of plasmonics, and therefore we will base our discussions of the fundamental dielectric properties of solids entirely on the Drude–Lorentz model, which is also the proper theoretical background for the most popular textbooks in the field of plasmonic nanoparticles [1, 2]. In Sec. 11.2.1 we will describe the basic dielectric properties of metals and insulators, and derive some related optical properties, which may be used to characterize plasmons. An example will illustrate the use of some of these derived optical properties.

The second part, Sec. 11.2.2, will be devoted to bulk and surface plasmons, where we will use the Drude–Lorentz model to describe the basic dielectric properties of various model systems. Furthermore we will describe the main optical properties of localized plasmon resonances in metallic nanoparticles, and as an example we will analyse the basic optical properties of gold nanoparticles.

11.2.1 Optical Properties of Solids

Light can interact with matter in various ways, some of which can actually be quite complex. Nevertheless we may start with a general picture of a chunk of matter, which consists of a skeleton of positively charged ions, held together by a negatively charged electron glue.

Depending on the nature of the chemical bond in such a chunk of matter, electrons can be strongly bound to certain types of ions, leading to an insulating or semiconducting optical material. Or the glue electrons may travel more or less freely throughout the whole bulk, which leads to a metallic system. This behaviour is covered by one of the simplest models of light–matter interactions, which is the so-called Drude–Lorentz model [3].

In the following we will develop the theoretical background to model important types of light–matter interactions, and we will also discuss some of its implications for optics and plasmonics. As we will see in Chapter 12, the more advanced approaches to model and analyse plasmonic resonances still have important features, which are already covered by the much simpler Drude–Lorentz model.

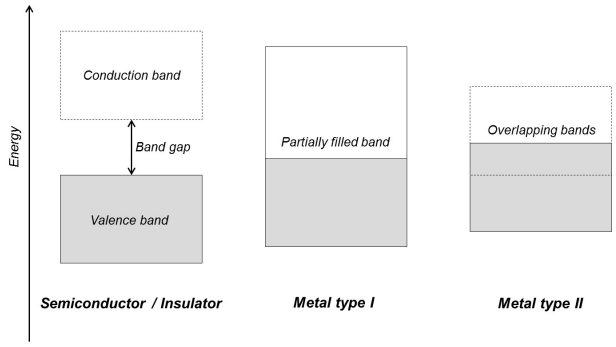

Fig. 11.1: Schematic band structures for semiconductors and insulators (left), as well as for metals (middle and right). semiconductors and insulators are marked by a band gap between a fully occupied valence band shown in grey, and an empty conduction band shown in white. metals are characterized by partially filled bands (middle), or by overlapping valence and conduction bands (right).

11.2.1.1 Metals and Insulators

For a solid with perfect translational symmetry there is a continuum of energy eigenstates described by general dispersion relations $E_i(\boldsymbol{k})$. The vectors $\boldsymbol{k}$ from reciprocal space are the so-called crystal momenta, which label electronic Bloch states as eigenstates of a crystal Hamiltonian. As shown schematically in Fig. 11.1 the difference between a semiconductor (insulator) and a metal is the location of the so-called Fermi level E_F, which separates occupied from unoccupied bands. As a basic mechanism of light–matter interactions, photons of energy $\hbar\omega$ can be absorbed by an electron, if that particular electron is able to make a transition from an occupied state characterized by $E_i(\boldsymbol{k})$ into an unoccupied electronic state characterized by $E_j(\boldsymbol{k'})$. For the energy difference ΔE between those two states we must have $\Delta E = \hbar\omega$. The transition can happen at the same point $\boldsymbol{k'} = \boldsymbol{k}$ in reciprocal space (direct transition), or at different points $\boldsymbol{k'} \neq \boldsymbol{k}$ in reciprocal space (indirect transition). In the latter case the electronic transitions will need some extra momentum, which is usually contributed by phonons.

As indicated in Fig. 11.1 all the Bloch states in the valence band are filled for a semiconductor or insulator, and there is a band gap that separates the valence band from the conduction band. This means that only photons with energies bigger than the band gap can be absorbed, and therefore semiconductors and insulators are often transparent. metals have either wide bands that are only partially filled, or they are characterized by two wide bands that actually overlap. In such a case photons can be absorbed by electrons over a large

frequency range, and an applied electric field can easily set the band electrons in motion, which makes the system a conductor.

On a more fundamental level the Bloch states for semiconductors/insulators and metals show different analytical behaviour, due to the properties of the corresponding crystal Hamiltonian and of the corresponding one-electron energies. For each of these band electrons there is always a competition between two energy terms. On one hand there is the kinetic energy which favours delocalization and thus a metallic behaviour, but there is also the potential energy term, which favours localization and thus an insulating behaviour.

In this chapter we will not consider the peculiar nature of highly correlated systems such as NiO, where band structure theory breaks down; NiO is obviously an insulator, whereas the band structure predicts that the material should be metallic. The reason for this breakdown of band theory is the electron–electron repulsion, which is not very well represented by the standard crystal Hamiltonians (for a nice elementary discussion see [4]). In this context we also want to point out the new field of topological insulators [5], where spin–orbit coupling in an insulating material can give rise to topologically protected edge states, which are chiral and conducting. We will simply assume that the band structure concept works fine, and that the Bloch states for insulators tend to be localized around certain atoms or certain regions within a solid, whereas the Bloch electrons for metals would like to go everywhere.

11.2.1.2 Frequency Dependent Dielectric Functions

The predictions made by the Drude–Lorentz model are formally based on a classical oscillator model. But they also refer to microscopic properties like electronic dipole moments , which are fundamentally quantum mechanical in nature. In order to justify such an approach, the basic equations of motion that characterize the microscopic properties must be understood in the theoretical framework of the Ehrenfest theorem [6], which states that quantum mechanical expectation values essentially obey the classical equations of motion.

Now let us build an Ehrenfest type of semi-classical oscillator model for the general interaction of electrons with photons in a solid. To this end, we start with a simple insulator model, where a nucleus with elementary charge e is located at the centre of a sphere of radius R, and this sphere is uniformly charged with the negative elementary charge of an electron. This model describes at least to some extent the localized charge densities ϱ characteristic of insulators or semiconductors, where

$$\varrho = -\frac{3e}{4\pi R^3} \tag{11.1}$$

We now assume that the nucleus is a test particle, which moves within that charged sphere. Such a motion could be induced by an external electromagnetic field. The movement of the test charge gives rise to the same forces as if the electron cloud within the sphere would move around a fixed nucleus. Using Gauss law we obtain a radially symmetric force law of the kind

$$F(r) = \frac{e^2}{4\pi\varepsilon_0}\frac{r}{R^3} \equiv -kr \,, \tag{11.2}$$

where ε_0 is the vacuum permittivity. This is obviously a harmonic restoring force with "spring constant"

$$k = \frac{e^2}{4\pi\varepsilon_0}\frac{1}{R^3} \tag{11.3}$$

The corresponding motion of the electron cloud around a nucleus (in the quasi-classical sense of the Ehrenfest theorem) would then correspond to radial harmonic oscillations with a (squared) angular frequency

$$\omega_0^2 = \frac{k}{m_e} \,, \tag{11.4}$$

where m_e is the mass of an electron. Note that for a metal, where the electrons would like to go everywhere inside the bulk material, we have to assume that R actually goes to infinity, which implies that the spring constant k will go to zero.

Now let the electron cloud of our insulator model be excited by an oscillating electric field $E(t) = E_0 \exp(i\omega t)$. That will lead to the following equation of motion:

$$m_e \frac{\mathrm{d}^2 r}{\mathrm{d}t^2} + m_e \gamma \frac{\mathrm{d}r}{\mathrm{d}t} + m_e \omega_0^2 r = -eE(t) \tag{11.5}$$

Note that γ is a damping rate. We could picture this damping as classical radiation damping of a moving charge, but a better picture would be the model of a solid, where each oscillator in the bulk is coupled to some sort of heat bath, through which it could loose some of its energy. The driven and damped oscillations of the electron cloud around the nucleus will lead to the formation of a local dipole moment. It must be pointed out that the driving electric field E is usually a local field, which comprises the applied electric field plus contributions from dipole–dipole interactions with all the other dipoles in the bulk. Using the ansatz $r(t) = r_0 \exp(i\omega t)$ one can easily

calculate the amplitude r_0 and the corresponding macroscopic polarization P (dipole moment per unit volume), assuming that there are N atoms per unit volume in the bulk:

$$P = -Ner = \frac{Ne^2}{m_e} \frac{1}{(\omega_0^2 - \omega^2 - i\gamma\omega)} E \tag{11.6}$$

The equations derived so far obviously describe the interaction of matter (electrons) with an external electromagnetic field. On the other hand macroscopic electrodynamics tells us that the corresponding dielectric displacement can be written as

$$D = \varepsilon_0 E + P \equiv \varepsilon_0 \varepsilon_r(\omega) E \equiv \varepsilon_0 (1 + \chi(\omega)) E \,, \tag{11.7}$$

where $\chi(\omega)$ is the (electric) susceptibility of the system.

Using these definitions we obtain the complex relative dielectric function of the Drude–Lorentz model:

$$\varepsilon_r(\omega) = 1 + \frac{Ne^2}{m_e \varepsilon_0} \frac{1}{(\omega_0^2 - \omega^2 - i\gamma\omega)} \tag{11.8}$$

The dielectric constant for a metallic system follows from Eq. (11.8) by assuming that $\omega_0 = 0$, which leads to

$$\varepsilon_r(\omega) = 1 - \frac{Ne^2}{m_e \varepsilon_0} \frac{1}{(\omega^2 + i\gamma\omega)} = 1 - \frac{\omega_p^2}{(\omega^2 + i\gamma\omega)} \,, \tag{11.9}$$

where $\omega_p = \sqrt{\frac{Ne^2}{m_e \varepsilon_0}}$ is the so-called plasma frequency.

The model described by Eqs. (11.8) and (11.9) can be further refined (and even parametrized) using quantum mechanical data [7], which makes it a useful qualitative and quantitative model for the optical properties of insulators and metals at least over certain interesting frequency ranges. Details of such an approach can be found in Ref. [7]. Furthermore we may assume that the electron cloud oscillates with different frequencies along different directions within the crystal, and in such a case the dielectric function actually becomes a dielectric tensor being diagonal in the main axis system of the crystal [7]. In Chapter 12 we will describe some proper *ab initio* quantum mechanical calculations of these general (tensorial) dielectric functions $\varepsilon_r(\omega)$. It will turn out that the resulting dielectric functions still contain many of the features of the analytical Drude–Lorentz model.

11.2.1.3 Derived Properties: Kramers–Kronig Relationships, Complex Refractive Index, Loss Function

Let us denote a general complex dielectric function as $\varepsilon_r = \varepsilon_1 + i\varepsilon_2$. There is the well-known relationship between the real part ε_1 and the imaginary part ε_2:

$$\varepsilon_1(\omega) - \varepsilon_0 = \frac{1}{\pi} P \int_{-\infty}^{\infty} d\omega' \frac{\varepsilon_2(\omega')}{\omega' - \omega} = \frac{2}{\pi} P \int_0^{\infty} d\omega' \frac{\omega' \varepsilon_2(\omega')}{\omega'^2 - \omega^2} \tag{11.10}$$

$$\varepsilon_2(\omega) = -\frac{1}{\pi} P \int_{-\infty}^{\infty} d\omega' \frac{\varepsilon_1(\omega')}{\omega' - \omega} = -\frac{2\omega}{\pi} P \int_0^{\infty} d\omega' \frac{\varepsilon_1(\omega') - \varepsilon_0}{\omega'^2 - \omega^2} \tag{11.11}$$

The symbol P refers to a Cauchy principal value integral. The reader unfamiliar with such integrals is referred to Ref. [3] for mathematical details, and for a number of carefully worked–out examples of such integrals.

The Kramers–Kronig relationships have a much more general validity than just relating the components of a complex dielectric function. The underlying mathematics with the necessary requirements of linearity, analyticity and causality is very well explained in Ref. [8], and a nice, but not uncritical historical account is given in Ref. [9]. The Kramers–Kronig relationships can also be of great value for numerical calculations, in particular when ε_2 is very similar to a form, where the Cauchy principal value integral is already known analytically. Then a useful estimate for ε_1 can be obtained from just applying Eq. (11.10), and complicated numerical calculations ε_1 must lead to similar results.

In a real experiment one usually measures the refractive index $n(\omega)$, or the optical absorption $\alpha(\omega)$ related to Beer's law. By introducing the extinction coefficient $\kappa(\omega) = \frac{c\alpha(\omega)}{2\omega}$ we can define the complex refractive index $N = n + i\kappa$, which is related to the complex dielectric constant $\varepsilon_r = \varepsilon_1 + i\varepsilon_2$ as follows:

$$\varepsilon_1 = n^2 - \kappa^2 \tag{11.12}$$

$$\varepsilon_2 = 2n\kappa \tag{11.13}$$

$$N = \sqrt{\varepsilon_r} \tag{11.14}$$

Again, the refractive index n and the extinction coefficient κ are related by a Kramers–Kronig relationship [8, 7]. The square roots of the complex numbers appearing in Eqs. (11.12 – 11.14) are special cases of de Moivre's formula [7]:

$$n = \sqrt{\frac{\varepsilon_1 + \sqrt{\varepsilon_1^2 + \varepsilon_2^2}}{2}} \tag{11.15}$$

$$\kappa = \frac{\varepsilon_2}{|\varepsilon_2|} \sqrt{\frac{-\varepsilon_1 + \sqrt{\varepsilon_1^2 + \varepsilon_2^2}}{2}} \tag{11.16}$$

It follows from the right hand side of Eq. (11.16) that κ and ε_2 must have the same sign.

The last derived property that we want to present in this section is the loss function. It is defined as follows [8]:

$$-\Im\left(\frac{1}{\varepsilon_r(\omega}\right) = \frac{\varepsilon_2}{\varepsilon_1^2 + \varepsilon_2^2} \tag{11.17}$$

As we will see in more detail below, peaks in the loss function correspond to longitudinal plasmon oscillations.

11.2.1.4 Example: Dielectric Properties from Reflectance Measurements

It will be instructive to see how complex dielectric functions can be extracted from optical experiments. The technique goes back to Philipp and Taft [10], and it is also described in Ref. [8].

Light at normal incidence to the smooth surface of a solid with complex dielectric constant N is reflected with a complex amplitude [11]

$$r = \frac{N-1}{N+1} = |r|e^{i\eta(\omega)} \tag{11.18}$$

This equation actually pre-supposes that no light will be able to pass the solid. Under these conditions, an experimentalist usually measures the reflected intensity

$$R(\omega) = |r|^2 = \frac{(n-1)^2 + \kappa^2}{(n+1)^2 + \kappa^2}\ , \tag{11.19}$$

but not the phase factor $\eta(\omega)$. However the related complex number $\ln(r) = \frac{1}{2}\ln(R) + i\eta$ gives rise to a Kramers–Kronig relationship, from which the phase factor η can be determined as follows [8]:

$$\eta(\omega) = -\frac{1}{2\pi} P \int_{-\infty}^{\infty} d\omega' \frac{\ln(R(\omega'))}{\omega' - \omega} \tag{11.20}$$

With the measurement of the reflectance R, and after the determination of the phase factor η, one can reconstruct the complex reflection amplitude r. The complex refractive index N then follows from:

$$N = \frac{1+r}{1-r} = n + i\kappa \tag{11.21}$$

Finally the dielectric properties ε_1 and ε_2 can be calculated using Eqs. (11.12 – 11.14).

11.2.2 Plasmons and Plasmonics

After familiarizing ourselves with a simple model for the basic dielectric properties of a material, we want to change our focus now on collective optical excitations of a solid called plasmons. For such a plasmon the whole electron gas of a solid can oscillate periodically around the skeleton of the ions, which gives rise to a number of interesting physical phenomena.

Furthermore it is possible to kick off evanescent surface waves called surface plasmon polaritons (SPPs), which lead to a new type of subwavelength optics, opening a possibility to bridge optics and electronics. We will also discuss absorption and scattering processes for metallic nanoparticles, which are also caused by plasmonic resonance effects. And as an example we will show calculated data for gold nanoparticles, based on a suitably parameterized Drude–Lorentz model.

A proper analysis or simulation of these phenomena requires the knowledge of fundamental properties of the electron gas and/or fundamental dielectric properties. This information can be supplied by experimental data, as explained in the previous section, or it could be provided by numerical data from *ab initio* calculations, as explained in Chapter 12.

11.2.2.1 Bulk Plasmons

In a solid a local surplus of electronic charge caused by fluctuations will be subject to a net repulsive force from the other electrons. The surplus electronic charge will then overshoot its original location, while being repelled by the electron cloud on the other side, which pushes the charge cloud back towards its original location, and so forth. This instability will lead to local oscillations of the electron gas.

Despite the resulting rapid charge density fluctuations of the electron gas, the overall charge density of the solid will be zero. The electrons that slosh around will give rise to a local electronic current $\boldsymbol{j}$, with a related continuity equation that involves the electronic charge density ϱ_e and the corresponding electric field $\boldsymbol{E}$:

$$\boldsymbol{\nabla} \cdot \boldsymbol{j} = -\frac{\partial \varrho_e}{\partial t} = -\varepsilon_0 \frac{\partial (\boldsymbol{\nabla} \cdot \boldsymbol{E})}{\partial t} \tag{11.22}$$

Assuming that there are N charge carriers per unit volume involved in this local electronic current $\boldsymbol{j}$, the current may be specified as

$$\boldsymbol{j} = -Ne\boldsymbol{v} \,, \tag{11.23}$$

where $\boldsymbol{v}$ is the velocity of the electrons in the current.

It is a standard exercise in electrodynamics to derive a general wave equation in the presence of such a current $\boldsymbol{j}$ [7]:

$$\frac{\partial \boldsymbol{j}}{\partial t} + \varepsilon_0 \frac{\partial^2 \boldsymbol{E}}{\partial t^2} = -\frac{1}{\mu_0} \boldsymbol{\nabla} \times (\boldsymbol{\nabla} \times \boldsymbol{E}) \tag{11.24}$$

We can further determine $\frac{\partial \boldsymbol{j}}{\partial t}$ by going back to Eq. (11.5), which leads to:

$$\frac{\partial \boldsymbol{j}}{\partial t} = -Ne \frac{\partial \boldsymbol{v}}{\partial t} = \frac{Ne^2 \boldsymbol{E}}{m_e} \tag{11.25}$$

Then we finally obtain the general plasmon equation

$$\omega_p^2 \boldsymbol{E} + \frac{\partial^2 \boldsymbol{E}}{\partial t^2} = -c^2 \boldsymbol{\nabla} \times (\boldsymbol{\nabla} \times \boldsymbol{E}) \,, \tag{11.26}$$

where ω_p is the plasma frequency of Eq. (11.9). As we are dealing with matter waves, one may assume that the electric field related to the plasmon oscillations has a longitudinal and transverse component $\boldsymbol{E} = \boldsymbol{E}_l + \boldsymbol{E}_t$, leading to two separate equations for longitudinal and transverse bulk plasmons.

For the longitudinal component $\boldsymbol{E}_l$ with $\boldsymbol{\nabla} \times \boldsymbol{E}_l = 0$ and $\boldsymbol{\nabla} \cdot \boldsymbol{E}_l \neq 0$ the resulting plasmon equation is:

$$\omega_p^2 \boldsymbol{E}_l + \frac{\partial^2 \boldsymbol{E}_l}{\partial t^2} = 0 \tag{11.27}$$

This is obviously the wave equation of a harmonic oscillator, and we can quantize the longitudinal oscillations accordingly [7]. A plane wave ansatz $\boldsymbol{E}_l = \boldsymbol{E}_0 \exp(i\boldsymbol{k} \cdot \boldsymbol{r} - i\omega t)$ for the oscillating electric field of the longitudinal plasmons shows that these oscillating modes are actually dispersionless (i.e. ω_p is independent of $\boldsymbol{k}$). This of course is an artefact of the many idealizations that we made to finally arrive at this equation. For example it will be much more realistic to include effective masses $m^*(\boldsymbol{k})$ and general permittivities $\varepsilon_r(\boldsymbol{k}, \omega)\varepsilon_0$ in the expression for ω_p, instead of using m_e and ε_0, see Ch. 12, Sec. 12.4.

We can actually derive some criteria for the appearance of longitudinal bulk plasmon oscillations, based on the theory developed up to now. Let us recall that for plasmon oscillations, the overall charge density of the bulk is zero on average, which according to Gauss' law implies that:

$$\boldsymbol{\nabla} \cdot \boldsymbol{D} = \boldsymbol{\nabla} \cdot (\varepsilon_r \varepsilon_0 \boldsymbol{E}) = 0 \tag{11.28}$$

For longitudinal plasmons with $\boldsymbol{\nabla} \cdot \boldsymbol{E}_l \neq 0$ this can only happen if $\varepsilon_r = 0$, and this criteria also remains valid for the most general types of relative

permittivities $\varepsilon_r(\boldsymbol{k},\omega)$. Furthermore (approximate) zeros in ε_r lead to peaks in the loss function $-\Im\left(\frac{1}{\varepsilon_r(\boldsymbol{k},\omega)}\right)$.

We can also give a physical meaning to this statement: a longitudinal plasmon oscillation cannot be directly excited by light, because the latter is a transverse electromagnetic wave. However particle beams like the electron beam in an electron microscope can knock–off plasmon oscillations, and the resulting plasmon resonances can be used for diagnostic purposes, which is a technique called electron energy loss spectroscopy (EELS). The probability $P(\boldsymbol{q},\omega)$ per unit time that a scattered electron transfers momentum $\boldsymbol{q}$ and energy $\hbar\omega$ to the electron gas is given by [11]:

$$P(\boldsymbol{q},\omega) = 2\pi\left(\frac{4\pi e^2}{q^2}\right)^2 S(\boldsymbol{q},\omega) = -\frac{8\pi e^2}{q^2}\Im\left(\frac{1}{\varepsilon(\boldsymbol{q},\omega)}\right) \tag{11.29}$$

Here $S(\boldsymbol{q},\omega)$ is the structure factor for the scattering of the incoming electron by the electron gas of the bulk solid. Consequently a peak in the loss function corresponds to a large probability of momentum and electron transfer by the incoming electrons, which is exactly what happens during a collective excitation of the electron gas.

Let us finally carry out a similar analysis for the transverse bulk plasmons $\boldsymbol{E}_t$ with $\boldsymbol{\nabla}\times\boldsymbol{E}_t \neq 0$ and $\boldsymbol{\nabla}\cdot\boldsymbol{E}_t = 0$. In this case Eq. (11.26) takes the form:

$$\omega_p^2\boldsymbol{E}_t + \frac{\partial^2\boldsymbol{E}_t}{\partial t^2} = -c^2\boldsymbol{\nabla}\times(\boldsymbol{\nabla}\times\boldsymbol{E}_t) \tag{11.30}$$

Using a plane wave ansatz $\boldsymbol{E}_t = \boldsymbol{E}_0\exp(i\boldsymbol{k}\cdot\boldsymbol{r} - i\omega t)$ we obtain the following dispersion relation:

$$c^2k^2 = \omega^2 - \omega_p^2 \tag{11.31}$$

There will be no plasmon oscillations for $\omega < \omega_p$. Furthermore as a result of the transverse nature of these plasmon oscillations $\boldsymbol{\nabla}\times\boldsymbol{E}_t = 0 = \boldsymbol{\nabla}\times((\varepsilon_r\varepsilon_0)^{-1}\boldsymbol{D})$, which implies that transverse plasmon modes correspond to poles $\varepsilon_r = \infty$ in the dielectric function $\varepsilon_r(\boldsymbol{k},\omega)$. Being transverse waves they can directly be excited by light.

11.2.2.2 Surface Plasmon Polaritons

Evanescent surface charge density waves can be generated at the interface between a regular dielectric with dielectric constant $\varepsilon_{r,d}(\omega)$, and a metal with dielectric constant $\varepsilon_{r,m}(\omega)$. In general, both dielectric constants describing the materials at the interface are tensors with complex entries. Standard cases are

interfaces between air and a homogeneous bulk metal, where the corresponding dielectric functions, and thus the general theoretical analysis, are largely simplified.

Surface charge density waves are strongly coupled photon–plasmon excitations described by quasiparticles called polaritons. For polaritons the strong interaction between the electromagnetic field and the polarizable matter is characterized by a dielectric constant $\varepsilon_r(\omega)$. From Maxwell's equations we then obtain a corresponding wave equation of the type:

$$\varepsilon_r(\omega)\frac{\partial^2 \boldsymbol{E}}{\partial t^2} = -c^2 \boldsymbol{\nabla} \times (\boldsymbol{\nabla} \times \boldsymbol{E}) \tag{11.32}$$

Using the standard plane wave ansatz $\boldsymbol{E}_t = \boldsymbol{E}_0 \exp(i\boldsymbol{k} \cdot \boldsymbol{r} - i\omega t)$ we derive a general polariton dispersion relation

$$c^2 k^2 = \varepsilon_r(\omega)\omega^2 \tag{11.33}$$

Let us now combine the general polariton concept with the concept of a surface wave, leading to evanescent surface waves called surface–plasmon polaritons (SPPs).

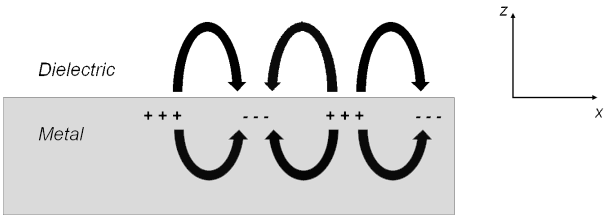

Fig. 11.2: Surface plasmon polariton wave at the interface between a dielectric and a metal. The electric field lines related to the surface charge density wave are indicated at both sides of the interface. The resulting evanescent surface wave is supposed to propagate in the x-direction, where it decays over time, and it will also decay into both materials along the z-direction. The corresponding magnetic fields have only components in the y-direction.

The general set-up is shown in Fig. 11.2. The SPP propagates into the positive x direction, where it will decay over time. It will also decay along the z-direction into both materials. Let us then assume that we can describe the light-matter interaction by a polariton dispersion relation on each side of the interface:

$$k_{x,i}^2 + k_{z,i}^2 = \varepsilon_{r,i}\left(\frac{\omega^2}{c^2}\right) \qquad i = d, m \tag{11.34}$$

Here d labels the dielectric side, and m labels the metallic side. Due to the evanescent character of the SPPs, we must assume that the components of $\boldsymbol{k}$ are complex within both media.

Furthermore we must apply the usual boundary conditions for general electromagnetic fields, which state that the tangential components of $\boldsymbol{E}$ and $\boldsymbol{H}$ and the normal components of $\boldsymbol{D}$ have to be continuous when crossing the interface at any point. This leads to following restrictions for the components of $\boldsymbol{k}$ [7]:

$$k_{x,d} = k_{x,m} = k_{\text{spp}} \qquad \frac{k_{z,d}}{\varepsilon_{r,d}} + \frac{k_{z,m}}{\varepsilon_{r,m}} = 0 \tag{11.35}$$

We can use these restrictions to eliminate the z-components in Eq. (11.34), and then we obtain the important dispersion relation for the propagation of SPPs in the x-direction:

$$k_{\text{spp}} = k_{\text{spp},1} + ik_{\text{spp},2} = \frac{\omega}{c}\sqrt{\left(\frac{\varepsilon_{r,d}\varepsilon_{r,m}}{\varepsilon_{r,d}+\varepsilon_{r,m}}\right)} = k_0\sqrt{\varepsilon_{\text{eff}}(\omega)} \tag{11.36}$$

Note that k_0 denotes the scalar wave vector of an electromagnetic wave in vacuum.

There is a lot of important physics hidden behind this equation. Although a general analysis will much more involved due to the appearance of the square root of a complex number, let us assume that the imaginary part of the dielectric function on the dielectric side $\varepsilon_{2,d}$ is zero. Furthermore let us assume that the real part on the metal side $\varepsilon_{1,m}$ is negative, and that the imaginary part $\varepsilon_{2,m}$ is very small. Then we can expand the square root in Eq. (11.36) to obtain:

$$\begin{aligned} k_{\text{spp}} &= k_{\text{spp},1} + ik_{\text{spp},2} \\ &= k_0\sqrt{\left(\frac{\varepsilon_{1,d}\varepsilon_{1,m}}{\varepsilon_{1,d}+\varepsilon_{1,m}}\right)} + i\frac{k_0}{2}\left(\frac{\varepsilon_{1,d}\varepsilon_{1,m}}{\varepsilon_{1,d}+\varepsilon_{1,m}}\right)^{3/2}\frac{\varepsilon_{2,m}}{\varepsilon_{1,m}^2} + \dots \end{aligned} \tag{11.37}$$

Obviously there can be no real $k_{\text{spp},1}$ (and thus a propagating surface wave!) unless $\varepsilon_{1,m} < -\varepsilon_{1,d}$. But then $k_{\text{spp},1} > k_0$, which means that the SPP for a given frequency ω has a smaller wavelength than the corresponding electromagnetic wave in vacuum, and therefore the SPP needs an extra momentum to be kicked off.

We can also define a propagation length $\delta_{\text{spp}} = \frac{1}{2k_{\text{spp},2}}$, which can reach up to 1 mm for the coupling of infrared light with wavelength 1.5 μm into a silver/vacuum interface [12]. By plugging our expressions for k_{spp} back into Eq. (11.34), we can analyse the propagation of SPPs along the z-direction, and it predicts decaying behaviour away from the interface [7].

From a practical point of view SPPs cannot be directly excited by light, due to their evanescent character. In fact the incoming light has to be coupled into an SPP using a prism or a surface grating, because extra momentum is necessary to kick off an SPP [12]. Once the SPPs have been excited, they give rise to an interesting type of surface optics: due to their subwavelength character the SPPs are actually forming the basis of a new branch of optical technology called plasmonics, which bridges the fields of optics and electronics [13, 14, 12].

11.2.2.3 Localized Plasmons

The third type of plasmonic phenomena that we want to discuss in this Section are localized plasmons (LPs), or localized surface plasmon resonances (LSPRs), to be more specific. localized plasmons or localized surface plasmon resonances (LPs/LSPRs) are caused by the interaction of light with metallic nanoparticles. In particular the interaction of light with irregularly shaped metallic nanoparticles can be quite complicated [2], and a numerical solution of this problem generally requires the use of finite difference time domain method (FDTD) methods, which are explained in Chapter 12.

What one generally observes in an optical experiment on metal nanoparticles is an enhancement of the field intensity around these metallic nanoparticles, which is caused by the formation of localized plasmonic surface waves. These field enhancements can be quite substantial, and the frequency ranges for the corresponding plasmonic resonances are strongly dependent on the size, the shape and the dielectric properties of the surrounding medium. This leads to a number of interesting practical applications [12].

In this Section we will only focus on spherical nanoparticles. Let us assume a simplified situation like in Fig. 11.3, where we see a spherical metallic particle with radius R and relative dielectric function $\varepsilon_{r,m}$, which is embedded into a surrounding dielectric material with relative dielectric function $\varepsilon_{r,d}$.

The system is excited by a constant electric field $\boldsymbol{E}$, which induces a dipole moment $\boldsymbol{p} = \alpha \boldsymbol{E}$ in the nanosphere. It is one of the standard exercises of electrodynamics to show that this system is equivalent to a point dipole $\boldsymbol{p}$ at the centre of the spherical nanoparticle, and with the following polarizability [3]:

$$\alpha = \frac{4\pi R^3}{3} \frac{\varepsilon_{r,m} - \varepsilon_{r,d}}{\varepsilon_{r,m} + 2\varepsilon_{r,d}} \tag{11.38}$$

In order to quantify the plasmonic field enhancements by such a particle, one can extend the simple dipole picture to the standard scattering scenario of incoming light with frequency ω and wave vector $\boldsymbol{k}$ being scattered by a point

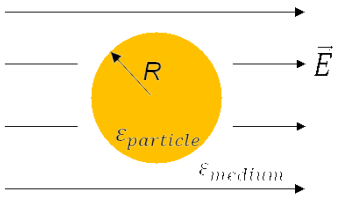

Fig. 11.3: A spherical metallic nanoparticle of radius R and with dielectric constant $\varepsilon_{\text{particle}}$ is embedded in a surrounding medium with dielectric constant $\varepsilon_{\text{medium}}$. Furthermore the particle is excited by a constant electric field $\boldsymbol{E}$, which induces a dipole moment within the nanoparticle.

dipole. The scattering process can be summarized as *extinction = scattering + absorption + luminescence*, which in terms of cross sections reads as follows:

$$\sigma_{\text{ext}} = \sigma_{\text{scatt}} + \sigma_{\text{abs}} + \sigma_{\text{lum}} \tag{11.39}$$

It is a non-trivial exercise to actually obtain analytical expression for these cross sections [2, 12]. Leaving luminescence effects aside one can just concentrate on scattering and absorption processes [12]:

$$\sigma_{\text{scatt}} = \frac{8\pi}{3} k^4 R^6 \left| \frac{\varepsilon_{r,m} - \varepsilon_{r,d}}{\varepsilon_{r,m} + 2\varepsilon_{r,d}} \right|^2 \tag{11.40}$$

$$\sigma_{\text{abs}} = 4\pi k R^3 \Im \left(\frac{\varepsilon_{r,m} - \varepsilon_{r,d}}{\varepsilon_{r,m} + 2\varepsilon_{r,d}} \right) \tag{11.41}$$

For the proper range of validity of these expressions with respect to the optical theorem see [2]. But as approximate as this approach may be, we can already clearly see a general trend from these two equations: For particles with a large radius R, Eqs. (11.40) and (11.41) tell us that scattering will largely dominate over absorption. For particles with small radius R we expect that absorption will largely dominate over scattering.

There are ways to extend the model presented in this Section to more general cases, e.g. elliptic particles of different shapes [2]. For more irregular shapes and coupled systems it is better to actually calculate the cross sections from the components of the Poynting vector, based on FDTD methods described in Chapter 12.

11.2.3 Example: Gold Nanoparticles

We have already guessed from Eqs. (11.40) and (11.41) that for particles with small radius R:

$$\sigma_{\text{abs}} \sim R^3 >> \sigma_{\text{scatt}} \sim R^6 \tag{11.42}$$

For particles with large radius R it should be exactly the other way round.

Furthermore both cross sections depend on the frequency ω of the incoming light through k, through the relative dielectric function $\varepsilon_{r,m}(\omega)$ of the metallic nanoparticle, and also through the relative dielectric function $\varepsilon_{r,d}(\omega)$ of the surrounding medium. Given the resonant character of the Drude-like dielectric functions discussed in Sec. 11.2.1 we would therefore expect peaks in the absorption and scattering cross sections within certain frequency ranges. Fig 11.4 shows the scattering and absorption cross sections for light scattering by gold nanoparticles embedded in air. A parametrized Drude–Lorentz model $\varepsilon_{r,m}$ is used for gold, which contains an additional term describing interband transitions.

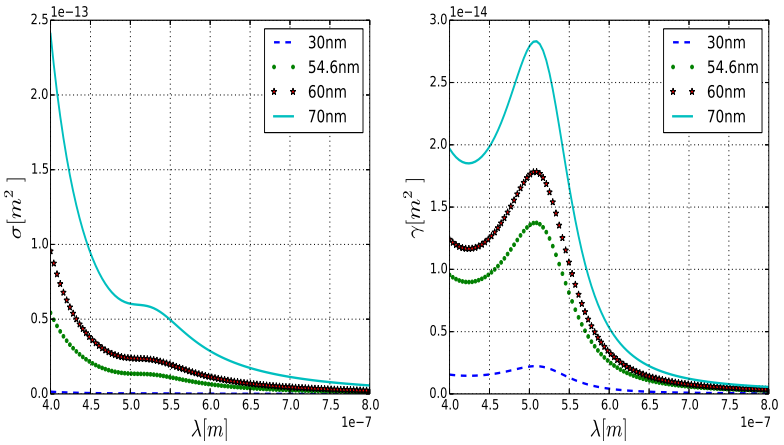

(a) (b)

Fig. 11.4: Scattering and absorption cross sections as a function of the frequency ω of scattered light for a series of gold particles of various sizes embedded in air.

We clearly observe the expected resonance effects within certain frequency ranges, where light of a certain frequency ω will be strongly absorbed or scattered by the gold nanoparticle. We also see that some of the cross sections

can largely surpass the geometrical cross sections of the particles, which is indicative of the field enhancements around the plasmonic nanoparticles during resonance. And the numerical data confirms the predicted trend, that small particles absorb and large particles scatter.

The domestic tool to generate these plots was written in Python, and it is available from the authors. One should expect to see similar trends when using *ab initio* dielectric functions, which may be generated by the methods described in Chapter 12.

11.3 Applications in Photovoltaics

It has been realized in recent years that the Shockley–Queisser limit for single-junction solar cell efficiencies [15] is more of a design problem than a real fundamental limit [16]. In particular when it comes to cheap and robust augmentations of standard organic and inorganic solar cells, the light trapping and light scattering properties of plasmonic nanoparticles could play a very important rule [17]. Plasmon enhanced solar cells should allow for efficiencies similar to multi-junction and concentrator technologies [16], but based on a much simpler design, and at a fraction of their productions costs. In order to achieve high efficiencies, it will be necessary to understand in detail the complicated interactions between free charge carriers or bound electron-hole pairs (excitons) and the localized plasmons in metallic nanoparticles, where computational methods will play a very important role. In the following we will discuss some of these novel approaches to increase the efficiency of standard solar cells, and hopefully we will stimulate some interest among our readers to tackle some of these design problems themselves, using the theoretical and numerical methods presented in Chapter 12.1 .

Let us point out in this context that for us (and many other researchers), solar cell design does not necessarily consist of beating world records in solar cell efficiency. An equally important goal is the development of cheap and reliable solar cell technologies for the benefit of the most disadvantaged members of our society, who are often disconnected from the main power grid, but urgently need stand–alone solutions to produce their own energy.

Research to develop useful photovoltaic devices for off-grid rural communities requires the sort of technological compromises, where computation tools play a very important role. Here a very crucial step is to get at least a rough idea about the underlying physical processes, or just an overview over a plethora of potential materials and technologies. As a practical example that falls under this particular category, we will present a numerical study of heat generation

by arrays of spherical plasmonic nanoparticles, which is one of the basic design problems for cheap and efficient plasmon enhanced solar cells.

11.3.1 Solar Cell Design

Solar energy is the most abundant source of energy available, and it is usually harnessed in terms of electricity, fuels and heat [18]. At the moment solar energy only makes up for a tiny fraction of the total energy production worldwide, but with the long term prospect of very limited resources of fossil fuels, research on photovoltaics and on other solar technologies is certainly a good investment into a sustainable future.

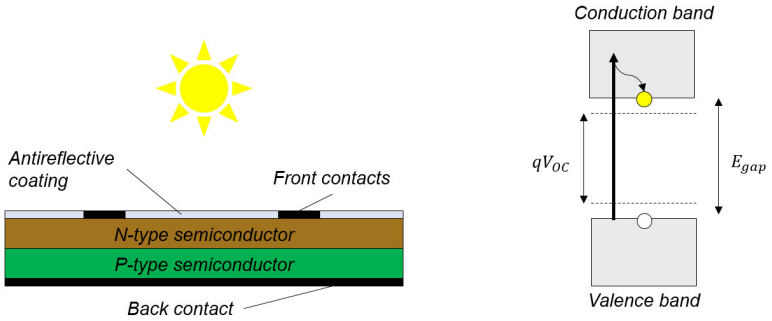

Fig. 11.5: Left: Anatomy of a typical solar cell. The basic layout is that of a p-n junction. Right: Light absorption in a solar cell. Photons with energy larger than the band gap E_{gap} create a electron–hole pair, but the electron will have lost part of its energy due to thermalization. Note that the much smaller separation between the real electron and hole Fermi levels qV_{OC} is caused by entropic effects, see [16].

The key technologies of photovoltaics are solar cells made of monocrystalline and polycrystalline silicon [19]. They are basically p-n junctions between p-doped and n-doped silicon. As in all p-n junctions a depletion layer will form around the interface between the two doped layers, leading to a strong electric field across this depletion layer. An incoming photon will directly create free charge carriers (i.e. electrons and holes), or it may form a loosely bound electron–hole pair called exciton within the active material(s) of the solar cell device. Excitons may diffuse towards the depletion layer, where the strong electric fields will separate them into an electron and a hole.

The n-layer will allow for the easy passage of electrons but not for holes, whereas the p-layer will allow for the easy passage of holes but not for electrons. So rather than annihilating each other, electrons and holes will migrate to separate contacts at the front and at the back of the solar cell, where they create a potential difference V_{OC} (the so-called open–circuit voltage), which is similar to the band gap of the active semiconductor layer. In a closed circuit attached to the contacts current will start to flow, and the cell will act as an electrical power source. In Fig. 11.5 we show the anatomy of a typical commercial solar cell.

For such a standard solar cell, one can expect an efficiency of about 18% [19]. The theoretical limit for the efficiency of a standard single junction cell without concentrated illumination was predicted to be around 31% [15]. The main problems leading to low efficiency are indicated in Fig. 11.5. Photons with energies larger than the band gap E_{gap} will create hot electrons, which loose a serious fraction of their energy due to thermalization. This problem is largely avoided in multi–junction cells, but they are very expensive and difficult to fabricate.

Furthermore there are a number of entropic effects that reduce the open circuit voltage V_{OC} to a value smaller than E_{gap}/q, where q is the charge of the carrier. As discussed in [16], one can in principle bring the efficiency up to 50–70% by using light–trapping technologies and surface light directors, both of which can be produced using standard nanofabrication technologies. Some of these light trapping strategies are nicely described in [20], where many of the numerical techniques described in this Chapter as well as in Chapter 12 are applied to show how to find the most promising technological solutions. Another big problem is the passage of photons with energies smaller than E_{gap}. These photons will not be able to create free charge carriers within the active layer of the solar cell. Therefore a considerable part of the solar spectrum cannot be used by a conventional solar cell. However as originally suggested in [21], one could use up- and down-conversion to harvest these "lost" photons.

For down-conversion an additional conversion layer has to be put on top of a standard solar cell, where high energetic photons will be transformed into two lower-energetic photons, whose energies are close to the band gap energy. For up-conversion a conversion layer together with a reflector are attached to the bottom of the cell, where two low-energetic photons passing the solar cell will generate a higher energetic photon, whose energy will be close to the band gap energy. For a survey of recent progress in up- and down-conversion for solar cell technologies see [22].

11.3.2 Plasmon Enhanced Solar Cells

The various strategies to improve the efficiency of conventional solar cells may profit considerably from the application of plasmonic technologies. This has been pointed out in two recent review articles [17, 23].

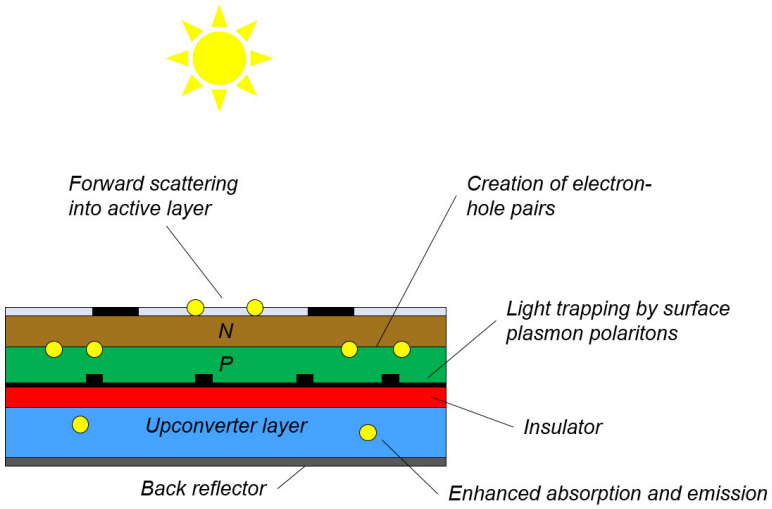

Fig. 11.6: Plasmon enhanced solar cell that shows several of the advanced plasmonics features discussed in [17]: (i) Metal nanoparticles at the surface of the cell collect photons, trap photons and scatter photons into the active layer. (ii) Metal nanoparticles in the active layer generate a larger number of electron–hole pairs via strong plasmon–exction coupling. (iii) Light trapping and guiding at metal–semiconductor interfaces. (iv) Enhanced up-conversion within the upconverter layer, due to the presence of metallic nanoparticles.

The essence of these new approaches is summarized in Fig. 11.6. Each of these suggestions will provide a fascinating playground for the computational methods described in Chapter 12. The expected improvements in solar cell efficiency are based on the light trapping, scattering and field enhancement properties of plasmons, as discussed in Sec. 11.2.2.

The first improvement in efficiency based on plasmonic nanoparticles would happen at the top of the solar cell. Here the nanoparticles are supposed to be partially embedded in a medium with larger permittivity ε_r below the interface. With their large scattering cross sections (in particular close to resonance), the nanoparticles will harness a lot of the incoming photons, and

preferentially scatter them into the dielectric with the larger relative permittivity ε_r. The latter is the active layer of the solar cell, where these photons will be converted into electron–hole pairs, thus increasing the efficiency of the solar cell.

The second improvement would come from the embedding of metallic nanoparticles within the active layer itself. There is some evidence that the enhanced electromagnetic field around the nanoparticles will also enhance the formation of excitons, which would again add to the efficiency of the solar cell, see Sec. 11.4 below. The fundamental mechanisms of this plasmon–exciton coupling are largely unexplored [17].

The third improvement would come form the fabrication of patterned backside contacts, which lead to the coupling of light into surface plasmon polaritons at the metal–semiconductor interface, provided one can equip the contacts with some grating structures in order to let the photons couple into the SPP modes. These plasmonic interfaces might also act as a traps for long–wavelength photons, which would usually pass through the cell without being harnessed.

Finally the fourth improvement would come from the embedding of metal nanoparticles into an upconverter layer at the back of the solar cell. Here the emission and also the excitation processes during up-conversion can be enhanced through plasmonic coupling. The details of this coupling are not fully understood, see Sec. 11.4 below. But it seems that the plasmonic nanoparticles actually enhance both, the absorption as well as the emission strength [22].

Each of these four improvements will offer new challenges and possibilities for the computational methods discussed in Chapter 12.1. The goal is to find the optimum shape, location and material for the plasmonic features described above. Furthermore a fundamental theory of plasmon enhanced solar cells will also require the combination of the standard computation methods described in Chapter 12.1 with other computational methods used to describe particle-hole and up-/down-conversion processes, in order to get some deeper insight into the coupling between these various processes.

11.3.3 Example: Heating of Plasmonic Layers

Despite the fact that light trapping by plasmonic nanoparticles might have many beneficial effects for the photon conversion efficiency of solar cells, it must also be pointed out that the local heating of the active layers by embedded plasmonic nanoparticles can actually lead to a largely reduced performance of such devices. It is therefore important to predict and analyse the heat generation for a given solar cell prototype.

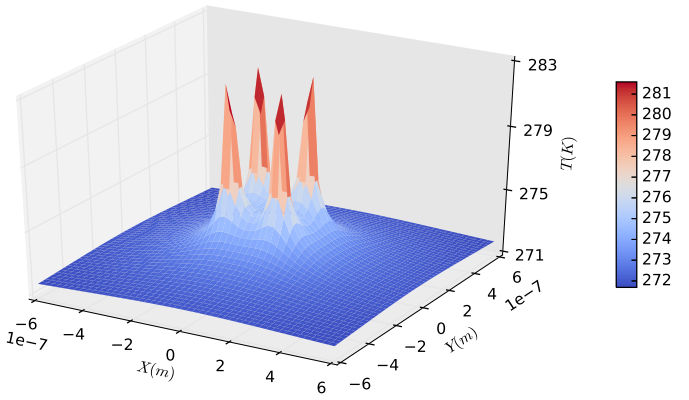

Fig. 11.7: Lateral temperature map for an array of 16 gold nanoparticles.

Heating by plasmonic nanoparticles is a phenomena that has already been studied for some time, because it leads to important applications in medicine [24]. Apart from their usage as diagnostic tools, plasmonic nanoparticles also play an important role in thermotherapy. After successfully attaching plasmonic nanoparticles to cancer cells, one can irradiate the tumor with light. Due to the resulting heating of the nanoparticles, one can kill the cancer cells without damaging the surrounding tissue [12]. There is a huge and established literature that deals with this processes [12, 25], and therefore we can fall back on this knowledge in order to simulate heating by plasmonic nanoparticles embedded in solar cells.

First of all we need a proper description of how incoming light of frequency ω will be turned into heat. This process can be quantified by the power of heat generation $Q(\omega)$ (in W), which is related to the absorption cross section $\sigma_{\text{abs}}(\omega)$ (in m^2) and the irradiance $I(\omega)$ (in W/m^2) of the incoming light:

$$Q(\omega) = \sigma_{\text{abs}}(\omega) I(\omega) \sim \sigma_{\text{abs}} E_{\text{loc}}^2 \tag{11.43}$$

The proportionality sign on the right side of this equation should remind us, that the heating of the nanoparticles is caused by the local field, which is the field of the incoming radiation plus the field due to dipole–dipole interactions with other nanoparticles. The correct way to calculate this local field is worked–out in [8].

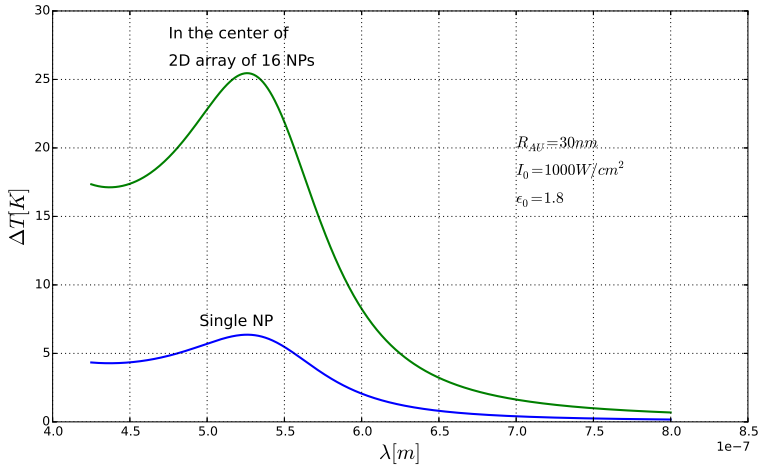

Fig. 11.8: Temperature difference as a function of incoming wavelength for a single gold nanoparticle, and for an array of gold nanoparticles. Local field effects have not been taken into account.

In order to calculate the absorption cross sections in Eq. (11.43), we can either use FDTD methods described in Chapter 12 , or we can use the expressions in Eqs. (11.40) and (11.41), either based on *ab initio* dielectric functions, or based on parameterized Drude–Lorentz models . Physically speaking Q describes the power generated within each nanoparticle, which will lead to a heating of that nanoparticle. Mathematically speaking Q gives rise to a source term in the heat transfer equation, which can be solved analytically for spherical particles with radius R. This leads to the following radial temperature profile outside the spherical nanoparticles [25]:

$$T(r,\omega) = T_0(\omega)\frac{R}{r} = \frac{Q(\omega)}{4\pi R\kappa_{\text{med}}}\frac{R}{r} \tag{11.44}$$

where κ_{med} is the thermal conductivity of the surrounding medium. For an ensemble of spheres, it actually makes sense to work out a temperature profile by adding up all the contributions from the different spheres, and implement their thermal coupling over the local field in Eq. (11.43).

The results of such a simulation are shown in Figs. 11.7 – 11.8. Again a domestic Python based tool was used, where the dielectric data for gold nanoparticles was calculated using a Drude–Lorentz model. The resulting heating effects for an array of 16 nanoparticles are comparable to previous studies in the field [26]. The tool can also deal with local field effects (usually resulting in red shifts of the resonance frequencies), and with random arrangements of

spherical nanoparticles of different sizes. Those are all typical scenarios, which might also be encountered in real plasmon enhanced solar cells.

11.4 New Research Directions

The development of theoretical concepts and computational methods in materials science is always driven by interesting new applications. In this section we will present some interesting new directions within the field plasmonics, which are the subject of intense current research. We will look at research about the interactions of plasmons with other types of electronic excitations and transition processes, like excitons and up/down-conversion processes.

11.4.1 Plasmonic Resonances in Non-Metallic Nanostructures

localized surface plasmon resonances are usually associated with metallic nanoparticles, see Sec. 11.2.2. However starting with the rather surprising measurement of plasmonic resonances for nanoparticles of the semiconductor $Cu_{2-x}S$ [27], a whole series of nanocrystalline systems have been discovered up to date, which show a similar optical behaviour [28]. Therefore it has been gradually realized, that LSPRs might not be a specific optical feature of metallic nanoparticles.

The LSPRs in semiconductor nanocrystals have a number of very distinct properties, which are nicely summarized in a recent review article [28]: The LSPRs can be excited based on just a handful of free charge carriers per nanoparticle. This is quite different from metallic nanoparticles. It makes these systems very sensitive to electron or hole transfer reactions, unlike metallic plasmonic nanoparticles. Furthermore the peak of the plasmon resonances can be shifted by manipulating the carrier densities, something that is not possible for metallic nanoparticles.

Sophisticated theoretical approaches as well as numerical simulations will be needed to fully understand the physics behind these phenomena. Together with progress being made on the experimental side, the surprising properties of these new types of plasmonic nanostructures could then be used for optical sensors and switches.

11.4.2 Interactions of Plasmons With Other Electronic Transition Processes

In Sec. 11.3 we described the use of plasmonic nanoparticles to enhance the efficiency of solar cells [17]. Furthermore we have pointed out the possibility of extending the spectral range of conventional inorganic and organic solar cells using up- and down-conversion [21].

A high efficiency for a conventional solar cell requires the absorption of most incoming photons, followed by a proper charge separation of electrons and holes before they actually recombine. For organic solar cells this process also involves the formation of bound electron-hole pairs called excitons [11]. The question is how the presence of plasmonic nanoparticles might influence the rate of exciton creation, the exciton diffusion length, and ultimately the lifetime of these excitons.

A strong coupling between surface plasmons and excitons has been observed in experimental studies (e.g. see [29]). Theoretical studies of the same phenomena have been made as well [30]. Furthermore studies of the related photon conversions processes have been carried out in Ref. [31]. One explanation for the reported interactions between excitons and plasmons may be the coupling of a single mode to a continuum, which should give rise to a (nonlinear) Fano effect [32].

A related topic are coherently coupled excitons and plasmons, forming a new type of quasiparticle called plexciton [33]. The basic processes of this coupling between excitons and plasmons are still not fully understood, and progress could be made by a proper multi-scale computational approach, based on the tools described in Chapter 12 .

Furthermore up- and down-conversion processes are mediated by electronic transitions within rare earth ions. These are mostly transitions between atomic states (in a crystal field), which are usually well separated from the surrounding bulk. The rate w at which these processes take place are strongly influenced by the photon flux Φ, according to the well-known relation:

$$w = \sigma_{\mathrm{lum}}(\Phi)\,\Phi \tag{11.45}$$

Here σ_{lum} is the luminescence cross section, see Eq. (11.39), which is supposed to be flux dependent for a typical two-photon process. It can be expected that the modification of local photon fluxes by an enhanced electromagnetic field around plasmonic nanoparticles will be very useful to increase the basic conversion rates, and indeed a thorough description of this effect can be found in Ref. [34].

11.5 Concluding Remarks

We gave a brief survey of light-matter interactions based on the Drude–Lorentz model. We used this approach to describe the basic properties of bulk plasmons, surface plasmons and localized plasmons. We also described recent efforts to enhance the efficiency of solar cells, based on the implementation of plasmonic nanoparticles and plasmonic nanostructures in the active layers of such a device. And we pointed out a number of interesting optical phenomena, which are caused by complex interactions between plasmons and other optical excitations. These phenomena not fully understood up to now.

In order to gain a much deeper understanding of the various plasmonic phenomena and their applications presented in this Chapter, it will be necessary to go beyond analytical models and the simplest model dielectric functions based on the Drude–Lorentz model. In Chapter 12 we will have a look at some of the major computational methods used to model and analyse the various plasmonic phenomena. We will then see how the basic dielectric properties of a given material may be calculated *ab initio*, i.e. from first principles. In Chapter 12 we will also present ways to combine *ab initio* methods with a proper electrodynamical modelling of non-idealized plasmonic nanostructures and plasmonic nano-particles.

Acknowledgements

The authors would like to thank the National Institute for Theoretical Physics (NITheP), the Mandelstam Institute for Theoretical Physics (MITP), the Materials Physics Research Institute (MPRI) and the DST-NRF Centre of Excellence in Strong Materials (CoE-SM) for support. We also acknowledge additional support through a bilateral project *Plasmonics for a better efficiency of solar cells* between South Africa and Italy (contributo del Ministero degli Affari Esteri e della Cooperazione Internazionale, Direzione Generale per la Promozione del Sistema Paese). Finally we would like to thank our colleague and collaborator Tahir Aslan (Wits) for providing us with Figs. 11.4, 11.7 and 11.8.

References

1. H.C. Van de Hulst, *Light Scattering by Small Particles* (Dover Publications, Mineola, 1981)

2. C.F. Bohren, D.R. Huffman, E.E. Clothiaux, *Absorption and Scattering of Light by Small Particles* (Wiley-VCH, Weinheim, Berlin, 2016)
3. H.J.W. Müller-Kirsten, *Electrodynamics: An Introduction Including Quantum Effects* (Wiley-VCH, Weinheim, Berlin, 2004)
4. A.P. Sutton, *Electronic Structure of Materials* (Clarendon Press, Oxford, 1993)
5. M.Z. Hasan, C.L. Kane, Rev. Mod. Phys. **82**, 3045 (2010)
6. C. Cohen-Tannoudji, B. Diu, F. Laloe, *Quantum Mechanics* (John Wiley and Sons, Hoboken, 1977)
7. M. Fox, *Optical Properties of Solids* (Oxford University Press, Oxford, 2010)
8. G.E. Mahan, *Condensed Matter in a Nutshell* (Princeton University Press, Princeton, 2011)
9. C.F. Bohren, European Journal of Physics **31**(3), 573 (2010)
10. H.R. Philipp, E.A. Taft, Physical Review **120**, 37 (1960)
11. C. Kittel, *Quantum Theory of Solids*, 2nd edn. (John Wiley and Sons, New York, 1987)
12. L. Novotny, B. Hecht, *Principles of nano-optics* (Cambridge University Press, Cambridge, 2012)
13. S.A. Maier, H.A. Atwater, Journal of Applied Physics **98**(1), 011101 (2005)
14. S.A. Maier, M.L. Brongersma, P.G. Kik, S. Meltzer, A.A.G. Requicha, H.A. Atwater, Advanced Materials **13**(19), 1501 (2001)
15. W. Shockley, H.J. Queisser, Journal of Applied Physics **32**(3), 510 (1961)
16. A. Polman, H.A. Atwater, Nature materials **11**, 174 (2012)
17. H. Atwater, A. Polman, Nature Materials **9**, 205 (2010)
18. G.W. Crabtree, N.S. Lewis, Physics Today **60**(3), 37 (2007)
19. T. Saga, Nature Asia Materials **2**, 96 (2010)
20. J.E. Fonash, *Introduction to Light Trapping in Solar Cell and Photo-detector Devices* (Adademic Press, Amsterdam, 2015)
21. T. Trupke, M.A. Green, P. Würfel, Journal of Applied Physics **92**(7), 4117 (2002)
22. W. van Sark, J. de Wild, J. Rath, A. Meijerink, R.E. Schropp, Nanoscale Research Letters **8**(1), 81 (2013)
23. J. Schuller, E. Barnard, W. Cai, Y.C. Jun, J. White, M. Brongersma, Nature Materials **9**, 193 (2010)
24. P.K. Jain, X. Huang, I.H. El-Sayed, M.A. El-Sayed, Plasmonics **2**(3), 107 (2007)
25. A.O. Govorov, W. Zhang, T. Skeini, H. Richardson, J. Lee, N.A. Kotov, Nanoscale Research Letters **1**, 84 (2006)
26. A.O. Govorov, H.H. Richard, Nano Today **2**, 30 (2007)
27. Y. Zhao, H. Pan, Y. Lou, X. Qiu, J. Zhu, C. Burda, Journal of the American Chemical Society **131**(12), 4253 (2009). PMID: 19267472
28. J. Faucheaux, A. Stanton, P. Jain, The Journal of Physical Chemistry Letters **5**(6), 976 (2014). PMID: 26270976
29. J. Bellessa, C. Bonnand, J.C. Plenet, J. Mugnier, Phys. Rev. Lett. **93**, 036404 (2004)
30. I.V. Bondarev, L.M. Woods, K. Tatur, Phys. Rev. B **80**(8), 085407 (2009)
31. Y. Fedutik, V.V. Temnov, O. Schöps, U. Woggon, M.V. Artemyev, Phys. Rev. Lett. **99**, 136802 (2007)
32. W. Zhang, A.O. Govorov, G.W. Bryant, Phys. Rev. Lett. **97**, 146804 (2006)
33. N. Fofang, N. Grady, Z. Fan, A. Govorov, N. Halas, Nano Letters **11**(4), 1556 (2011). PMID: 21417362
34. V. Rivera, Y. Ledemi, S. Osario, D. Manzani, F. Ferri, R.S. J.L., N. L.A.O., E. Marega Jr., Journal of Non-Crystalline Solids **378**, 126 (2013)

Index

Appendix E. Computational Plasmonics: Numerical Techniques

In this appendix, we include the work co-authored by Robert Warmbier and Alex Quandt. It is cited in ref. [5]. The content of the chapter is summarized in the sections of chapter 4.

12

Computational Plasmonics: Numerical Techniques

F. Mohammed, R. Warmbier, and A. Quandt

[1] School of Physics, Centre of Excellence in Strong Materials, University of the Witwatersrand, Wits 2050, Johannesburg, South Africa
[2] Materials for Energy Research Group (MERG), University of the Witwatersrand, Wits 2050, Johannesburg, South Africa faris.aims.ac.za
[3] Centro studi e ricerche Enrico Fermi, Piazza del Viminale, 00184 Roma, Italy

Abstract. This is the second Chapter in which we give a detailed introduction into the field of computational plasmonics. While Chapter 11 covered the theoretical background of modern plasmonics, this Chapter provides describtions of the the numerical methods involved in computational plasmonics. To this end we use modern *ab initio* methods, the standard frequency-domain and time-domain methods of computational electromagnetics. Finally we show some applications in the fields of photovoltaics and plasmonic–photonic crystals and close with a discussion of open problems.

12.1 Introduction

The Physics of real systems requires the solution of very complex basic equations where analytical solutions do not exist. From this follows the need for accurate numerical solutions. Numerical methods have played a major role in the development of all applied sciences, and not only of Physics. Alongside the development of powerful computers it was also the development of new algorithms that allowed us to tackle very complex tasks efficiently, and with very high accuracy [1].

For systems that are described by partial differential equations, such as electronic (Schrödinger equation) and photonic (wave equation derived from Maxwell's equations) systems, different techniques have been developed to

solve these equations for a given system, and to make accurate predictions about their properties. In the following Sections we will describe some of the most popular numerical techniques used to simulate plasmonic systems on various lengthscales and timescales.

We will start with mesoscopic/macroscopic optical systems. The numerical simulation of such systems is based on wave equations, which can be derived from Maxwell's equations. Knowing the properties of the basic materials in terms of their relative permittivities and permeabilities, one can make very precise predictions even for relatively complex systems, because the underlying equations are mostly linear. The most popular numerical techniques are the finite-difference time-domain method [2], spectral methods [3], block iterative methods [4] and block-pseudospectral methods [5], just to name a few. We will limit our discussion to only two methods, which are the frequency domain method (FD) described in Sec. 12.2, and the finite-difference time-domain (FDTD) method described in Sec. 12.3.

Permeabilities and permittivities have their origin in light-matter interactions at the atomic level (i.e. nanoscale). If we want to make accurate predictions about plasmonic systems on the nanoscale, then we cannot use simple models any more, like the Drude–Lorentz model described in Sec. 11.2. We have to solve the many-body Schrödinger equation for a bulk system excited by electromagnetic radiation. Although this equation can be written down quite easily, it is well–known in quantum mechanics that it will not have analytical solutions for even the most simple nanosystems. Numerical solutions are a formidable challenge as well, due to the non-linear nature of the effective one-particle equations derived from the many-body Schrödinger equation. We will limit our discussion to density functional theory (DFT) [6, 7] described in Sec. 12.4.

In this Chapter we will have a look at some of the major computational methods used to model and analyse the various plasmonic phenomena. Based on the assumption that we somehow dispose of a sufficiently precise dielectric function, we will first discuss the standard frequency and time domain methods of computational plasmonics and their practical applications. Then we will go into the details of determining the dielectric function *ab initio* (i.e. from first principles) using (time-dependent) DFT.

In Sec. 12.5 we will present the development of the numerical techniques required to understand the physics of plasmonic photonic crystals, where one tries to control the flow of surface plasmon polaritons using photonic superstructures. We will show how to model the corresponding photonic band structures, and also motivate for more extended studies of disordered or aperiodic photonic systems.

Finally in Sec. 12.6 we will give a short summary and discuss a number of open questions. First we will discuss some important numerical tools, which have not been developed or implemented in the standard numerical packages up to now. Second we will give an outlook on some of the most exciting new research directions in (computational) plasmonics.

Note that all three Sections 12.2 - 12.4 contain worked–out examples to illustrate the practice of the numerical methods, and to illustrate the physical interpretation of numerical results for each of these methods.

12.2 Frequency Domain Methods for Periodic Systems

Periodic systems like photonic crystals, waveguides and resonant cavities lead to electromagnetic modes, which have analytical properties similar to electronic states in periodic solids [8]. A fundamental technique in understanding the optical properties of these particular electromagnetic modes is the decomposition into harmonic time–dependent eigenmodes. frequency domain (FD) methods as a special case of these decomposition methods will expand electromagnetic fields into Fourier eigenmodes, which is often sufficient to understand the characteristics of optical materials in the absence of non-linear effects [4]. frequency domain methods usually start from basic photonic systems with translational symmetry, for which the solution of Maxwell's equations and the derived wave equations will give rise to electromagnetic Bloch states and photonic band structures [8].

In the following we will discuss the numerical details for the computing of these photonic band structures using FD schemes. We will show that under the particular assumption of the FD schemes, the solution of the wave equation will become equivalent to a matrix eigenvalue problem, which is one of the standard problems of numerics, and for which there are very powerful numerical methods available. We point out some of the technical problems of the FD scheme, and show an example of a photonic band structure for a two–dimensional honeycomb lattice. These numerical results were obtained using the standard software MPB [4], and they were visualized using Python modules written by the authors.

12.2.1 Photonic Band Structures

To find the eigenmodes using a frequency domain method, the general equation describing the propagation of electromagnetic waves in matter has to be

mapped onto an eigenvalue problem. For a linear dielectric function $\varepsilon(\boldsymbol{r})$ we may derive general wave equations for the electric and magnetic components of the propagating waves, which are of course related by Maxwell's equations [8]. For the magnetic field $\boldsymbol{H}$ the corresponding wave equation will be

$$\nabla \times \frac{1}{\varepsilon} \times \nabla \times \boldsymbol{H} = \frac{1}{c^2} \frac{\partial^2}{\partial t^2} \boldsymbol{H} \ , \tag{12.1}$$

which is constrained by the transversality condition

$$\nabla \cdot \boldsymbol{H} = 0 \tag{12.2}$$

Taking into account the periodicity and translational symmetry of a dielectric system described by $\varepsilon(\boldsymbol{r})$, we only consider time–dependent periodic solutions $\boldsymbol{H}(t)$ for the eigenvalue problem in Eq. (12.1) and Eq. (12.2). In analogy to the Bloch states of electrons in a solid [9], the corresponding electromagnetic Bloch states are

$$\boldsymbol{H}(\boldsymbol{k}, \boldsymbol{r}) = e^{i(\boldsymbol{k}\cdot\boldsymbol{r} - \omega t)} \boldsymbol{H}_{\boldsymbol{k}}(\boldsymbol{r}) \ , \tag{12.3}$$

where $\boldsymbol{k}$ is Bloch's wavevector (which is a pseudomomentum [9]), and $\boldsymbol{H}_{\boldsymbol{k}}$ is an amplitude factor periodic with the periodicity of the underlying photonic system. Substituting the ansatz of Eq. (12.3) into Eq. (12.1) results in

$$(\nabla + i\boldsymbol{k}) \times \left(\frac{1}{\varepsilon} (\nabla + i\boldsymbol{k}) \times \boldsymbol{H}_{\boldsymbol{k}} \right) = \left(\frac{\omega}{c} \right)^2 \boldsymbol{H}_{\boldsymbol{k}} \tag{12.4}$$

The operator on the left hand side of Eq. (12.4) is a positive semi–definite Hermitian operator, and Eq. (12.4) is a typical Hermitian eigenvalue problem. By introducing a complete set of basis states $\{\boldsymbol{\Psi}_i(\boldsymbol{r})\}_i$ we can map this eigenvalue problem onto a standard (Hermitian) matrix eigenvalue problem:

$$A\boldsymbol{H}_{\boldsymbol{k}} = \left(\frac{\omega}{c} \right)^2 B\boldsymbol{H}_{\boldsymbol{k}} \tag{12.5}$$

where A is the Hermitian operator on the left hand side of Eq. (12.4). The matrix element A_{lm} is given by $\boldsymbol{\Psi}_l^\dagger A \boldsymbol{\Psi}_m$ and B_{lm} is $\boldsymbol{\Psi}_l^\dagger \boldsymbol{\Psi}_m$. These products involve integration over the configuration space, in analogy to matrix elements in quantum mechanics [8].

Note that due to the $\boldsymbol{k}$ dependence of the Bloch states $\boldsymbol{H}_{\boldsymbol{k}}(\boldsymbol{r})$, the frequencies ω derived from the eigenvalue problem are also $\boldsymbol{k}$ dependent, i.e. $\omega = \omega(\boldsymbol{k})$. One usually solves the eigenvalue problem for a series of selected $\boldsymbol{k}$ vectors, and then interpolates in between these points to obtain the photonic band structure. See Fig. 12.1 as an example.

12.2.2 Numerical Details

The fields $\boldsymbol{H}_{\boldsymbol{k}}$ in Eq. (12.4) can be written as a linear expansion of basis vectors $\boldsymbol{\Psi}_i$ [4]

$$\boldsymbol{H_k} = \sum_{i=1}^{\infty} h_i \boldsymbol{\Psi}_i \ , \tag{12.6}$$

where h_i represents the expansion coefficients, which form a column vector in the matrix formulation of the eigenvalue problem of Eq. (12.5). From a computational point of view, it is impossible to calculate every single coefficient in the infinite sum that represents the field $\boldsymbol{H_k}$. Therefore this sum must be truncated at a sufficiently small number N, which should still yield a very good approximation to the exact $\boldsymbol{H_k}$.

Terminating the sum in Eq. (12.6) at a number N of basis functions also reduces the size of the column vectors and of the matrix operators to finite sizes of $N \times 1$ for the column vector and $N \times N$ for the matrix sizes. But even this mapping onto a matrix eigenvalue problem does not necessarily provide a directly solvable problem in practice. In particular when a traditional linear algebra approach is used to solve the matrix eigenvalue problem. The matrices involved could just be too large, requiring enormous amounts of computer memory, and the algorithms involved will basically never finish.

Fortunately, in most cases only a few lower eigenvalues or photonic bands are necessary to understand the interesting physics behind periodic optical systems like photonic crystals [8]. Then we do not have to solve for the entire spectrum of the eigenvalue problem, and the interesting bands are computed using a suitable iterative method. This approach also has a very positive impact on the computer memory needed by a typical FD scheme.

The iterative solution of the eigenvalue problem starts off with an initial guess of the eigenvector $\boldsymbol{H}$ (neglecting all labels for the moment being). Then one iteratively improves this guess, based on the fact that for all Hermitian operators the smallest eigenvalue λ satisfies

$$\lambda = \min_{\boldsymbol{H}} \frac{\boldsymbol{H}^{\dagger} A \boldsymbol{H}}{\boldsymbol{H}^{\dagger} B \boldsymbol{H}} \tag{12.7}$$

This type of problem is better known as the Rayleigh-quotient, which can perfectly be solved using a preconditioned conjugate–gradient method [8]. An interesting aspect of this method is the fact that we do not have to store the full matrices A and B in order to solve the minimization problem of Eq. (12.7). In fact the conjugate gradient method only requires the storage of the products $A\boldsymbol{\Psi}$ and $B\boldsymbol{\Psi}$, which saves a lot of computer memory.

The minimization of Eq. (12.7) leads to the determination of an eigenvalue λ and the related frequency ω, and we also obtain an eigenvector $\boldsymbol{H}$. This is the lowest band at a given $\boldsymbol{k}$ point. To obtain the next band values for the following frequency, we repeat the minimization in Eq. (12.7), but for a new

trial eigenvector $\boldsymbol{H}'$, which is constrained to be transverse and orthogonal to the lowest eigenvector $\boldsymbol{H}$. Hence the band structure may be obtained on the basis of a band-by-band minimization technique using the preconditioned conjugate–gradient method [8].

At this point we have to say something about the basis functions $\boldsymbol{\Psi}_i$. Due to the periodicity of the photonic system, a plane wave basis seems to be a natural choice. Then the eigenvectors $\boldsymbol{H}$ are expanded into basis functions $\boldsymbol{\Psi}_{\boldsymbol{G}} = \exp(i\boldsymbol{G} \cdot \boldsymbol{r})$ where $\boldsymbol{G}$ is a reciprocal lattice vector, and $\boldsymbol{r}$ is a vector in real (configuration) space. The vectors $\boldsymbol{G}$ are related to the fundamental lattice vectors $\hat{G}_i$ in reciprocal space by

$$\boldsymbol{G} = \sum_{i=1}^{3} m_i \hat{G}_i \ , \tag{12.8}$$

where m_i are integers. We can further simplify our numerics by taking only vectors $\boldsymbol{r}$ from a grid in real space, i.e.

$$\boldsymbol{r} = \sum_{j=1}^{3} n_j \hat{r}_j \ , \tag{12.9}$$

where the vectors $\hat{r}_j$ are integer fractions of the fundamental lattice vectors $\hat{R}_j$ in real space determined by the grid size, and n_j are integers. Then we can easily switch between the two grids in real and reciprocal space using Fast Fourier transform (FFT) routines [8], which is also useful for evaluating the vector operators in Eq. (12.4) . By switching from real to reciprocal space, the curl operator $\boldsymbol{\nabla}$ becomes $\boldsymbol{k} + \boldsymbol{G}$. Switching back from reciprocal to real space, we can easily carry out the successive multiplication by ε^{-1}. Switching to reciprocal space again, we can again easily carry out the last curl operation. Given the speed of the standard FFT routines, the operations on the left hand side of Eq. (12.4) can actually be carried out very efficiently.

The simplification of Eq. (12.4) by putting the modes on a grid in real space comes with its own problems, which are related to the inverse dielectric function ε^{-1}. The latter has to be evaluated on a real space grid as well, and irregular geometries at the interface between two dielectric media might not be covered by a moderate discretization grid in real space, leading to all sorts of numerical artefacts.

In order to avoid these problems, the dielectric function close to the interface has to be averaged. The most successful procedure is based on effective–medium theory [8]. If we take $\hat{n}$ as the vector normal to the surface and P is the projection operator onto $\hat{n}$, then the effective inverse dielectric constant $\tilde{\varepsilon}^{-1}$ for one unit of a cubic discretization grid is given by:

$$\tilde{\varepsilon}^{-1} = \overline{\varepsilon^{-1}} P + (\bar{\varepsilon})^{-1} (1 - P) \tag{12.10}$$

where the first term on the right hand side of Eq. (12.10) is the average of the inverse dielectric function projected onto the surface normal. That term is the dominant term when the incident field is parallel to the surface normal. The second term is the inverse of the averaged dielectric function, and this contribution dominates when the field is perpendicular to the normal of the surface. Away from the dielectric media this averaging plays no role, and we can just take the usual inverse of the dielectric constant at a particular grid point. For further details see Ref. [4].

12.2.3 Example: Honeycomb Lattice

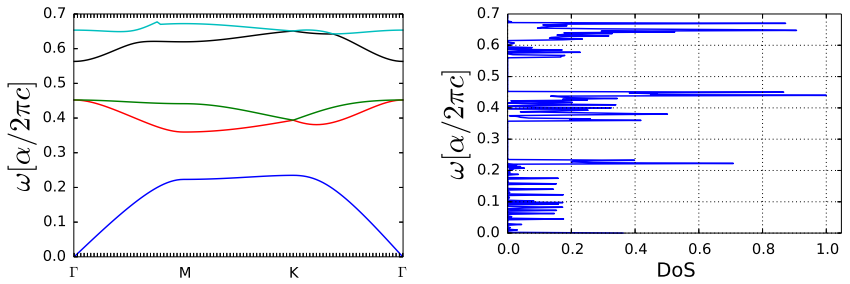

(a) (b)

Fig. 12.1: (a) TM modes in units of $\frac{\alpha}{2\pi c}$ for a honeycomb photonic crystal. In (b) we show the corresponding scaled density of states (DoS).

In Fig. 12.1 we show the transverse magnetic mode (TM) band structure for a two dimensional honeycomb lattice. The lattice points are populated with cylindrical objects of radius 0.2α, where α is the lattice constant. It is quite convenient to represent all bands in Fig. 12.1a in units of α, which stems from the fact that Maxwell's equations for systems with frequency-independent dielectric functions are scale–invariant. The cylindrical objects on the lattice consist of a dielectric material of dielectric constant 13. The background medium is air (i.e. dielectric constant equal to 1). Band gaps are observed between $\omega \sim 0.24\frac{\alpha}{2\pi c}$ and $0.35\frac{\alpha}{2\pi c}$, and $\omega \sim 0.46\frac{\alpha}{2\pi c}$ and $0.55\frac{\alpha}{2\pi c}$, which can also be seen in the density of states related to the band structure.

12.3 Time Domain Methods

The finite difference time domain method (FDTD) is a grid–based method similar to finite difference approaches [10]. In FDTD, Maxwell's equations are discretized using central differences with respect to the space and time derivatives. The resulting set of equations are solved in a leapfrog manner on a staggered grid, a technique which is also quite popular in fluid dynamics [1].

For the sake of simplicity, we will describe the basic mathematical formalism and some of the numerical details in one spatial and one temporal dimension, only. The corresponding formalism in four dimensional spacetime can be found in Ref. [2]. Although the FDTD method has a wide range of applications, we will provide one particular example that demonstrates the calculation of absorption and scattering cross sections, which are very useful in the context of plasmonic nanoparticles, see Ch. 11, Sec. 11.2.2 and Ch. 11, Sec. 11.3. These simulations were performed using the standard package MEEP [11], in combination with Python modules written by the authors [12].

12.3.1 Outline of the FDTD method

The frequency–domain methods are very successful in describing the properties of periodic systems like photonic crystals. But in order to examine a finite system, one has to use a supercell approach, which easily becomes very expensive from a numerical point of view. In such cases one needs a more robust numerical technique suitable for such systems, which is provided by the finite difference time domain method (FDTD).

The FDTD method simulates the propagation of the electromagnetic wave in the dielectric medium itself, rather than taking a deviation over a linear algebra problem. That way it becomes much easier to simulate very complex geometries, and non–linear media are not a problem for the FDTD method, in contrast to the FD scheme. We will come back to this problem in Sec. 12.5.

The key idea of the FDTD method is the staggering of the vector components for the electric fields $\boldsymbol{E}$ and the magnetic fields $\boldsymbol{H}$. This is called a Yee lattice as a tribute to Kane Yee, who pioneered the method [13]. The Yee lattice represents the physical space where the electromagnetic waves propagate, and an example is shown in Fig. 12.2. In order to describe the wave propagation on this grid, Maxwell's equation have to be discretized as well.

Let's base our analysis on a very general version of Maxwell's equations. As we are interested in wave phenomena, we must assume that there are no

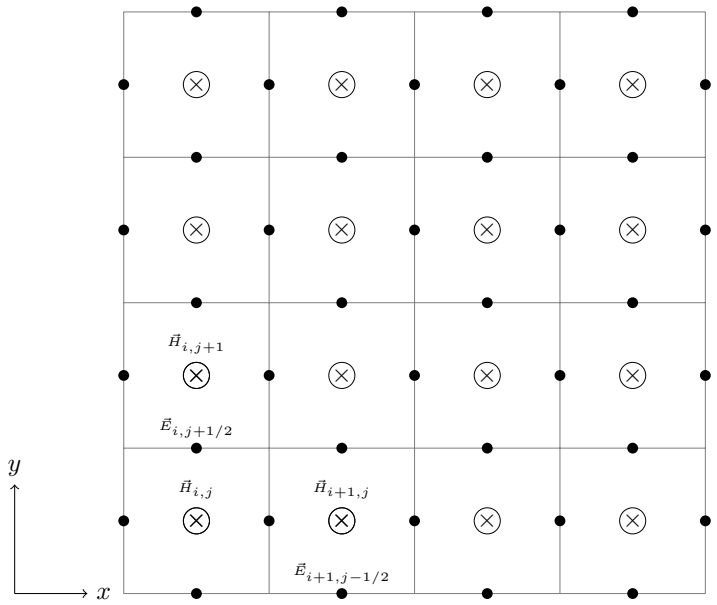

Fig. 12.2: Two-dimensional Yee lattice. The solid points represent the electric field $\boldsymbol{E}$ and the $\times$ points represent the magnetic field $\boldsymbol{H}$. The electric field propagates in the x-y plane while the magnetic field is perpendicular to $\boldsymbol{E}$. At the bottom left cell the magnetic field $\boldsymbol{H}$ coordinates are i, j. The neighbouring solid point in the y direction represents an electric field with coordinates $i, j + 1/2$.

source terms. But there could be electric and (artificial) magnetic currents characterized by electrical conductivites σ and magnetic resistivities ϱ. Thus:

$$\frac{\partial \boldsymbol{H}}{\partial t} = -\frac{1}{\mu}\nabla \times \boldsymbol{E} - \frac{\varrho}{\mu}\boldsymbol{H} \tag{12.11}$$

$$\frac{\partial \boldsymbol{E}}{\partial t} = \frac{1}{\varepsilon}\nabla \times \boldsymbol{H} - \frac{\sigma}{\varepsilon}\boldsymbol{E} \tag{12.12}$$

where ε is the electrical permittivity, and μ is the magnetic permeability.

Let us simplify Eqs. (12.11) and (12.12) by restricting the field propagation to the z-direction. Then for the different vector components of $\boldsymbol{E}$ and $\boldsymbol{H}$ these equations will simplify to

$$\frac{\partial E_x}{\partial z} = -\mu\frac{\partial H_y}{\partial t} - \varrho H_y \tag{12.13}$$

$$\frac{\partial E_y}{\partial z} = \mu\frac{\partial H_x}{\partial t} + \varrho H_x \tag{12.14}$$

and

$$\frac{\partial H_x}{\partial z} = \varepsilon \frac{\partial E_y}{\partial t} + \sigma E_y \tag{12.15}$$

$$\frac{\partial H_y}{\partial z} = -\varepsilon \frac{\partial E_x}{\partial t} + \sigma E_x \ , \tag{12.16}$$

Although the fields $\boldsymbol{E}$ and $\boldsymbol{H}$ retain their vector character in 3 dimensions, the problem is now effectively one-dimensional, because the fields can only vary in time, and in the z direction. We now want to introduce the general notation for the discretization scheme used in FDTD, and formulate our simplified setting in this form. Let the indices i, j and k represent the increments in the three spatial coordinates as depicted in Fig. 12.2. Then for a point on the grid the x-coordinates is given by $i\Delta x$ where i takes an integer value and Δx is the size of the grid cell in that particular direction. Furthermore, the fields are time-dependant and they have to be discretized accordingly. For this purpose, we take the time increment to be n and the time step to be Δt. The discretized Eqs. (12.13) – (12.16) read

$$\begin{aligned}
\frac{E_x^{i,j,k+1/2} - E_x^{i,j,k-1/2}}{\Delta z} &= -\frac{\mu_{xy}^{ijk}}{c_\circ} \frac{H_y^{i,j,k}|_{n+1/2} - H_y^{i,j,k}|_{n-1/2}}{\Delta t} \\
&\quad - \varrho_{xy} H_y^{i,j,k}|_{n-1/2} \\
-\frac{E_y^{i,j,k+1/2} - E_y^{i,j,k-1/2}}{\Delta z} &= -\frac{-\mu_{xx}^{ijk}}{c_\circ} \frac{H_x^{i,j,k}|_{n+1/2} - H_x^{i,j,k}|_{n-1/2}}{\Delta t} \\
&\quad + \varrho_{xy} H_x^{i,j,k}|_{n-1/2}
\end{aligned}$$

and similarly for the magnetic field

$$\begin{aligned}
-\frac{H_y^{i,j,k}|_{n+1/2} - H_y^{i,j,k-1}|_{n+1/2}}{\Delta z} &= \frac{-\varepsilon_{xx}^{ijk}}{c_\circ} \frac{E_x^{i,j,k-1/2}|_{n+1} - E_x^{i,j,k-1/2}|_n}{\Delta t} \\
&\quad + \sigma_{xx} E_x^{i,j,k-1/2}|_n \qquad (12.17) \\
\frac{H_x^{i,j,k}|_{n+1/2} - H_x^{i,j,k-1}|_{n+1/2}}{\Delta z} &= -\frac{-\varepsilon_{yy}^{ijk}}{c_\circ} \frac{E_y^{i,j,k-1/2}|_{n+1} - E_y^{i,j,k-1/2}|_n}{\Delta t} \\
&\quad + \sigma_{yy} E_y^{i,j,k-1/2}|_n \qquad (12.18)
\end{aligned}$$

Obviously only k is incremented, since it represents the propagation along the z-axis. The fields are also temporally staggered in a way that $\boldsymbol{E}$ is computed at a point in time $n\Delta t$, then $\boldsymbol{H}$ is computed at $(n+1/2)\Delta t$ instead of $(n+1)\Delta t$, where the next value of $\boldsymbol{E}$ is computed.

12.3.2 Numerical details

The solution of the equations starts with an initial value of the electric field on the Yee lattice. From the equations above, the temporal variation of $\boldsymbol{E}$

depends on the spatial variation of $\boldsymbol{H}$, and visa versa. Thus, propagating the initial values of $\boldsymbol{E}$ in space and time will update the following values of $\boldsymbol{H}$. Then propagating $\boldsymbol{H}$ will update $\boldsymbol{E}$ and so on. It is essential to choose a proper discretization grid. A grid spacing that is too small will propagate the solutions over extremely small distances and time intervals, whereas a grid spacing that is too large will lead to numerical instabilities [1].

The fields are updated in the above fashion until they reach the boundaries of the Yee lattice. At that point special assumptions have to be made in order to truncate the simulation. That is usually achieved via absorbing boundaries, that force all outgoing or reflected fields to decay. From a numerical point of view, an artificial absorbing material will be introduced called a perfectly matched layer (PML) [14]. Details of this procedure are discussed in Ref. [2]. The introduction of such a hypothetical material has to be done very carefully, in order to ensure that the material really absorbs all outgoing waves, and does not generate any strange numerical artefacts [15].

12.3.3 Example: Cross Sections Using FDTD

The computation of the scattering, as shown in Fig. (12.3b), as well as the absorption cross sections, as shown in Fig. (12.3a), is one of the important aspects of FDTD methods. The cross section is defined as the power transmitted through a unit surface area. The power P that goes through a surface S is given by the real part of the integral of the Poynting vector over the plane

$$P(\omega) = \mathrm{Re} \oiint_S \boldsymbol{E}(\omega, \boldsymbol{r}) \times \boldsymbol{H}(\omega, \boldsymbol{r}) \cdot \mathrm{d}\boldsymbol{A} \,, \tag{12.19}$$

where the fields $\boldsymbol{E}$ and $\boldsymbol{H}$ are specified at a given spatial point $\boldsymbol{r}$ and frequency ω.

One problem is the fact that the FDTD technique simulates the propagation of the fields in space and time. In order to calculate the power spectrum $P(\omega)$, the fields have to be transformed into the frequency domain. To perform the calculations one has to use a short–pulse source, which covers the range of the frequencies at which the cross sections are required to be calculated. With this the fields that propagate out of the surface S are stored for each time step. Then one can perform a Fourier transformation according to

$$\tilde{\boldsymbol{E}}(\omega) = \frac{1}{\sqrt{2}} \sum_n e^{i\omega n \Delta t} \boldsymbol{E}(n\Delta t)\Delta t \,, \tag{12.20}$$

which is known as discrete–time Fourier transformation. It is the preferred technique used by MEEP, but other methods to extrapolate Fourier transform can be used as well. For details and further references see Ref. [11].

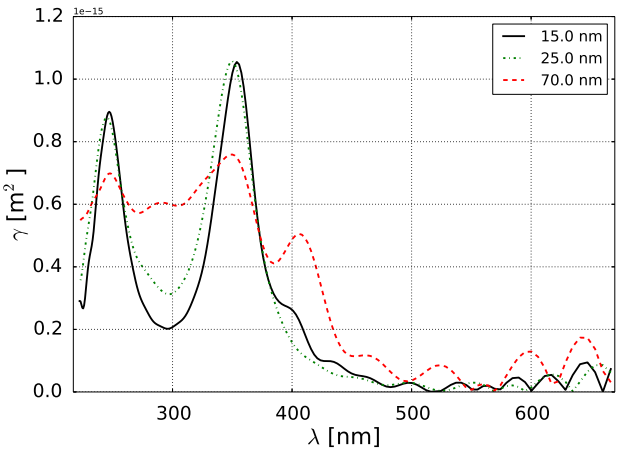

(a)

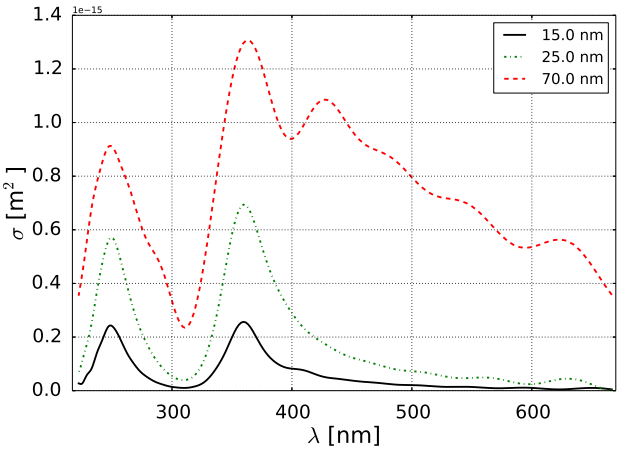

(b)

Fig. 12.3: In (a) we show the absorption cross–section and the scattering cross–section in (b) for a simple two-dimensional plane surface with silver sphere positioned in its centre. The simulation is performed using the FDTD method. Three different radii of the sphere, 15, 25 and 70 nm are considered during the simulation.

12.4 *Ab Initio* Dielectric Functions

A proper description of the plasmonic behaviour of a material largely depends on the knowledge of the frequency–dependent dielectric function, which is a

characteristic of the excited electronic states of a material. It is therefore necessary to determine the ground state and the excited electronic states of the system, and to compute the properties of optical transitions between those states. This may be based on a non-relativistic Schrödinger equation.

In the following we will briefly introduce the theoretical background of the most relevant *ab initio* numerical techniques which require no empirical information. Many of these methods can be applied to extended and isolated systems alike. However the numerical effort can be enormous in some cases. We will focus here on density functional theory [6, 7] and related methods, which are the methods of choice for extended systems and large isolated systems like clusters.

12.4.1 Density Functional Theory

density functional theory (DFT) is one of the standard methods of computational physics and chemistry for several decades. Detailed descriptions can be found in many books [16, 17, and others], and these details need not be repeated here. The N-body Schrödinger equation depends on $3N$ variables, or $4N$ if spin is included. This quickly leads to infeasible system sizes, and therefore approximations and reformulations have to be found to solve the corresponding quantum mechanical N-body problem also for larger systems. In almost all applications of *ab initio* methods, it is assumed that the Born–Oppenheimer approximation [18] holds, which is also called adiabatic approximation. The nuclei of a molecule, cluster or solid are much heavier than the electrons, and therefore it can be assumed that the motions of the nuclei are largely decoupled from the motion of the electrons, such that for any given nuclear configuration the electrons will be in their respective ground states. We are now left with the task to solve the electronic Schrödinger equation.

The basic idea of density functional theory goes back to Hohenberg and Kohn [6]. It can be described as follows: For a quantum mechanical system the ground state of the system is completely determined by the ground state charge density. In other words there is a unique mapping between the charge density ϱ and the total energy E of the system via a charge density dependent energy functional $E[\varrho]$. Knowledge of the charge density allows us to dramatically reduce the number of spatial degrees of freedom from $3N$ to 3, which also reduces the computational complexity quite substantially. According to Hohenberg–Kohn the unknown charge density dependent energy functional $E[\varrho]$ should look like this:

$$E[\varrho] = T[\varrho] + \int \mathrm{d}\boldsymbol{r}\, v_{\mathrm{ext}}\varrho(\boldsymbol{r}) + E_H[\varrho] + E_{xc}[\varrho] \tag{12.21}$$

Here T stands for the functional of electronic kinetic energy, v_{ext} are externals potentials like the nucleus–electron interaction, E_H is the functional of a classical Hartree/Coulomb interaction and E_{xc} is the exchange-correlation functional.

In order to make density functional theory useful for everyday numerical simulations, and in order to implement it in existing *ab initio* program packages, another ansatz was very important. Kohn and Sham [7] showed, that there is a non-interacting reference system, whose one-particle Schrödinger equation takes the form

$$(T + v_{\text{eff}}(\boldsymbol{r}))\psi_i(\boldsymbol{r}) = \epsilon_i(\boldsymbol{r})\psi_i(\boldsymbol{r}) \,, \tag{12.22}$$

with an effective potential v_{eff} that yields the same ground state density ϱ as the real interacting system. Then the charge density ϱ is given by the independent particle orbitals ψ_i, which are eigenstates of the one-particle Schrödinger equation (12.22), i.e.

$$\varrho = \sum_i^N |\psi_i(\boldsymbol{r})|^2 \tag{12.23}$$

This Kohn–Sham approach together with the idea of a charge density dependent energy functional leads to the Kohn–Sham density functional theory (KS-DFT):

$$E[\varrho] = \sum_i^N \epsilon_i - E_H[\varrho] + E_{xc}[\varrho] - \int \mathrm{d}\boldsymbol{r}\, \frac{\delta E_{xc}[\varrho]}{\delta \varrho(\boldsymbol{r})} \varrho(\boldsymbol{r}) \tag{12.24}$$

The one-particle Schrödinger equation (12.22) follows from the minimization of the KS energy functional $E[\varrho]$ with respect to the set of orbitals ψ_i.

In principle the KS–DFT allows for an exact solution for the ground state of the electronic Schrödinger equation. However, while it has been proven that there exists an exchange–correlation functional $E_{xc}[\varrho]$, which yields the correct electronic ground state, this functional has never been found, and there is no guarantee that such a functional would have an analytic form. Nevertheless, a large number of approximate functionals are known and widely used with great success. The available functionals are grouped according to their analytic form, and there has even been assigned a Jacob's ladder for the different levels of approximation [19, 20]. The simplest approximation is the local density approximation (LDA) [21], where the exchange–correlation is directly dependent on the value of the charge density in space. LDA functionals can in principle be derived without empirical parameters, constraint by the requirement that they must reproduce the properties of the homogeneous electron gas. The next level of approximations are the Generalized Gradient Approximations (GGA) [22, 23], which depend on the charge density and its spatial derivatives. GGA functionals have already a lot of degrees

of freedom in their construction. They are the most common functionals for ground state calculations. The third step on the ladder are the metaGGAs, which also depend on the second derivatives of the charge density and/or on the kinetic energy density. Despite some promising efforts, metaGGAs have not become numerical standard yet, because of the difficulties implementing them for perturbation theory and linear response equations.

The KS–DFT in itself is not suited to describe excited state properties as the orbitals are generally not related to the physical one-electron states (quasi-particles!), and therefore the predicted band gaps are generally largely underestimated. There are a few common approaches being pursued to overcome those short–comings of DFT.

One is to use highly parametrized metaGGAs or even more complex functionals, which deliver improved band structures and band gaps [24]. While these functionals have little numerical overhead, their complicated structures and high levels of parametrization have two distinct disadvantages. First it is difficult to derive some analytical properties like the elastic strain, which limits their usability and makes the implementation of metaGGAs less straightforward. Second it is difficult to anticipate when the functionals actually fail to describe a system properly.

Another promising approach is to mix DFT with Hartree–Fock theory. For these so called hybrid functionals [25] a certain part of the DFT exchange–correlation functional is mixed with the Hartree–Fock potential. While these hybrid functionals tend to give much better results than the normal DFT functionals, the theoretical motivation for the specific mixing of different functionals is very difficult. Furthermore most hybrid functionals increase the numerical effort quite dramatically.

The third promising approach is to use the Green's function methods as part of a general quasi-particle approach to improve the band gaps and band structures compared to DFT. The most common implementation of the Green's function method is Hedin's GW method [26]. The GW method is in principle exact, but numerous approximations must be made to achieve acceptable numerical effort.

Besides the proper choice of the exchange–correlation functionals, at least two other important technical choices have to be made, concerning the representation of the Kohn-Sham wave functions. In principle these electronic wave functions can be expanded in any complete set of basis functions. However for the purpose of numerical simulations only truncated sets can be handled, and the size of these restricted basis sets will directly influence the overall computational effort. For isolated systems one uses a Gaussian basis set or the Linear Combination of Atomic Orbitals (LCAO) approach, because these basis func-

tions are close to be molecular orbitals. Extended periodic systems however exhibit electronic Bloch states, which are best described by a plane–wave basis set. It is always up to the user to decide, how many basis functions should be included in a given simulation run, based on accuracy and speed/memory requirements.

For extended periodic systems one is not only concerned with the real space properties of the system, but also with the reciprocal space (or k-space) properties related to the electronic Bloch states. The reciprocal space is dual to the real (physical) space, and lattices embedded in both spaces are related via a Fourier transform [9]. One usually chooses a point mesh to sample the reciprocal space. The denser the resulting meshes the higher the accuracy, and unfortunately also the larger the computational effort, because the Schrödinger equation has to be solved at each of those mesh points in reciprocal space.

12.4.2 Linear Response and the Time Dependent Density Functional Theory

In order to calculate the dielectric function, we have to evaluate the response of a material to an external perturbation in terms of an applied electromagnetic field. If this perturbation is weak compared to the internal electric fields caused by the ions, then the induced fluctuations in the charge density can be described within the framework of time–dependent perturbation theory, where these charge densities fluctuations will be linearly dependent on the applied perturbation. In the following we will give a brief summary of the linear response time dependent density functional theory (LRTDDFT) approach, which can be used to calculate the dielectric function from first principles. A more detailed description of this method can be found in [27].

Within LRTDDFT the response of the systems can be expressed in different but closely related forms, which are the dielectric response, the polarization or the density response. For example an incident beam of electromagnetic waves causes a change in the external electric field and therewith in the external potential v_{ext} of the excited system. The density response function

$$\chi(\boldsymbol{r}, \boldsymbol{r}', t - t') = \frac{\delta n(\boldsymbol{r}, t)}{\delta v_{\text{ext}}(\boldsymbol{r}', t')} \tag{12.25}$$

is the reaction of the electron density n to this perturbation. The density response is directly related to the relative dielectric function ε_r by the Coulomb kernel ν:

$$\varepsilon_r^{-1} = 1 + \nu\chi \tag{12.26}$$

We have seen in the previous Section that we can use the Kohn–Sham DFT to calculate the ground state charge densities, but not under time–dependent

perturbations. Here the more general framework of time–dependent density functional theory (TDDFT) [28] must be used. Then the time independent Schrödinger equation is replaced by a time dependent equation, and all physical quantities become time dependent. Also instead of determining the lowest energy solution, the quantum mechanical action integral will be minimized.

For the time evolution of isolated systems TDDFT can basically simulate arbitrary types of perturbations, including strong laser fields. But in practice the simulation of perturbed extended periodic systems is limited to the frequency domain linear response TDDFT method. Then one can express the density response χ in terms of the independent particle response χ^0 using a Dyson equation approach:

$$\chi(\boldsymbol{r},\boldsymbol{r'},\omega) = \chi_0(\boldsymbol{r},\boldsymbol{r'},\omega) \iint_\Omega d\boldsymbol{r}_1 d\boldsymbol{r}_2 \; \chi_0(\boldsymbol{r},\boldsymbol{r}_1,\omega) K(\boldsymbol{r}_1,\boldsymbol{r}_2) \chi(\boldsymbol{r}_2,\boldsymbol{r'},\omega), \tag{12.27}$$

Here K is the exact Coulomb and exchange–correlation kernel

$$K(\boldsymbol{r}_1,\boldsymbol{r}_2) = \frac{1}{|\boldsymbol{r}_1 - \boldsymbol{r}_2|} + \frac{\partial V_{xc}[n]}{\partial n} \tag{12.28}$$

Electromagnetic waves are periodic phenomena, and therefore we easily switch from to the time to the frequency domain. The independent particle, or non-interacting, response function can be readily computed from the KS-DFT eigenvalues $\epsilon_{n\boldsymbol{k}}$ and eigenfunctions $\psi_{n\boldsymbol{k}}(\boldsymbol{r})$:

$$\chi^0(\boldsymbol{r},\boldsymbol{r'},\omega) = \sum_{\boldsymbol{k},\boldsymbol{q}}^{\mathrm{BZ}} \sum_{n,n'} \frac{f_{n\boldsymbol{k}} - f_{n'\boldsymbol{k}+\boldsymbol{q}}}{\omega + \epsilon_{n\boldsymbol{k}} - \epsilon_{n'\boldsymbol{k}+\boldsymbol{q}} + i\eta} \psi^*_{n\boldsymbol{k}}(\boldsymbol{r}) \psi_{n'\boldsymbol{k}+\boldsymbol{q}}(\boldsymbol{r}) \psi_{n\boldsymbol{k}}(\boldsymbol{r'}) \psi^*_{n'\boldsymbol{k}+\boldsymbol{q}}(\boldsymbol{r'}) \tag{12.29}$$

The $f_{n\boldsymbol{k}}$ are the Fermi occupation numbers of the eigenstates. In the case of extended systems one has to consider the whole Brillouin zone in order to determine the response of such a system. Therefore the sum in Eq. (12.29) runs over all the points $\boldsymbol{k}$ in first Brillouin zone. This also means that the possible momentum transfer $\boldsymbol{q}$ by the perturbation must be taken into account. In the case of light as a source for perturbations of the system we are always operating in the optical limit of $\boldsymbol{q} = 0$, because the moment of electromagnetic plane waves is very small.

For spatially periodic extended systems, a formulation of the independent particle response function in reciprocal space will be more useful than a real space description. A Fourier transform of Eq. (12.29) will generate the expression for the independent particle response in terms of the wave vectors $\boldsymbol{q}$ of the incoming wave, and of the reciprocal lattice vectors $\boldsymbol{G}$. The Fourier coefficients, derived by Adler [29] and Wiser [30], are written as

$$\chi^0_{\boldsymbol{G}\boldsymbol{G}'}(\boldsymbol{q},\omega) = \frac{1}{\Omega}\sum_{\boldsymbol{k}}^{\mathrm{BZ}}\sum_{n,n'}\frac{f_{n\boldsymbol{k}} - f_{n'\boldsymbol{k}+\boldsymbol{q}}}{\omega + \epsilon_{n\boldsymbol{k}} - \epsilon_{n'\boldsymbol{k}+\boldsymbol{q}} + i\eta}\langle\psi_{n\boldsymbol{k}}|e^{-i(\boldsymbol{q}+\boldsymbol{G})\cdot\boldsymbol{r}}|\psi_{n'\boldsymbol{k}+\boldsymbol{q}}\rangle_{\Omega_{\mathrm{cell}}}\times \langle\psi_{n\boldsymbol{k}}|e^{i(\boldsymbol{q}+\boldsymbol{G}')\cdot\boldsymbol{r}'}|\psi_{n'\boldsymbol{k}+\boldsymbol{q}}\rangle_{\Omega_{\mathrm{cell}}} \tag{12.30}$$

The full interacting density response is then given by

$$\chi_{\boldsymbol{G}\boldsymbol{G}'}(\boldsymbol{q},\omega) = \chi^0_{\boldsymbol{G}\boldsymbol{G}'}(\boldsymbol{q},\omega) + \sum_{\boldsymbol{G}_1\boldsymbol{G}_2}\chi^0_{\boldsymbol{G}\boldsymbol{G}_1}(\boldsymbol{q}\omega)K_{\boldsymbol{G}_1\boldsymbol{G}_2}(\boldsymbol{q})\chi_{\boldsymbol{G}_2\boldsymbol{G}'}(\boldsymbol{q},\omega) \tag{12.31}$$

In this notation the (microscopic) inverse dielectric function is given as (see Eq. (12.26))

$$\varepsilon^{-1}_{\boldsymbol{G}\boldsymbol{G}'}(\boldsymbol{q},\omega) = \delta_{\boldsymbol{G}\boldsymbol{G}'} + \frac{4\pi}{|\boldsymbol{q}+\boldsymbol{G}|^2}\chi_{\boldsymbol{G}\boldsymbol{G}'}(\boldsymbol{q},\omega) \tag{12.32}$$

In most practical cases one is interested in the related macroscopic dielectric function $\varepsilon_M (= \varepsilon_r)$, which can be obtained as follows:

$$\varepsilon_M(\boldsymbol{q},\omega) = \frac{1}{\varepsilon^{-1}_{00}(\boldsymbol{q},\omega)} \tag{12.33}$$

In principle Eq. (12.31) is exact. However up to this point it has not been possible to derive accurate time dependent exchange correlation kernels. The popular ALDA (adiabatic local density approximation) kernel does not correlate different times t, and it diverges with $1/q^2$, which means it does not contribute to the optical limit. Therefore this kernel is also not able to describe excitonic effects, for which the more cumbersome Bethe–Salpeter equation [27] has to be solved. This problem does not occur for isolated systems, where TDDFT is reported to give very good results.

In addition to the challenge of finding good exchange–correlation kernels, a number of other approximations are commonly used. The simplest approximation is the independent particle approximation, which uses χ^0 instead of χ in Eq. (12.32). Random phase approximations consists of neglecting the exchange-correlation part of the kernel in Eq. (12.31). Neglecting local field effects leads to an approximation, which ignores the change in screening due to local dipole interactions that are represented by the off-diagonal elements in $\chi_{GG'}$. The impact of these different approximations on the accuracy of the numerical results will be illustrated in the following Section.

With the knowledge of the dielectric function calculated in Eq. (12.33), derived properties like the electron energy loss spectrum (EELS) can be easily obtained using the relation given by Eq. (11.17). In contrast to the analytic Lorentz model, *ab initio* dielectric functions can also be computed for non-zero momentum transfer $\boldsymbol{q}$. The relevance of this feature can be seen in the loss function of graphene, which is shown in Fig. 12.4 [31]. Graphene has

two (bulk) plasmons, where the π plasmon is located around 5 eV, and the $\pi + \sigma$ plasmon is located around > 15 eV. Both resonances show up as peaks in the electron energy loss function of Fig. 12.4. One can also see that both plasmons experience strong dispersion, and that they have their maxima for $\|\boldsymbol{q}\| \approx 0.2\,\text{Å}^{-1}$, i.e. some distance away from the limit described by analytical dispersionless models of the Drude–Lorentz type, and at higher energies.

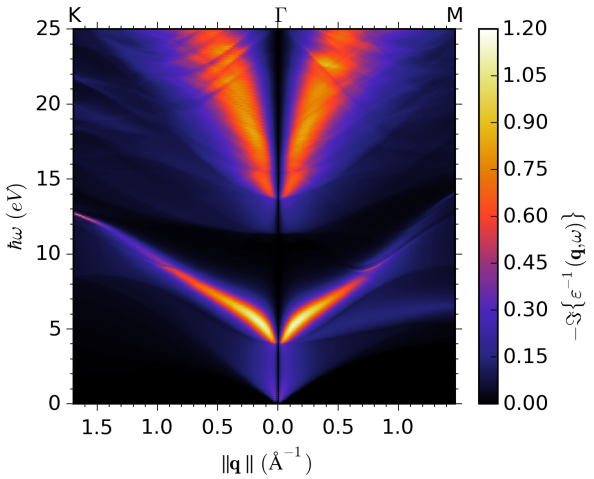

Fig. 12.4: electron energy loss spectrum of graphene as calculated on the LRTDDFT level of theory. Reprint from [31] Fig. 3.

In this Section we have limited ourselves to contributions for the dielectric function, which stem from interband transitions only, which limits the validity of this approach to semiconductors and insulators. It is however possible to add the intraband contributions to the dielectric function in an ad hoc fashion. To this end a term corresponding to the Drude model in Eq. (11.9) is added to the dielectric function. The plasma frequency ω_p can easily be calculated from the *ab initio* data, but unfortunately the damping constant γ must be guessed, which adds some uncertainty to the final results. As the Drude model does not depend on q, such an ad hoc treatment to describe metallic systems can ony be used for calculations in the optical limit of $q = 0$.

12.4.3 Example: ZnO

In this Section we illustrate the numerical procedures to calculate dielectric functions, and we give optical evidence to the advantages and short-comings of the different methods and approximations described above. We chose ZnO as an example for this Section, because it is a common direct band gap semiconductor used in photovoltaics. It has the advantage of a relatively small unit cell with only four atoms, which allows people to reproduce the present calculations even without access to a super computing facilities. The ground state DFT calculations were performed using the Quantum Espresso package [32], and the linear response and GW calculations were performed using the Yambo package [33].

Ab initio simulations of dielectric functions always refer to the mono–crystalline phase. ZnO has a hexagonal unit cell of the wurtzite type. As a first step the numerical parameters of the DFT calculations have to be converged. These are usually the size of the basis set into which the wave functions are expanded, and the number of points to sample the Brillouin zone in k-space. Secondly, it is often prudent to relax the structures taken from databases. DFT delivers only approximate numerical solutions, where the global minimum of the equilibrium energy functional in terms of cell parameters and atomic positions is slightly different from a real structure.

The next step is to calculate the ground state charge density and electron wave functions within DFT, which are then taken as input for the linear response LRTDDFT. ZnO has a direct band gap of about 3.34 eV, however DFT estimates the band gap to be as small as 0.82 eV. This leads to considerable errors in the dielectric response. In Fig. 12.5 we compare the dielectric function of ZnO computed in different numerical ways with the experimental results by Gori et al. [34]. The experimental curve shows a strong onset in the real and imaginary parts of the dielectric function at the position of the band gap, which is possibly caused by an exciton. For the rest of the spectrum the curves are flat without any prominent peaks. The computed curves are all much more wobbly than the experimental results, which is a numerical artefact caused by the limited size of the grid covering the first Brillouin zone ($15 \times 15 \times 9$). It is often not possible to sufficiently increase the grid density in order to obtain a clean picture.

Let us comment on the different approximations used in Fig. 12.5. The simplest approximation in the computation of the linear response is the independent particle model (IP). It directly uses the KS-DFT orbitals and calculates transitions between occupied and unoccupied bands without any further correlations. This model shows an onset in the absorption at a DFT band gap of

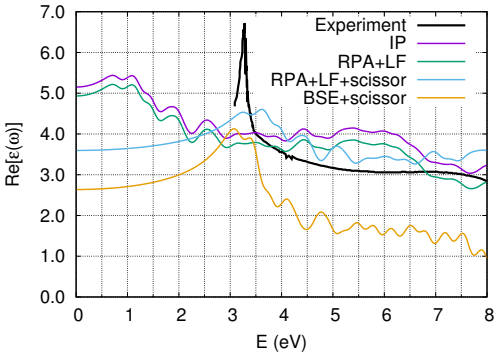

(a)

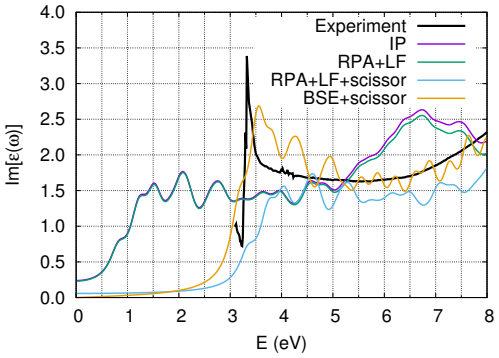

(b)

Fig. 12.5: Real (a) and imaginary (b) part for the dielectric function of zinc oxide calculated at different levels of approximation.

0.8 eV, which is much too low, and therefore the whole dielectric function is heavily red shifted.

The next level of approximation consists of introducing the Hartree kernel into the response function (RPA), and to calculate the response for a number of $\boldsymbol{G}$ vectors. This will introduce the local field (LF) corrections to the response function. This level of approximation could be considered fairly accurate, but it does not correct the band gap problem, and it does not take into account excitonic effects. The RPA+LF model can be expected to produce accurate static limits ε_∞ of the dielectric function. If one imagines these curves to be rigidly blue shifted they reproduce the experimental curves reasonably well, except the excitonic peak at the band gap energy. Therefore one can introduce a scissor operation to blue shift all unoccupied bands, such that the desired band gap is obtained. This however means, that energy eigenvalues and the

corresponding wavefunctions are no longer consistent. Then the real part of the dielectric function is severely underestimated, especially below the band gap, but the imaginary part can be quite reasonable.

In order the reproduce all the features of the experimental dielectric function, one has to solve the Bethe–Salpeter equation (BSE), which then includes excitonic effects. As can be seen in Fig. 12.5 the BSE dielectric functions matches the experimental one quite well. There are however a few set-backs. The BSE is numerically much more cumbersome than the LRTDDFT, which practically forbids well-resolved curves to be computed by this method. In addition, the real part of the dielectric function is underestimated. As can be seen form Eq. (12.29) or Eq. (12.30), the density response (and therefore also the dielectric function) has a form which can be described by a sum of Lorentz oscillators. In those the real part on the side of ω_0 does not approach zero, but a constant value. Therefore one needs to include all oscillators up to very high energies in this sum of Lorentz oscillators just to compute converged absolute values of the real part of the dielectric function. This however is prohibitively expensive in the BSE framework, and only a small number of transitions are included in the graph.

Better curve shapes might be obtained after we base the BSE calculation on eigenvalues and functions calculated using the GW method. This provides reasonable band gaps and also reasonable quasi-particle energies.

12.5 Plasmonic Photonic Crystals

In this Section we examine the optical properties of periodic arrays of dielectric elements placed on a metal substrate, and thus introduce the concept of a photonic crystal [8] into the field of plasmonics. This is a very interesting theoretical and experimental scenario, where one can study the formation of photonic band gaps for evanescent surface plasmon polariton waves. Even more interesting is the further localization of these evanescent Bloch waves after introducing varying degrees of structural disorder. The conditions under which a Bloch-like SPP will be either localized, extended or even form a critical state are not clear a priori [35]. It is also not clear how optical localization can be separated from the evanescent character of an SPP. Being of mainly fundamental interest at the moment, the topic of plasmonic photonic crystals could nevertheless have important implications for the future development of nanoscale plasmonic devices, where the localized, extended or evanescent character of SPPs can be controlled and manipulated. Computational methods will certainly play a very distinct role in the development of basic theoretical and practical concepts for this field.

Photonic crystals provide control over the flow of electromagnetic waves. They can stop the propagation of light with certain frequencies, forming photonic band gaps as the one shown in Fig. 12.1. These unique optical properties of photonic crystals have their origin in the translational symmetry of their dielectric structures [8]. One can tune the optical properties of photonic crystals by introducing dielectric point defects, or by tuning the dielectric contrast.

More interestingly, the presence of surface plasmons polaritons (SPP) can have a quite similar effect, and enhance these optical properties even further [36]. Placing a photonic crystal on a metallic surface leads to surface plasmon polaritons [37] at the interface between the heterogeneous dielectric metamaterial and the metal, see Ch. 11, Sec. 11.2.2. SPP modes are decaying, and they influence the dielectric properties of photonic crystals by introducing non-linearities [38], which can localize certain photonic modes.

In the following Section, plasmonic photonic crystals are treated using perturbation theory. We start with a brief description of a perturbative scheme developed by us to study plasmonic photonic crystals. We then give an example of the photonic band structure for a 2D honeycomb crystal placed on an aluminium surface. The core numerical calculations are performed using MPB [4], while the extension that deals with the perturbation of the bands was developed by ourselves using Python.

12.5.1 Perturbation Theory

In contrast to textbook examples of standard photonic crystals, the variation of the dielectric function at a given frequency is cucial for the description of plasmonic photonic crystals, and it will also introduce non-linearities. Such changes will modify the resulting band structures. Within the framework of perturbation theory [39], the change in the band structure $\Delta\omega$ is related to the change in the dielectric function $\Delta\varepsilon$, as well as to the electric field $\boldsymbol{E}(\boldsymbol{r})$ itself, see [8]:

$$\Delta\omega = -\frac{\omega}{2}\frac{\int \mathrm{d}^3 r \Delta\varepsilon |\boldsymbol{E}(\boldsymbol{r})|^2}{\int \mathrm{d}^3 r\, \varepsilon |\boldsymbol{E}(\boldsymbol{r})|^2} \tag{12.34}$$

Here we have neglected the $\boldsymbol{k}$ dependence of the band structure $\omega(\boldsymbol{k})$ and of the fields $\boldsymbol{E}(\boldsymbol{k}, \boldsymbol{r})$. The metallic substrate alters the dielectric function of a photonic crystal, which leads to different effective dielectric functions $\varepsilon_{\mathrm{spp}}$ at both sides of the interface [38]

$$\varepsilon_{\mathrm{spp}}(\omega) = \frac{\varepsilon_m(\omega)\varepsilon_d(\boldsymbol{r})}{\varepsilon_m(\omega) + \varepsilon_d(\boldsymbol{r})} \tag{12.35}$$

Here $\varepsilon_d(\boldsymbol{r})$ is the composite dielectric function of the material forming the photonic crystal (silicon and air for example), and $\varepsilon_m(\omega)$ is the metallic di-

electric function, which can be modelled using a standard formula such as the Drude model:

$$\varepsilon_m = 1 - \frac{\omega_p^2}{\omega^2 - i\omega\gamma} \tag{12.36}$$

Remember that ω_p is the plasma frequency of the metal and γ is a damping constant. It is also worth mentioning that for simulations of the plasmonic photonic band structures, only the real part of ε_{spp} will be of interest. The presence of the complex part does not influence the features of the band structure, it only leads to a gradual decay of the surface waves [40].

We now have a very interesting theoretical, numerical and experimental setting. We can now systematically introduce disorder into the photonic crystal component, which leads to the localization of photonic Bloch states. On top of that the imaginary part of ε_{spp} leads to an evanescent character of the Bloch-like states in a plasmonic photonic crystal anyway. A detailed study of such models is likely to tell us something fundamental about the character of optical localization [35], and how we can actually manipulate it in practice. The following example will hopefully wet the appetite of some of our readers to dig deeper into this fascinating subject, and to improve the necessary numerical tools as well.

12.5.2 Example: Plasmonic Photonic Band Structure

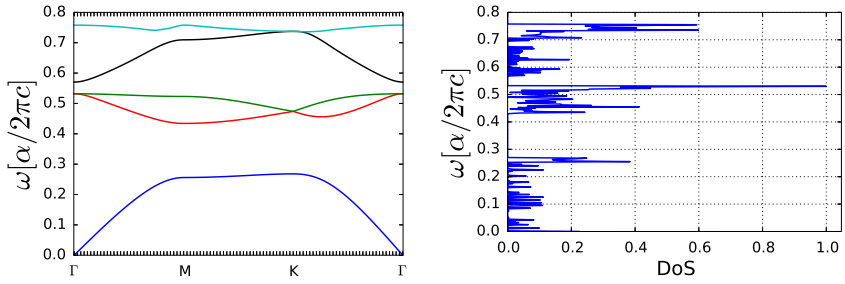

(a) (b)

Fig. 12.6: (a) TM modes in units of $\frac{\alpha}{2\pi c}$ for a plasmonic photonic crystal. In (b) we show the corresponding scaled density of states (DoS).

To compute the perturbative correction of the harmonic modes (Bloch states), we use first order (self–consistent) perturbation theory [39]. An unperturbed

band structure is computed first, using a constant dielectric function for the feature of a regular photonic crystal. Then within a small window of frequencies ω to $\omega + \Delta\omega$, the small perturbative change in the (average) frequency is computed. We thus assume that within this small frequency window, the effective dielectric function will not remarkably deviate from its initial value, and therefore the resulting band structures are approximately self–consistent. This of course is just an idealized assumptions, and larger deviations cannot be treated by this method. In the following we require that relative changes in the dielectric constant ($\frac{\Delta\varepsilon}{\varepsilon}$) have to be less than 1%, and therefore a first order perturbation theory for small deviations should be sufficient. Larger fluctuations in the dielectric function might require higher order perturbation theories, or even iterative schemes.

For a sample calculation of a plasmonic photonic band structure we essentially use the same model as for Fig. 12.1a in Sec. 12.2, which is the honeycomb lattice. This lattice is placed on aluminium substrate, and the dielectric function for the metallic component is described by the Drude model in Eq. (12.36). The presence of SPP also influences the dielectric constant of the cylindrical objects and of the background, which are modified according to Eq. (12.35).

The plasma frequency of aluminium is taken to be 2.24×10^{16} rad/sec, $\gamma = 1.22 \times 10^{14}$ rad/sec [41]. In order to compute the effect SPP on the dielectric function, the frequency units have to be converted to match the units of ω_p and γ. The substitution of real values for the lattice constants influences the resulting band structure, and it removes the scale–invariance of Maxwell's equations. Moreover, it is also important for the validity of our numerical approach. In Fig. 12.6 a plasmonic photonic band structure is shown for $\alpha = 500$ nm. The lower band gap for the plasmonic photonic crystal is wider compared to its photonic counterpart shown in Fig. 12.1.

12.6 Open Questions

In this final Section we briefly want to emphasize some of the most recent developments in the field of (computational) plasmonics, together with some new challenges. In Sec. 12.6.1 we will discuss some numerical problems, where proper solutions could have a major impact on the field of computational plasmonics.

12.6.1 Missing Numerical Tools

As we have already pointed out several times that the numerical approach to many interesting plasmonics phenomena and the modeling of derived applications is basically multi-scale. The numerical methods described in Sec. 12.1 are certainly the most powerful tools on an atomic to mesoscopic level (*ab initio* methods like TD-DFT, see Sec. 12.4), or from a microscopic to macroscopic level (FD and FDTD methods, see Sec. 12.2 and 12.3).

However, each of these methods has conceptional limitations. Even within their usual range of validity these methods tend to become very inefficient, whenever the systems under consideration become very heterogeneous. Furthermore if we want to treat a typical multi-scale problem in plasmonics with sufficient accuracy, then we often have to extend the range of validity for each these methods by combining them with other types of numerical tools, a general procedure that does not always work very well, nor is it really well understood from a mathematical point of view [1].

Classical electrodynamics has circumvented many of these fundamental problem by introducing light-matter interactions simply through the permittivity $\varepsilon(\omega)$ and the permeability $\mu(\omega)$. But nowadays we have the possibility to determine these materials properties for idealized systems using first principles numerical methods, as discussed in Sec. 12.4. This raises the question, whether the resulting optical properties can also be extended to describe imperfect systems.

In the following we will briefly discuss some ideas concerning the implementation of *ab initio* optical properties in the standard FD and FDTD methods.

12.6.1.1 Implementation of Tabulated Data for $\varepsilon(\omega)$

A lot of simulations in this Chapter have been carried out using model dielectric functions. Although such an approach often often lead to very good results, it also has its limitations. A better and more realistic approach would be based on tabulated data, generated using *ab initio* methods described in Sec. 12.4.

Unfortunately most of the available numerical tools in computational electromagnetics are not designed to accommodate tabulated data. In fact most of them are only designed to cater for user–defined functions. For example MEEP, which is a very sophisticated finite difference time domain solver, on one hand offers the interesting possibility to solve Maxwell's equations for

systems that have frequency-dependent dielectric functions, but that choice is limited to a certain number of model dielectric functions of Drude–Lorentz type. The popular frequency domain solver MPB does not have any support for frequency dependent dielectrics.

Handling tabulated *ab initio* data for some these numerical tools will not be an easy task. One possible way of managing tabulated data is to load the data directly into a routine, whose task will be to generates model dielectric data for the standard routines of a given package. One will of course be left with the difficulty of interpolating values, which do not exist among the tabulated raw data. Another problem is the structure of some the standard numerics packages, which have grown over years or decades, and which have not always been documented very well during that time. This often makes the implementation of new features into an existing code a rather painful programming exercise.

12.6.1.2 TDDFT for Extended Systems

time–dependent density functional theory is without any doubt an excellent tool to predict the spectroscopic properties of isolated systems like molecules and small clusters. Here the linear response scheme (LRTDDFT) can be used to calculate the frequency–dependent spectrum. Alternatively, laser excitations can be simulated using time evolution schemes, which allow to capture non-linear behaviour as well.

Unfortunately for extended systems the situation is more complicated [27]. The linear response scheme suffers from two major problems. First it is not a self-consistent scheme. Moreover it relies on the band–structures calculated on the KS-DFT level, which are known to underestimate the band . This is a severe flaw, which cannot be corrected by the correlated density response alone (see Sec. 12.4). Second it is extremely difficult to find a good time–dependent density functional, even more difficult than for the Kohn–Sham case. In fact the most commonly used adiabatic LDA (ALDA) functional is not even frequency-dependent. No functional has been found up to now, which would reliably mimic the excitonic effects, and therefore the Bethe–Salpeter equation remains the only decent approach to study excitons using *ab initio* methods.

Besides linear response, the non-linear effects can be observed using laser excitation simulations. While this has been implemented for isolated systems in several program packages, it is still not available for extended systems. The difficulty stems from the periodic boundary conditions of the extended system [27]. Some fixes have been suggested, but their numerical implementations are

not stable enough to be implemented in any of the standard *ab initio* codes yet, in particular not without causing more damage than good.

12.6.1.3 Multi-Scale Tools

A straightforward multi-scale approach based on the numerical methods described in Sec. 12.1 would consist of tabulated dielectric data $\varepsilon(\omega)$ obtained with the help of *ab initio* methods described in Sec. 12.4, which is then either plugged into the analytical expressions of Ch. 11, Sec. 11.2.2. Or it could be plugged into a FD or FTDT solver (see Sec. 12.2 and 12.3) as dielectric data points on a grid. A typical example of such an approach would be our study of surface plasmon polaritons in graphene [42]. Methods of this kind would fall under the category of heterogeneous multi-scale methods, where one combines different numerical and analystical models [1]. For heterogeneous systems on the FDTD level it is sometimes necessary to work with finer meshes in certain regions (for a review see Ref. [43]). This type of multi-scale approach would fall under the category of multi-grid methods [1]. Unless we are able to solve the Schrödinger equation on the same type of spatio-temporal grid that we use to solve Maxwell's equations on a FDTD level, then the multi-grid approach will not be suitable for a multi-scale modeling of a plasmonic structure, which starts from the atomic structure of the basic materials.

Concerning the implementation of the more promising heterogeneous multi-scale methods in computational plasmonics, one would not really take advantage of their full potential by simply operating with tabulated *ab initio* data on a FD or FDTD level, or by plugging *ab initio* data into analytical models. Whenever we are interested in the coupling of optical phenomena between different mesoscopic systems as described in Ch. 11, Sec. 11.4, then it will be necessary to combine detailed atomistic simulations and coarse grained electromagnetic simulations much more directly.

For example, as long as we are in the usual linear-response regime to calculate the basic dielectric properties of a material using *ab initio* methods, the expressions for the determination of the dielectric function will always refer to a homogeneous external electric field, see Sec. 12.4. But these expressions are just a special case of a more general linear response formalism, which is nicely described in Ref. [44]. Note that a heterogeneous electric field like a sharp pulse, or the electric field in the vicinity of a plasmonic nanoparticle, could also modify the dielectric function on an atomic level, or they might even give rise to nonlinear effects. The resulting modified dielectric function will be fed back into the spatio-temporal grid used for the FDTD simulations, where the updated fields will back-react with the system on an atomic level again, etc.

Another example are interfaces or grain boundaries, where a simple mixing of dielectric functions will not always be sufficient. Therefore it might be necessary to fall back on atomistic models in order to understand the optical response around interfaces or surfaces. The optical properties of nanocrystals in particular are dominated by surface effects, and conventional methods are unlikely to describe the corresponding dielectric and optical properties, see Ch. 11, Sec. 11.4.

The best strategy to combine different numerical methods in a heterogeneous multi-scale approach is in general not known, because the choice and the combination of various numerical methods strongly depends on the nature of the problem that one wants to examine. This can be understood as follows [1]: Let us describe our system on a macro-level by a model $F(U, D) = 0$, where U is a macroscopic variable, and D the data needed to parameterize this model. On the micro-level we have a model $f(u, d) = 0$, where u is a microscopic variable, and d is the data needed to set up the microscopic model (e.g. constraints).

The biggest problem will not necessarily be the numerical solution of both models, where we in most cases one could easily find efficient numerical solvers. The more important problems will be the mappings $u \leftrightarrow U$, which require compression $u \leftarrow U$ or reconstruction $u \rightarrow U$ schemes over the configuration space. The second big problem are the mappings $d \leftrightarrow D$, which require constraints $d \leftarrow D$ and data estimation $d \rightarrow D$ schemes. Further complications arise, when one tries to impose some of these mappings over boundary conditions.

For a survey and nice examples see Ref. [1], where it becomes quite clear that a proper multi-scale modeling is still more of an artwork than a straightforward numerical procedure. Nevertheless we think that computational plasmonics would be a perfect playground to explore and further develop multi-scale modeling: The basic numerical methods are already well-established, and now it is time to put them all together.

12.7 Concluding Remarks

In this Chapter we had a look at some of the major computational methods used to model and analyse the various plasmonic phenomena. We showed how the basic dielectric properties of a given material may be calculated from first principles. We also presented ways to combine *ab initio* methods with a proper electrodynamical modelling of non-idealized plasmonic nanostructures and plasmonic nano-particles.

Combining the available methods complex systems can be evaluated, which is an extremely helpful addition to the more analytical tools and methods described in Chapter 11. The field of computational plasmonics has still many construction sides, as described in Section 12.6, which leaves room for many new and exciting methods and discoveries in the future.

Acknowledgements

The authors would like to thank the National Institute for Theoretical Physics (NITheP), the Mandelstam Institute for Theoretical Physics (MITP), the Materials Physics Research Institute (MPRI) and the DST-NRF Centre of Excellence in Strong Materials (CoE-SM) for support. We also acknowledge additional support through a bilateral project *Plasmonics for a better efficiency of solar cells* between South Africa and Italy (contributo del Ministero degli Affari Esteri e della Cooperazione Internazionale, Direzione Generale per la Promozione del Sistema Paese).

References

1. E. Weinan, *Principles of Multi-Scale Modeling* (Cambridge University Press, Cambridge, 2011)
2. A. Taflove, Wave Motion **10**, 547 (1988)
3. J. Hesthaven, T. Warburton, Journal of Computational Physics **181**(1), 186 (2002)
4. S.G. Johnson, J. Joannopoulos, Optical Express **8**(3), 173 (2001)
5. T.A. Driscoll, B. Fornberg, SIAM Sci. comput **21**(3), 1146 (1999)
6. P. Hohenberg, W. Kohn, Phys. Rev. **136**, B864 (1964)
7. W. Kohn, L.J. Sham, Phys. Rev. **140**(4A), A1133 (1965)
8. J.D. Joannopoulos, S.G. Johnson, J.N. Winn, R.D. Meade, *Photonic Crystals Molding the Flow of Light*, 2nd edn. (Princeton University Press, Princeton, 2008)
9. N. Ashcroft, N. Mermin, *Solid State Physics* (Saunders College, Philadelphia, 1976)
10. G.D. Smith, *Numerical Solution of Partial Differential Equations: Finite Difference Methods* (Oxford University Press, Oxford, 1985)
11. A.F. Oskooi, R. D., M. Ibanescu, P. Bermel, J.D. Joannopoulos, S.G. Johnson, Computer Physics Communications **181**, 687 (2010)
12. B.K. Juluri. Scattering / extinction / absorption cross-sections of silver nanowires (infinite cylinders) using meep. http://juluribk.com/2011/06/01/scattering-extinction-absorption-cross-sections-of-silver-nanowires-infinite-cylinders-using-meep/ (2011). 10-Dec-2015

13. K.S. Yee, IEEE Trans. Antennas Propagat. **14**(3), 302 (1966)
14. J.P. Berenger, Journal of computational physics **144**(2), 185 (1994)
15. E. Bécache, S. Fauqueux, P. Joly, Journal of Computational Physics **188**(2), 399 (2003)
16. R.G. Parr, W. Yang, *Density-Functional Theory of Atoms and Molecules*, *International Series of Monographs on Chemistry*, vol. 16 (Oxford University Press, Oxford, 1989)
17. F. Jensen, *Introduction to computational chemistry* (John Wiley & Sons, Chichester, England; Hoboken, NJ, 2007)
18. M. Born, R. Oppenheimer, Ann. Phys. **389**(20), 457 (1927)
19. J.P. Perdew, K. Schmidt, in *AIP Conference Proceedings*, vol. 577 (AIP Publishing, 2001), vol. 577, pp. 1–20
20. J.P. Perdew, A. Ruzsinszky, J. Tao, V.N. Staroverov, G.E. Scuseria, G.I. Csonka, The Journal of Chemical Physics **123**(6), 062201 (2005)
21. D.M. Ceperley, B.J. Alder, Phys. Rev. Lett. **45**(7), 566 (1980)
22. J.P. Perdew, K. Burke, M. Ernzerhof, Phys. Rev. Lett. **77**(18), 3865 (1996)
23. J.P. Perdew, K. Burke, M. Ernzerhof, Phys. Rev. Lett. **78**(7), 1396 (1997)
24. M. Kuisma, J. Ojanen, J. Enkovaara, T.T. Rantala, Phys. Rev. B **82**(11), 115106 (2010)
25. A.D. Becke, The Journal of Chemical Physics **98**(2), 1372 (1993)
26. L. Hedin, Phys. Rev. **139**(3A), A796 (1965)
27. G. Onida, L. Reining, A. Rubio, Rev. Mod. Phys. **74**(2), 601 (2002)
28. E. Runge, E.K.U. Gross, Phys. Rev. Lett. **52**(12), 997 (1984)
29. S.L. Adler, Phys. Rev. **126**(2), 413 (1962)
30. N. Wiser, Phys. Rev. **129**(1), 62 (1963)
31. R. Warmbier, A. Quandt, Computational Materials Science **114**, 18 (2016)
32. P. Giannozzi, S. Baroni, N. Bonini, M. Calandra, R. Car, C. Cavazzoni, D. Ceresoli, G.L. Chiarotti, M. Cococcioni, I. Dabo, A.D. Corso, S.d. Gironcoli, S. Fabris, G. Fratesi, R. Gebauer, U. Gerstmann, C. Gougoussis, A. Kokalj, M. Lazzeri, L. Martin-Samos, N. Marzari, F. Mauri, R. Mazzarello, S. Paolini, A. Pasquarello, L. Paulatto, C. Sbraccia, S. Scandolo, G. Sclauzero, A.P. Seitsonen, A. Smogunov, P. Umari, R.M. Wentzcovitch, J. Phys.: Condens. Matter **21**(39), 395502 (2009)
33. A. Marini, C. Hogan, M. Grüning, D. Varsano, Computer Physics Communications **180**(8), 1392 (2009)
34. P. Gori, M. Rakel, C. Cobet, W. Richter, N. Esser, A. Hoffmann, R. Del Sole, A. Cricenti, O. Pulci, Phys. Rev. B **81**(12), 125207 (2010)
35. P. Sheng, *Introduction to wave scattering, localization and mesoscopic phenomena* (Academic Press, San Diego, San Diego, 1995)
36. W.L. Barnes, A. Dereux, T.W. Ebbesen, Nature **424**, 824 (2003)
37. S.A. Maier, *Plasmonics: Fundamentals and applications* (Springer, New York, 2007)
38. L. Feng, M.H. Lu, V. Lomakin, Y. Fainman, Appl. Phys. Lett **93**(231105) (2008)
39. F. Mohammed, A. Quandt, Optical Materials pp. 107–109 (2015)
40. L. Feng, X.P. Liu, Y.F. Tang, Y.F. Chen, J. Zi, S.N. Zhu, Y.Y. Zhu, Phys. Rev. B **71**(195106) (2005)
41. I. El-Kady, M.M. Sigalas, R. Biswas, K.M. Ho, C.M. Soukoulis, Phys. Rev. B **62**(15299) (2000)
42. R. Warmbier, G.S. Manyali, A. Quandt, Phys. Rev. B **85**, 085442 (2012)

43. C. Christopoulos, {AEU} - International Journal of Electronics and Communications **57**(2), 100 (2003)
44. Y. Imry, *Introduction of mesoscopic physics* (Oxford University Press, Oxford, 2002)

Index

Acknowledgements

First and foremost I thank The Almighty ALLAH for His infinite blessings and mercy.

I am sincerely thankful to my supervisor, professor Alex Quandt for giving me the opportunity to be one of his students. His guidance and advice have substantially assisted me along the various stages. I have acquired elaborate knowledge during the period that I have worked under his supervision.

I would like to thank Dr. Robert Warmbier for the important role he played in this work. His endless support and expertise have paved the way and removed many obstacles. I would like to thank him for allowing me to share the office with him.

I am grateful to the members of our research group as well as MERG; especially Dr. Daniel Wamwangi, Tahir Aslan, Jason Myers, Khaled Baiuomy, Nhluvuko Mayimele, Nkosinathi Malaza, Patrick Mwonga and Timothy Mehay.

A Special thank you to the members of School of Physics, University of the Witwatersrand, especially professor Joao Rodrigues, and professor Daniel Joubert for their support.

I would like to thank all the friends and the colleagues who had directly or indirectly made a contribution to the work. I would like to express my gratitude to all of those who have always supported and encouraged the development of science in Africa in general, and AIMS in particular. Many thanks to professor Neil Toruk, AIMS founder, professor Fritz Hahne, the former director of AIMS, professor Barry Green, the current director, and the rest of AIMS community.

I would like to express my love and gratitude to my beloved wife for her infinite love, and words of encouragement throughout the difficult times. A special thank to my baby son Yazeed for filling our lives with joy, happiness and contentment.

To my parents, I am here because of you. Every success in my life is driven by you. Your guidance, your support, words of wisdom, encouragement and advice have lightened my way. I can not thank you enough for everything that you have done for me. Your love and support is beyond words. I am grateful that I am your son, and I would like to dedicate this thesis to you.

References

[1] E. Yablonovitch, T. J. Gmitter, R. D. Meade, A. M. Rappe, K. D. Brommer, , and J. D. Joannopoulos. Donor and acceptor modes in photonic band structure. *Physical Review Letters*, 67(24):3380, 1991. 1

[2] F. Mohammed and A. Quandt. About optical localization in photonic quasicrystals. *Optical and Quantum Electronics*, 48(8):380, 2016. 1, 38, 49, 55, 71

[3] F. Mohammed and A. Quandt. A simple perturbative tool to calculate plasmonic photonic bandstructures. *Optical Materials*, 56:107–109, 2016. 1, 33, 55, 59, 67

[4] F. Mohammed, R. Warmbier, and A. Quandt. Computational plasmonics: Theory and applications. Accepted as a book chapter, September 2016. 1, 3, 5, 6, 10, 56, 80

[5] F. Mohammed, R. Warmbier, and A. Quandt. Computational plasmonics: Numerical techniques. Accepted as a book chapter, September 2016. 1, 3, 6, 23, 56, 110

[6] H. J. W. Müller-Kirsten. *Electrodynamics: An Introduction Including Quantum Effects*. Wiley-VCH, Weinheim, Berlin, 2004. 3, 11

[7] C. Cohen-Tannoudji, B. Diu, and F. Laloe. *Quantum Mechanics*. John Wiley and Sons, Hoboken, 1977. 3

[8] M. Fox. *Optical Properties of Solids*. Oxford University Press, Oxford, 2010. 5, 6, 7, 9

[9] R. Warmbier and A. Quandt. Plasmonic and dielectric properties of ideal graphene. *Computational Materials Science*, 114:18–22, March 2016. 5

[10] S. L. Adler. Quantum Theory of the Dielectric Constant in Real Solids. *Phys. Rev.*, 126(2):413–420, April 1962. 5, 7

[11] E. Ozbay. Plasmonics: Merging photonics and electronics at nanoscale dimensions. *Science*, 311(5758):189–193, 2006. 6, 19

[12] S. A. Maier. *Plasmonics: Fundamentals and applications*. Springer, New York, 2007. 6, 19

[13] C. Kittel. *Quantum Theory of Solids*. John Wiley and Sons, New York, 2 edition, 1987. kittel reference. 8

[14] J. Bellessa, C. Bonnand, J. C. Plenet, and J. Mugnier. Strong coupling between surface plasmons and excitons in an organic semiconductor. *Phys. Rev. Lett.*, 93:036404, Jul 2004. 8

[15] J. D. Jackson. *Classical electrodynamics*. Wiley, 1999. 9

[16] L. Novotny and B. Hecht. *Principles of nano-optics*. Cambridge University Press, Cambridge, 2012. 10, 11

[17] S. A. Maier and H. A. Atwater. Plasmonics: Localization and guiding of electromagnetic energy in metal/dielectric structures. *Journal of Applied Physics*, 98(1):011101, 2005. 10

[18] S. A. Maier, M. L. Brongersma, P. G. Kik, S. Meltzer, A. A. G. Requicha, and H. A. Atwater. Plasmonics: A route to nanoscale optical devices. *Advanced Materials*, 13(19):1501–1505, 2001. 10

[19] C. F. Bohren, D. R. Huffman, and E. E. Clothiaux. *Absorption and Scattering of Light by Small Particles*. Wiley-VCH, Weinheim, Berlin, 2016. 10, 11, 12

[20] A. F. Oskooi, D. Roundy, M. Ibanescu, P. Bermel, J. D. Joannopoulos, and S. G. Johnson. Meep: A flexible free-software package for electromagnetic simulations by the fdtd method. *Computer Physics Communications*, 181:687–702, 2010. 13, 40

[21] Peter Y. Y. and M. Cardona. *Fundamentals of Semiconductors: Physics and Materials Properties*. Springer Berlin, 3rd edition, 2005. 14

[22] E. Yablonovitch. Inhibited spontaneous emission in solid-state physics and electronics. *Phys. Rev. Lett.*, 58:2059–2062, May 1987. 14

[23] S. John. Strong localization of photons in certain disordered dielectric superlattices. *Phys. Rev. Lett.*, 58:2486–2489, Jun 1987. 14

[24] I. El-Kady, M. M. Sigalas, R. Biswas, K. M. Ho, and C. M. Soukoulis. Metallic photonic crystals at optical wavelengths. *Phys. Rev. B*, 62(23):15229–15302, 2000. 14, 35

[25] O. Painter, R. K. Lee, A. Scherer, A. Yariv, J. D. O'brien, P. D. Dapkus, and I. Kim. Two-dimensional photonic band-gap defect mode laser. *Science*, 284(5421):1819–1821, 1999. 14

[26] J. Broeng, D. Mogilevstev, S. E. Barkou, and A. Bjarklev. Photonic crystal fibers: A new class of optical waveguides. *Optical fiber technology*, 5(3):305–330, 1999. 14

[27] D. R. Smith, J. B. Pendry, and M. C. K. Wiltshire. Metamaterials and negative refractive index. *Science*, 305(5685):788–792, 2004. 14

[28] T. Baba. Slow light in photonic crystals. *Nature photonics*, 2(8):465–473, 2008. 14

[29] N.W. Ashcroft and N.D. Mermin. *Solid State Physics*. Saunders College, Philadelphia, 1976. 15, 25, 28

[30] J. D. Joannopoulos, S. G. Johnson, J. N. Winn, and R. D. Meade. *Photonic Crystals Molding the Flow of Light*. Princeton University Press, 2nd edition edition, 2008. 15, 16, 24, 25, 26, 28, 33, 46

[31] V. Berger. Nonlinear photonic crystals. *Phys. Rev. Lett.*, 81:4136–4139, Nov 1998. 15

[32] S. G. Johnson and J. D. Joannopoulos. Block-iterative frequency-domain methods for maxwell's equations in a planewave basis. *Optical Express*, 8(3):173–190, 2001. 16, 23, 24, 26, 28, 33, 34

[33] J. Teyssier, S. V. Saenko, D. van der Marel, and M. C. Milinkovitch. Photonic crystals cause active colour change in chameleons. *Nature Communications*, 6(6368), 2014. 17, 18

[34] T Smith and J Guild. The c.i.e. colorimetric standards and their use. *Transactions of the Optical Society*, 33(3):73, 1931. 19

[35] H. Raether. *Surface Plasmons on Smooth and Rough Surfaces and on Gratings*. Springer, Berlin, 1988. 19

[36] William L. Barnes, Alain Dereux, and Thomas W. Ebbesen. Review article surface plasmon subwavelength optics. *Nature*, 424:824–830, 2003. 19

[37] L. Feng, M.-H. Lu, V. Lomakin, and Y. Fainman. Plasmonic photonic crystal with a complete band gap for surface plasmon polariton waves. *Applied Physics Letters*, 93(23):231105, 2008. 19, 34

[38] S. Guddala, S. A. Kamanoor, A. Chiappini, M. Ferrari, and N. R. Desai. Experimental investigation of photonic band gap influence on enhancement of raman-scattering in metal-dielectric colloidal crystals. *Journal of Applied Physics*, 112(084303):1–7, 2012. 19

[39] N. N. Lal, B. F. Soares, J. K. Sinha, F. Huang, S. Mahajan, P. N. Bartlett, N. C. Greenham, and J. J. Baumberg. Enhancing solar cells with localized plasmons in nanovoids. *Optics Express*, 19(12):11256–11263, 2011. 19

[40] S. I. Bozhevolnyi, J. E. Erland, K. Leosson, P. M. W. Skovgaard, and J. M. Hvam. Waveguiding in surface plasmon polariton band gap structures. *Phys. Rev. Lett.*, 86(14):3008–3011, 2001. 19

[41] C. Marquart, S. I. Bozhevolnyi, and K. Leosson. Near-field imaging of surface plasmon-polariton guiding in band gap structures at telecom wavelengths. *Optics Express*, 13(9):3303–3309, 2005. 19

[42] M. U. Gonzlez, J.-C. Weeber, A.-L. Baudrion, A. Dereux, A. L. Stepanov, J. R. Krenn, E. Devaux, and T. W. Ebbesen. Design, near-field characterization, and modeling of 45 surface-plasmon bragg mirrors. *Phys. Rev. B*, 73(15):155416–155429, 2006. 19

[43] J.-C. Weeber, A. Bouhelier, G. Colas des Francs, L. Markey, and A. Dereux. Submicrometer in-plane integrated surface plasmon cavities. *Nano Letters*, 7(5):13521359, 2007. 19

[44] Z. Yu, G. Veronis, Z. Wang, and S. Fan. One-way electromagnetic waveguide formed at the interface between a plasmonic metal under a static magnetic field and a photonic crystal. *Phys. Rev. Lett.*, 100(02):023902–023906, 2008. 19

[45] W. P. Anderson. Absence of diffusion in certain random lattices. *Physical review*, 109(5):1492, 1958. 20

[46] P. Sheng. *Introduction to wave scattering, localization, and mesoscopic phenomena*. Springer, Berlin, 2nd edition, 2006. 20, 21, 34, 39, 41, 43, 45, 46, 54

[47] E. Abrahams, P. W. Anderson, D. C. Licciardello, and T. V. Ramakrishnan. Scaling theory of localization: Absence of quantum diffusion in two dimensions. *Physical Review Letters*, 42(10):673, 1979. 21

[48] E. Weinan. *Principles of Multi-Scale Modeling*. Cambridge University Press, Cambridge, 2011. 23, 29, 32

[49] A. Taflove. Review of the formulation and applications of the finite-differences time-doamin method for numerical modelind of electromagnetic wave interactions with arbitrary structures. *Wave Motion*, 10:547–582, 1988. 23, 29, 32

[50] J. Hesthaven and T. Warburton. Nodal high-order methods on unstructured grids: I. time-domain solution of maxwell's equations. *Journal of Computational Physics*, 181(1):186 – 221, 2002. 23

[51] T. A. Driscoll and B. Fornberg. Lock pseudospectral methods for maxwells equations: Ii. twodimensional, discontinuouscoefficient case. *SIAM Sci. comput*, 21(3):1146 – 1167, 1999. 23

[52] P. Hohenberg and W. Kohn. Inhomogeneous electron gas. *Phys. Rev.*, 136:B864–B871, Nov 1964. 24

[53] W. Kohn and L. J. Sham. Self-Consistent Equations Including Exchange and Correlation Effects. *Phys. Rev.*, 140(4A):A1133–A1138, November 1965. 24

[54] P. Concus, G. H. Golub, and G. Meurant. Block preconditioning for the conjugate gradient method. *SIAM Journal on Scientific and Statistical Computing*, 6(1):220–252, 1985. 27

[55] M. C. Payne, M. P. Teter, D. C. Allan, T. A. Arias, and J. D. Joannopoulos. Iterative minimization techniques for ab initio total-energy calculations: molecular dynamics and conjugate gradients. *Rev. Mod. Phys.*, 64:1045–1097, Oct 1992. 27

[56] G. A. Niklasson, C. G. Granqvist, and O. Hunderi. Effective medium models for the optical properties of inhomogeneous materials. *Applied Optics*, 20(1):26–30, 1981. 28

[57] G. D. Smith. *Numerical Solution of Partial Differential Equations: Finite Difference Methods*. Oxford University Press, 1985. 29

[58] K. S. Yee. Numerical solution of initial boundary value problems involving maxwell's equationsin isotropic media. *IEEE Trans. Antennas Propagat.*, 14(3):302–307, 1966. 29

[59] J. P. Berenger. A perfectly matched layer for the absorption of electromagnetic waves. *Journal of computational physics*, 144(2):185–200, 1994. 32

[60] E. Bécache, S. Fauqueux, and P. Joly. Stability of perfectly matched layers, group velocities and anisotropic waves. *Journal of Computational Physics*, 188(2):399–433, 2003. 32

[61] L. Feng, X. P. Liu, Y. F. Tang, Y. F. Chen, J. Zi, S. N. Zhu, and Y. Y. Zhu. Tunable negative refraction in a two-dimensional active magneto-optical photonic crystal. *Phys. Rev. B*, 71(19):195106–195112, 2005. 34

[62] *Ab initio simulations of optical materials*, Transparent Optical Networks (ICTON), 2014 16th International Conference on. IEEE, July 2014. 37, 56

[63] C. Janot. *Quasicrystals*. Clarendon Press, Oxford, 2nd edition, 1994. 38, 39, 49

[64] SI Ben-Abraham and A. Quandt. Hybrid quasiperiodic-periodic structures constructed by projection in two stages. *Acta Crystallographica Section A: Foundations of Crystallography*, 63(2):177–185, 2007. 38, 39, 41, 50

[65] M. E. Zoorob, M. D. B. Charleton, G. J. Parker, J. J. Baumberg, and M. C. Netti. Complete photonic band gap in 12-fold symmetric quasicrystals. *Nature*, 404:740743, 2000. 38, 49

[66] X. Zhang, Z. Q. Zhang, and C. T. Chan. Absolute photonic band gap in 12-fold symmetric photonic crystals. *Phys. Rev. B*, 63:081105, 2001. 38, 49

[67] A. Della Villa, S. Enoch, G. Tayeb, F. Capolino, V. Pierro, and V. Aldi. Localized modes in photonic quasicrystals with penrose-type lattice. *Opt Express*, 14(21):10021, 2006. 38

[68] M. Baake, D. Joseph, and M. Schlottmann. The root lattice d_4 and planar quasilattices with octagonal and dodecagonal symmetry. *International Journal of Modern Physics B*, 05:1924, 1991. 41

[69] J. H. Conway and N. J. A. Sloane. *Sphere packings, lattices and groups*. Springer, New York, 3rd edition, 1999. 41

[70] K. Edagawa. Photonic crystals, amorphous materials, and quasicrystals. *Sci. Technol. Adv. Mater*, 15:034805, 2014. 41, 49

[71] D. N. Christodoulides and R. I. Joseph. Discrete self-focusing in nonlinear arrays of coupled waveguides. *Optics letters*, 13(9):794–796, 1988. 46

[72] T. Schwartz, G. Bartal, S. Fishman, and M. Segev. Localization of light in disordered lattices. *Optics and Photonics News*, 18(12):35–35, 2007. 46

[73] Y. Lahini, A. Avidan, F. Pozzi, M. Sorel, R. Morandotti, D. N. Christodoulides, and Y. Silberberg. Anderson localization and nonlinearity in one-dimensional disordered photonic lattices. *Physical Review Letters*, 100(1):013906, 2008. 46

[74] M. Segev, Y. Silberberg, and D. N. Christodoulides. Anderson localization of light. *Nature Photonics*, 7(3):197–204, 2013. 46

[75] F. Wegner. Inverse participation ratio in $2 + \varepsilon$ dimensions. *Z. Physik B*, 36:209–214, 1980. 46

[76] Z. V. Vardeny, A. Nahata, and A. Agrawal. Optics of photonics quasicrystals. *Nature Photonics*, 7:177–187, 2013. 49

[77] W. JIN, J. JU, H. L. HO, Y. L. HOO, and A. ZHANG. Photonic crystal fibers devices and applications. *Front Optoelectron*, 6:3–24, 2013. 49

[78] D. Shechtman, J. Blech, D. Gratias, and J. W. Cahn. Metallic phase with long range orientational order and no translational symmetry. *Phys. Rev. Lett*, 53:1951–1953, 1984. 49

[79] W. Gellermann, M. Kohmoto, B. Sutherland, and P. C. Taylor. Localization of light waves in fibonacci dielectric multilayers. *Phys. Rev. Lett.*, 72:633, 1994. 49

[80] T. Hattori, N. Tsurumachi, S. Kawato, and H. Nakatsuka. Photonic dispersion relation in a one-dimensional quasicrystal. *Phys. Rev. B*, 50:R4220, 1994. 49

[81] L. Dal Negro, C. J. Oton, Z. Gaburro, L. Pavesi, P. Johnson, A. Lagendijk, R. Righini, M. Colocci, and D. S. Wiersma. Light transport through the band-edge states of fibonacci quasicrystals. *Phys. Rev. Lett.*, 90:055501, 2003. 49

[82] Y. Neve-Oz, T. Pollok, S. Burger, M. Golosovsky, and D. Davidov. Resonant transmission of electromagnetic waves through two-dimensional photonic quasicrystals. *Journal of Applied Physics*, 107:063105, 2010. 49

[83] M. Kohmoto, B. Sutherland, and K. Iguchi. Localization in optics: Quasiperiodic media. *Phys. Rev. Lett.*, 58:23, 1987. 49

[84] L Maigyte and K Staliunas. Spatial filtering with photonic crystals. *Applied Physics Reviews*, 2(1):011102, 2015. 55

[85] G Gomard, R Peretti, E Drouard, X Meng, and C Seassal. Photonic crystals and optical mode engineering for thin film photovoltaics. *Optics express*, 21(103):A515–A527, 2013. 55

[86] JC Knight, TA Birks, P St J Russell, and DM Atkin. All-silica single-mode optical fiber with photonic crystal cladding. *Optics letters*, 21(19):1547–1549, 1996. 55